SEDIMENTOLOGY the journal of the International Association of Sedimentologists

Sedimentology (2016) doi: 10.1111/sed.12318

Encounters with an unearthly mudstone: Understanding the first mudstone found on Mars

JUERGEN SCHIEBER*, DAVID BISH*, MAX COLEMAN†, MARK REED‡, ELISABETH M. HAUSRATH§, JOHN COSGROVE¶, SANJEEV GUPTA¶, MICHELLE E. MINITTI**, KENNETH S. EDGETT†† and MIKE MALIN††

**Department of Geological Sciences, Indiana University, 1001 East 10th Street, Bloomington, IN 47405-1405, USA (E-mail: jschiebe@indiana.edu)*

†Jet Propulsion Laboratory, California Institute of Technology and NASA Astrobiology Institute, 4800 Oak Grove Drive, Pasadena, CA 91109, USA

‡Department of Geological Sciences, University of Oregon, 1585 East 13th Avenue, Eugene, OR 97403, USA

§Department of Geoscience, University of Nevada Las Vegas, 4505 South Maryland Parkway, Las Vegas, NV 89154, USA

¶Department of Earth Science and Engineering, Imperial College, London, SW7 2AZ, UK

***Planetary Science Institute, 1700 East Fort Lowell Road #106, Tucson, AZ 85719, USA*

††Malin Space Science Systems, 5880 Pacific Center Boulevard, San Diego, CA 92121, USA

Associate Editor – Nathan Sheldon

ABSTRACT

The Sheepbed mudstone forms the base of the strata examined by the Curiosity rover in Gale Crater on Mars, and is the first *bona fide* mudstone known on another planet. From images and associated data, this contribution proposes a holistic interpretation of depositional regime, diagenesis and burial history. A lake basin probably received sediment pulses from alluvial fans. Bed cross-sections show millimetre to centimetre-scale layering due to distal pulses of fluvial sediment injections (fine-grained hyperpycnites), fall-out from river plumes, and some aeolian supply. Diagenetic features include mineralized synaeresis cracks and millimetre-scale nodules, as well as stratiform cementation. Clay minerals were initially considered due to *in situ* alteration, but bulk rock chemistry and mineralogy suggests that sediments were derived from variably weathered source rocks that probably contained pre-existing clay minerals. X-ray diffraction analyses show contrasting clay mineralogy in closely spaced samples, consistent with at least partial detrital supply of clay minerals. A significant (*ca* 30 wt%) amorphous component is consistent with little post-depositional alteration. Theoretical modelling of diagenetic reactions, as well as kinetic considerations, suggest that the bulk of diagenetic clay mineral formation occurred comparatively late in diagenesis. Diagenetic features (synaeresis cracks and nodules) were previously thought to reflect early diagenetic gas formation, but an alternative scenario of synaeresis crack formation via fabric collapse of flocculated clays appears more likely. The observed diagenetic features, such as solid nodules, hollow nodules, matrix cement and 'raised ridges' (synaeresis cracks) can be explained with progressive alteration of olivine/glass in conjunction with centrifugal and counter diffusion of reactive species. Anhydrite-filled fractures in the Sheepbed mudstone occurred late in diagenesis when fluid pressures built up to exceed lithostatic pressure. Generating fluid overpressure by burial to facilitate hydraulic fracturing suggests a burial depth of at least 1000 m for the underlying strata that supplied these fluids.

Keywords Burial history, deposition, diagenesis, Mars, mudstone.

INTRODUCTION

Because the Mars Science Laboratory (MSL) mission objective is the search for habitable environments, mudstones are a high priority rock type due to their known capacity for preserving organic remains. Since landing on Mars on 6 August 2012, the Curiosity rover (also known as the MSL), has explored outcrops in Gale crater, and careful mapping of the crater floor by team members (Grotzinger *et al.*, 2014) led to identification of a potential target 450 m east of the landing site (Fig. 1A), the so-called Sheepbed mudstone (Grotzinger *et al.*, 2014). The full rover payload and its contact-science instruments (Fig. 1C, D and E), consisting of assorted geochemical analytical capabilities (Alpha Particle X-Ray Spectrometer – APXS; Chemistry & Camera – ChemCam; Chemistry & Mineralogy X-Ray Diffraction – CheMin; Sample Analysis at Mars Instrument Suite – SAM) and a range of cameras for navigation (Navigation Cameras – Navcam; Hazard Avoidance Cameras – Hazcam) and science observations (Mast Cameras – Mastcam; Mars Descent Imager – MARDI; Mars Hand Lens Imager – MAHLI), were engaged in its investigation (Fig. 1B). A large number of papers has already been published on the results of these investigations (e.g. Grotzinger *et al.*, 2014; McLennan *et al.*, 2014; Nachon *et al.*, 2014; Siebach *et al.*, 2014; Stack *et al.*, 2014; Vaniman *et al.*, 2014; Bristow *et al.*, 2015; Mangold *et al.*, 2015) with particular focus on sedimentary rocks, the role of water during their deposition and potential habitability (Grotzinger *et al.*, 2014).

Drawing on multiple data sets, the Sheepbed mudstone was interpreted as a lacustrine deposit that accumulated in a crater lake as alluvial fans supplied water and sediment from the crater rim (Grotzinger *et al.*, 2014). At present, however, much of what has been published on the origin of this mudstone unit is weighted towards consideration of diagenetic features and geochemical analyses (McLennan *et al.*, 2014; Siebach *et al.*, 2014; Stack *et al.*, 2014; Vaniman *et al.*, 2014).

Upon careful consideration of the available data, several of the authors thought that alternative or improved interpretations were possible with regard to the nature of the original sediment, the sedimentary features in the Sheepbed mudstone, diagenetic features and diagenetic chemistry, as well as burial history. The authors also think that it would be helpful to the geological community if a holistic reappraisal of the geology and origin of this mudstone were to be made available. A major aspect of this re-examination consisted of careful examination of the broader stratigraphic relationships (Mastcam), sedimentary features at the outcrop scale (Mastcam), and detailed textural relationships at the centimetre to millimetre-scale (MAHLI), because image data constitute the largest body of observations available. A second perspective consisted of a re-examination of the mineralogical (XRD, CheMin) data and whole-rock analyses (APXS) with a view towards understanding the degree of weathering of the source rocks and the likelihood of detrital clays, and combining these data with geochemical modelling of plausible diagenetic alteration pathways and consideration of reaction kinetics. Following from these efforts, a diagenetic reaction scheme was developed that explains the observed diagenetic features in the context of depositional processes, as well as plausible chemical reactions in the pore waters of the accumulating muds. Finally, the late diagenetic fluid flow events that impacted these rocks and caused hydraulic fractures filled with anhydrite were considered in the context of comparable phenomena on Earth, suggesting the presence of a considerable thickness of crater fill strata buried beneath the Yellowknife Bay succession. An additional objective of this paper is to convey how the constraints of rover-conducted geology necessitate careful interdisciplinary examination and analysis of the limited data in order to arrive at well-founded interpretations.

LIMITATIONS OF THE ROVER GEOLOGIST PROXY

The manner in which an actual geologist performs field work is vastly different from the procedures that have to be used when working with a rover proxy. One of the main barriers is the fact that radio signals from Earth, depending on their relative positions, can take anywhere between four and a half and 21 minutes to get to Mars, and therefore real time rover operation is not possible. Any action the rover undertakes needs to be carefully planned and choreographed. A risky activity by the rover that is not recognized during planning could damage or incapacitate the rover and cause an end to the mission. Basic tasks that terrestrial field geologists take for granted become highly involved procedures that entail planning and vetting by a large team of scientists and engineers. Think of

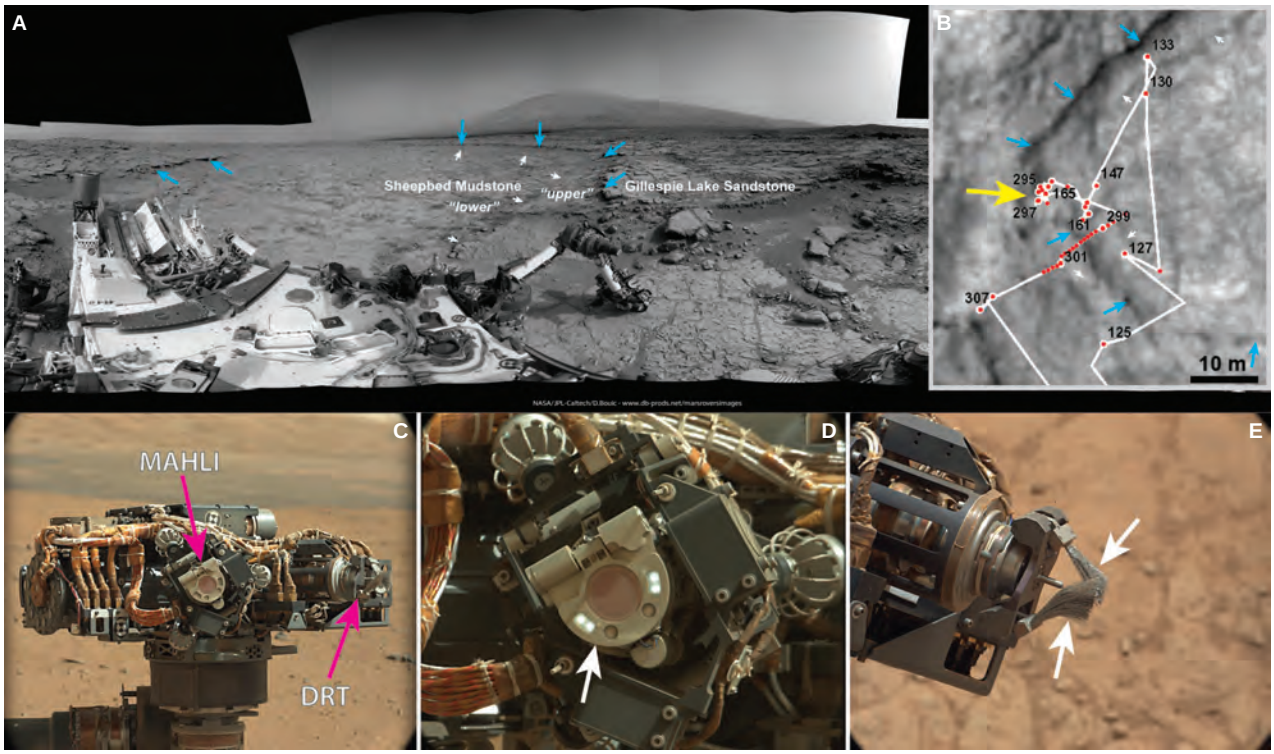

Fig. 1. (A) Black and white Navcam panorama (Sol 168, sequences ncam05794, ncam07754 and ncam12754; Sol 169 sequence ncam05794) that shows Mt. Sharp in the distance. Yellowknife Bay with the Sheepbed mudstone is left of centre, the Gillespie Lake sandstone in the centre and to the right, and the instrument turret of the rover arm is set down at the John Klein drill site. Small white arrows point to a stratigraphic boundary within the Sheepbed member that is also visible from orbit. This boundary marks in the context of this paper the contact between unit 1 and unit 2 of the Sheepbed mudstone. Blue arrows mark the erosion-resistant escarpment formed by the Gillespie Lake sandstone. (B) The path of the rover in Yellowknife Bay. Red dots and black numbers mark Sol locations. It is apparent that most time was spent in the westernmost portion (yellow arrow) on investigations of Sheepbed unit 2. Blue and white arrows mark same features as shown in (A). (C) View of instrument turret at end of rover arm (Mastcam Left image 0032ML0000760000100861E01). Pointed out with arrows are the rover's 'hand lens', the MAHLI camera, and the dust removal tool (DRT). (D) The front end of the MAHLI camera with dust cover (arrow) closed (Mastcam Right image 0032MR0000690020100777E01). The bright spots in the rim of the dust cover are LEDs for night time imaging. (E) Closer look at the DRT (Mastcam Right image 0150MR0007550000201222E01). Two sets of stainless steel bristles (arrows) rotate and sweep away surface dust. MAHLI, Mars Hand Lens Imager.

a fundamental field task like breaking off a piece of rock and looking at it with a hand lens. Curiosity is not equipped with a rock hammer, but rather relies on the DRT (Dust Removal Tool) to clear dusty rock surfaces (Fig. 1E). On occasion, however, the rover wheels break rocks that they drive over, producing fresh surfaces for interrogation. However, the path from creating such a fresh surface to investigating it is a multi–sol endeavour, from identifying the fresh surface to assessing its reachability with the rover arm and turret instruments to acquiring close-up images to returning the data. Thus, a task that on Earth would take a field geologist five minutes could consume an entire week of rover operations. The rover has multiple science instruments that can be utilized within one command cycle, but limits on the complexity of a given plan and power use restrict how much can be carried out on a given sol (sol is the term used by Mars researchers to denote the duration of a day on Mars).

The Yellowknife Bay campaign was conducted from 19 December 2012 (Sol 125) to 10 June 2013 (Sol 301), a total of 174 Earth days, and the bulk of the detailed science activities took place in a 5 by 15 m area in the westernmost corner of Yellowknife Bay (Fig. 1B). For a geologist on Earth, to scrutinize an area of that size, take pictures and collect some samples for

later analysis could easily be accomplished in a single day; and there is always the option to come back for another look if necessary. On Mars, the rover rarely backtracks to previously visited stops; the science team makes the best of the images and data collected, and gets accustomed to uncertainty and doubt. This may sound discouraging, but Curiosity is the most powerful rover that ever landed on Mars, which is as good as it gets for studying Martian geology. Although a series of initial results were published within six to 12 months following the Yellowknife Bay campaign (see *Introduction*), this contribution is an effort to re-assess the sedimentary geology of the first mudstone encountered on Mars, benefitting from more time for careful re-examination of data and images, further discussions with colleagues, and experimental work to better understand the implications of observed aeolian abrasion features.

When it comes to the study of coarser sediments, such as sandstones and conglomerates, the Mastcam science cameras on the rover (Malin *et al.*, 2010b) have provided an abundance of observational data. These have been very helpful for interpreting the outcrops and putting them in context, and they were of a scale and quality to allow quick publication of results. Yet although Mastcam images have been very beneficial for interpreting sandstones and conglomerates (e.g. Williams *et al.*, 2013; Anderson *et al.*, 2015), the small grain size of mudstones presents considerable challenges.

Earth-based studies of mudstones rely heavily on thin-section petrography with petrographic microscope and scanning electron microscopy (SEM) (Lazar *et al.*, 2015), options that are not available on current Mars rovers. The best instrument for visual inspection is the MAHLI camera (the 'handlens'; Edgett *et al.*, 2012) that is attached to the robotic arm (Fig. 1D); MAHLI can achieve a pixel scale of about 14 μm at closest approach (2·1 cm working distance). In order to differentiate an object it has to be bordered by pixels of differing brightness/colour, and thus any object smaller than 42 μm is technically not resolvable. Because mudstones are defined as 'no coarser' than 62·5 μm (Lazar *et al.*, 2015), MAHLI can be used to differentiate mudstones from coarser lithologies. MAHLI imaging, however, requires the use of the robotic arm of the rover, and its use requires substantially more planning and time than imaging via Mastcam. MAHLI is therefore most efficiently used when the rover is at a location where other contact-science instruments at the end of the robotic arm are utilized as well (Fig. 1C).

GEOLOGICAL AND STRATIGRAPHIC SETTING

The present study area is in Gale crater, a 154 km diameter impact crater that is located near the Martian dichotomy boundary (Latitude 5°S, Longitude 138°E) and probably formed in the Early Hesperian or during the Noachian–Hesperian transition (Grant *et al.*, 2014). In its interior, it contains a 5 km tall mound of sedimentary rocks (Malin & Edgett, 2001) that

Fig. 2. Overview of Yellowknife Bay. (A) Composite of two HiRISE orbital images (25 cm/pixel). Images ESP_028335_1755 and ESP_032436_1755 were combined because each image is only partially optimal due to shadowing at the time of image acquisition. Yellowknife Bay is a depression that consists of the aeolian eroded Sheepbed mudstone (polygonal crack network) that is bordered by an erosion-resistant escarpment, the Gillespie sandstone. (A') Annotated image. The yellow dashed line marks the contact/escarpment between the Sheepbed mudstone and the Gillespie sandstone. The red dashed lines mark layers and sets of layers that are also visible in Mastcam images (Fig. 3). Arrows and white lettering mark locations along the escarpment that are also shown in (C), (D) and Fig. 3. The red and blue circles mark the Cumberland and John Klein drill sites, respectively. Stepped white dashed line marks border between the two HiRISE images. (B) Close-up of the stratigraphic interval discussed (Mastcam Left mosaic from Sol 298; images 0298ML0012440000106393E03, 0298ML0012440010106394E02, 0298ML0012440020106395E01, 0298ML0012440030106396E01). The Gillespie sandstone is a resistant cap above the softer Sheepbed mudstone. The black shadows at the contact are due to erosional undercutting of the Gillespie sandstone. Because the image is of a gently sloping surface, the scale changes from foreground to background. Two better cemented horizons that weather as resistant ledges are marked with yellow arrows. (C) 360 degree panorama acquired with Mastcam Left on Sol 137 location (mcam00818), marked with white circle in (A'), red and blue circles mark the John Klein and Cumberland drill sites, respectively. White lettering and arrows point to same locations as in (A'). The yellow letter 'F' is a reference point for images (C) and (D). (D) A higher resolution panorama (Mastcam Right, Sol 147, mcam00834) that includes locations along the southern edge of Yellowknife Bay (shown in more detail in Fig. 3).

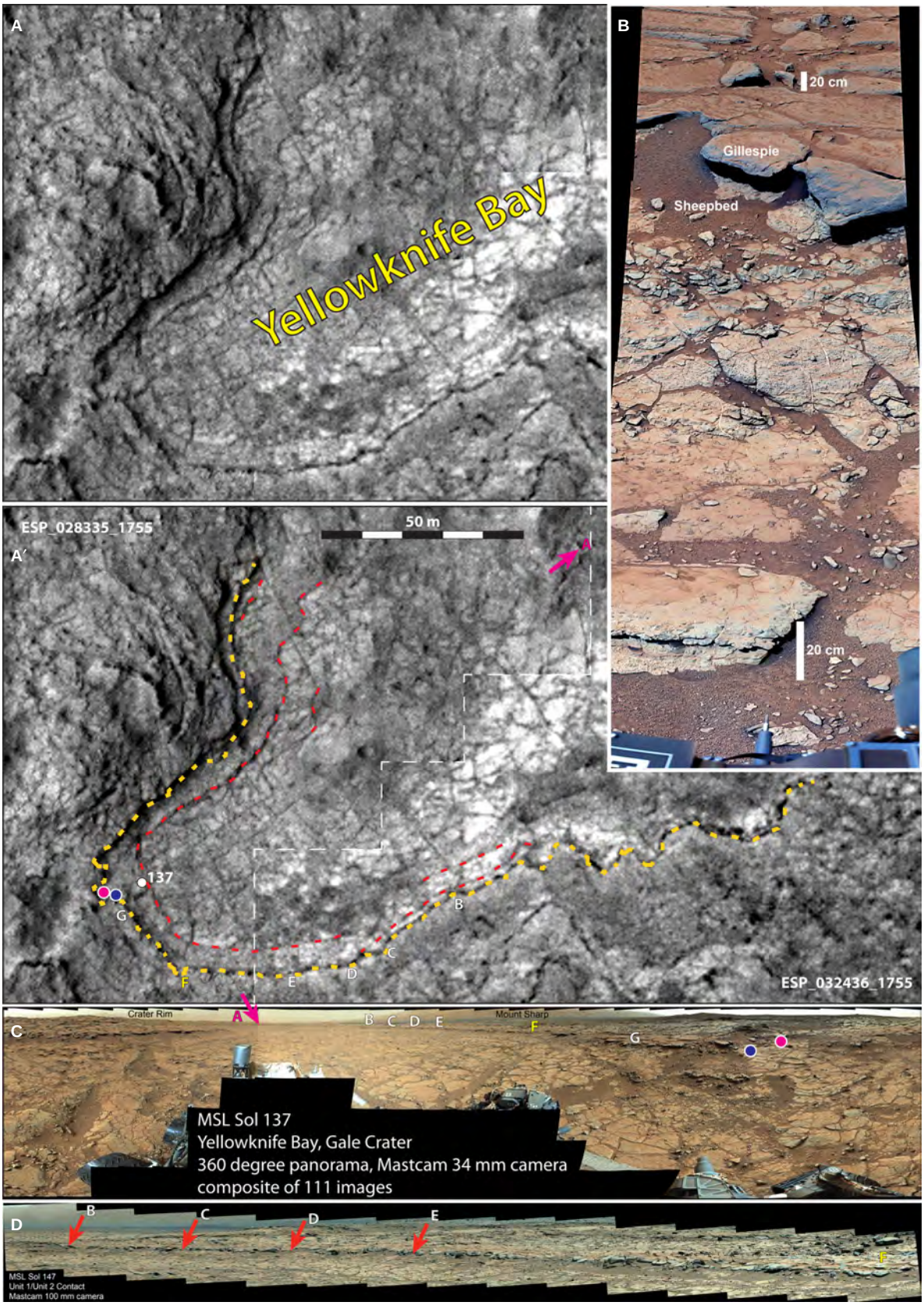

represents an extended record of Martian history in the Hesperian (*ca* 3·7 to 3·0 Gya; Tanaka, 1986) and appears to capture the transition from a wet to a dry Mars (Grotzinger *et al.*, 2015). The mound is informally referred to as Mt. Sharp, although its official name is Aeolis Mons. The mudstone that is the focus of this investigation, the Sheepbed member of the Yellowknife Bay formation (Grotzinger *et al.*, 2014), crops out in a depression (Yellowknife Bay, Fig. 2) that is located approximately 450 m east of the landing site (in this paper it is also referred to as the Sheepbed mudstone).

The Sheepbed member is the stratigraphically lowest unit of the Yellowknife Bay formation (Grotzinger *et al.*, 2014), and although its thickness is unknown, at least 2 m are exposed below the contact with the overlying Gillespie Lake member, a well-cemented sandstone (Fig. 2B). The contact between the two units is sharp because of strong lithological contrast and further enhanced by differential erosion (Fig. 2B). The Sheepbed/Gillespie contact forms a prominent escarpment that is visible from orbit in HiRISE (High Resolution Imaging Science Experiment) imagery (Fig. 2A) at a pixel resolution of 25 cm. In addition, bedding within the Sheepbed member that is prominent in outcrop (Fig. 3) is also discernable in orbital images (Fig. 2A').

Although the Sheepbed member was only examined closely in the vicinity of locality G (Fig. 2C), two high-resolution image mosaics (Fig. 2C and D) that were acquired with the right eye of Mastcam (focal length = 100 mm) were also scrutinized. The overall impression from Yellowknife Bay Mastcam images is that rocks that are conspicuous in outcrop due to differential erosion are most likely well-cemented sandstones, such as exemplified by the Gillespie Lake member. Thus, the authors consider the weathering resistant concave feature in the most distal image of the Sheepbed member (Fig. 3A) to be a sandstone that fills a scour or channel into underlying mudstone. Similarly, the resistant beds at location B (Fig. 3B) are therefore considered of cemented sandstone composition at their base. Between locations B and E (Fig. 3), a prominent couplet can be followed over a distance of approximately 45 m, and this interval may be equivalent to a bundle of resistant layers observed at locality G (Fig. 6). These beds appear more weathering resistant at the base and softer towards the top. This property may be due to an upward increase of clay content and softness, and is thus suggestive of grading.

METHODS

Images: MastCam consists of two colour cameras. The left camera (M-34) has 34 mm focal length, an image scale of 0·22 mrad/pixel, and a 18·4° × 15° field of view, and acquires 1600 × 1200 pixel images. The right camera is identical, except for the focal length (100 mm). Image scale is 0·074 mrad/pixel, and field of view is 6·3° × 5·1° (Malin *et al.*, 2010b; Bell *et al.*, 2012). The Mars Hand Lens Imager (MAHLI), attached to the instrument turret at the end of the rover's robotic arm (Fig. 1), is a 2 megapixel colour close-up camera that can focus from 2·1 cm to infinity and achieves 14 microns/pixel spatial resolution at closest approach (Edgett *et al.*, 2012). MastCam images and image mosaics were scaled and correlated with the HiRISE images via knowledge of camera azimuth and field of view, as well as through knowledge of the relationship between camera focal distance and focus motor position. MAHLI images were scaled on the basis of knowledge of the relationship between camera focal distance and focus motor position (Edgett *et al.*, 2012). Photoshop™ was used for processing and compositing images.

CheMin is the miniaturized X-ray diffraction/X-ray fluorescence (XRD/XRF) instrument inside the body of the Curiosity rover. The instrument uses a Co X-ray tube to interact with a powder sample (<150 μm) in transmission mode, and diffracted and fluoresced X-rays are recorded on a two-dimensional CCD detector. A conventional one-dimensional XRD pattern is produced by circumferentially integrating the Debye rings on the CCD (Bish *et al.*, 2014). X-ray diffraction data are analysed using conventional searches of the Powder Diffraction File, and quantitative analyses are done using the Rietveld method (Bish & Post, 1993) or full-pattern fitting methods (FullPat, Chipera & Bish, 2002).

Geochemical models of reaction of mudstone detritus with its pore fluid were executed with computer program CHIM-XPT (Reed, 1998) using the BRGM data base for aqueous and mineral thermodynamic properties (Marty *et al.*, 2015). Program CHIM-XPT applies equilibrium constants to compute the compositions and quantities of aqueous, gas and mineral phases at chemical equilibrium for any given bulk composition.

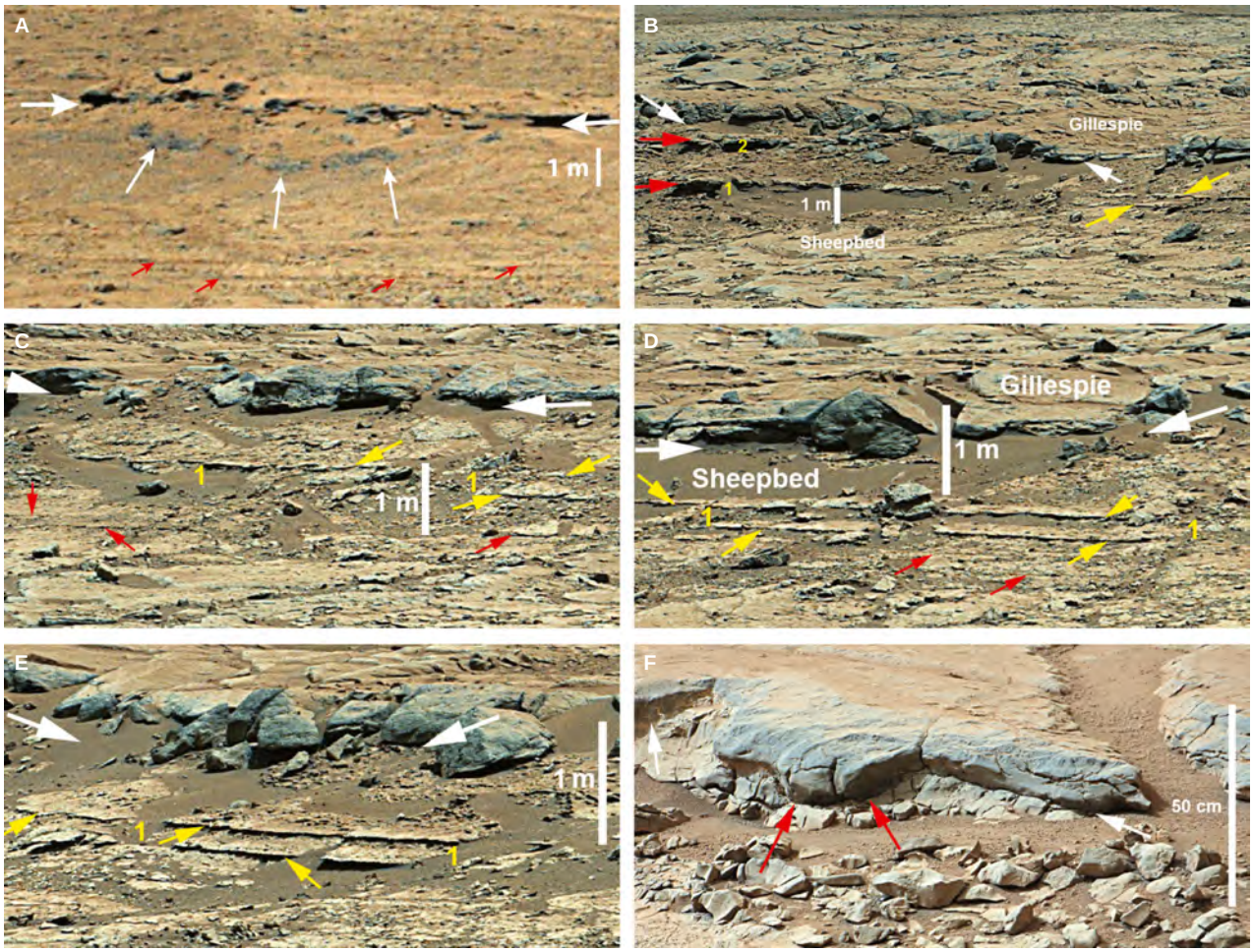

Fig. 3. Details from panoramas (B) and (C) in Fig. 2. The lettering of images corresponds to white lettering used in Fig. 2. All distances refer to distance between Sol 137 location (Fig. 2) and escarpment that marks the Sheepbed/Gillespie contact in a given image. (A) Distal (164 m NE of Sol 137 location) view of escarpment that shows the Sheepbed/Gillespie contact (marked with white arrows in this and following images), and a more resistant rock body with a concave base (small arrows) within the Sheepbed unit. Mastcam Right images 0137ML0008180250104170E01 and 0137ML0008180000104145E01. (B) Well-developed bedding in the Sheepbed mudstone (75 m distance). At left two thick resistant beds (*ca* 15 cm thick, levels 1 and 2, red arrows), probably sandstones based on their weathering resistance. They show internal stratification and appear to thin towards the right. The upper bed, marked 2, is truncated at the Sheepbed/Gillespie contact (white arrows), the lower one, marked 1, seems to pass into a thinner and less resistant bed to the right (upper yellow arrow). The lower yellow arrow points to a similar bed that appears to be covered to the left. At this location, the truncation surface cuts down about 50 cm into the Sheepbed mudstone. Mastcam Right images 0147MR0008340000201175E01 and 0147MR0008340010201176E02. (C) About 61 m distant, the level 1 couplet of resistant beds (yellow arrows) from previous image, and additional resistant beds below them (red arrows). Mastcam Right images 0147MR0008340020201177E01 and 0147MR000 8340030201178E01. (D) The same couplet (yellow arrows) at *ca* 51 m distance, as well as stratigraphically lower positioned resistant beds (red arrows). Mastcam Right image 0147MR0008340040201179E01. (E) Continuation of level 1 couplet at *ca* 41 m distance. Mastcam Right 0147MR0008340060201181E01. (F) The base of the Gillespie sandstone with a deep scour (red arrows) into the Sheepbed mudstone. The scour surface shows up to 25 cm relief. Mastcam Right image 0137MR0008170280200961E01.

Aeolian abrasion of mudstones as a source of insight

Because present-day aeolian abrasion has in places enhanced subtle textural details of these rocks, and because of a current lack of information on aeolian abrasion of mudstones on Earth, experiments were conducted to better understand textural features produced by aeolian erosion of mudstones. Likely water-associated

sedimentary rocks on Mars appear to be restricted to its earliest history (Malin & Edgett, 2000; Carr & Head, 2010), the Noachian (Nimmo & Tanaka, 2005). Later time periods appear to record a shift to much drier conditions and a thinner atmosphere (Bibring *et al.*, 2006). The shift from a 'wet' to a 'dry' Mars is thought to have occurred in the Late Noachian (Bibring *et al.*, 2006), and thus for the past 3·7 billion years aeolian processes were the predominant erosional forces, largely responsible for the landforms seen on Mars today. In the case of Yellowknife Bay, dating of exposure ages (Farley *et al.*, 2014) indicates that the escarpment that marks the top of the Sheepbed mudstone (Figs 1 and 2) retreated at a rate of approximately 0·75 m/Ma. On Earth, where scarp retreat in desert areas proceeds 3 to 4 orders of magnitude faster (Schmidt, 1989; Parsons & Abrahams, 2009), the main agent for breaking down and eroding mudstones is water, even in areas that receive very little rainfall. It is therefore very difficult to observe aeolian abrasion in terrestrial mudstone exposures. The Sheepbed mudstone, in contrast, shows a wide variety of surface textures produced by aeolian abrasion. In order to extract maximum insight from these textures, an extensive series of aeolian abrasion experiments was conducted on mudstone samples and experimental analogues (Howald & Schieber, 2009; Wilson *et al.*, 2011; Rossman *et al.*, 2012). The results of these experiments are used to interpret the features observed on Mars. Even without the benefit of petrographic information from thin sections, through experimentally produced textural analogues at the centimetre to sub-millimetre scale it is still possible to make informed deductions on the level of cementation, compositional homogeneity and relative rock hardness. Data on which the conclusions in this paper are based are archived in the Planetary Data System (pds.nasa.gov).

PHYSICAL SEDIMENTOLOGY OF THE SHEEPBED MUDSTONE

Subdivisions

Images of Yellowknife Bay show an approximately 5 m wide fringe zone (informally called Sheepbed unit 2) that follows the escarpment and erodes differently from the stratigraphically lower bulk of the Sheepbed mudstone exposed in the central portions of the bay (informally called Sheepbed unit 1). This subdivision is clear in outcrop (Figs 1A and 4A) and is even visible from orbit (Fig. 2A) where unit 1 is characterized by metre and decametre-scale polygons (Fig. 1A). When viewed in more detail, these polygons resolve into convexly abraded slabs of rock (Fig. 4A) with smooth and undulating surfaces that are separated by sand and debris filled cracks (Fig. 4A and B).

Sheepbed unit 2 does not show the well-developed large polygons seen in Sheepbed unit 1 (Fig. 4A) and instead has in many places a 'rougher', sharp-edged appearance (Fig. 4C) and a variety of presumed diagenetic features, such as raised ridges and millimetre-size spherical nodules (Grotzinger *et al.*, 2014; Siebach *et al.*, 2014; Stack *et al.*, 2014).

Layer characteristics

There are only a small number of close-up Mastcam images of Sheepbed unit 1, but in one of these a polygon margin has been exposed by aeolian processes and shows faint but clearly visible parallel layering at the millimetre to centimetre-scale (Fig. 5A). In places thin horizons with small millimetre-size nodules have been observed as well.

The majority of close-up Mastcam images are from Sheepbed unit 2, predominantly in the vicinity of the John Klein and Cumberland drill sites (Figs 1 and 2, locality G). Most of these images were taken in support of drill site characterization at a high angle and thus preferentially show bedding plane features. After scrutinizing all images, however, for beds exposed in cross-section, a number of places were found where side views of beds show finer scale layering (Fig. 5). In places aeolian abrasion of bed surfaces has exposed millimetre-scale parallel laminae (Fig. 5E and F).

In addition to these subtle expressions of stratification, there are also beds that are prominent in outcrop and can be identified in multiple areas of the western Yellowknife Bay outcrop area (Figs 1 and 2). These layers form continuous beds of 5 to 10 cm thickness in the basal portions of Sheepbed unit 2 (Fig. 6) and show a variety of diagenetic features, presumed to be mineralized synaeresis cracks and small nodules (Siebach *et al.*, 2014; Stack *et al.*, 2014). The resistance to erosion of these beds is such that it causes them to form steps in outcrop where overlying mudstone has been

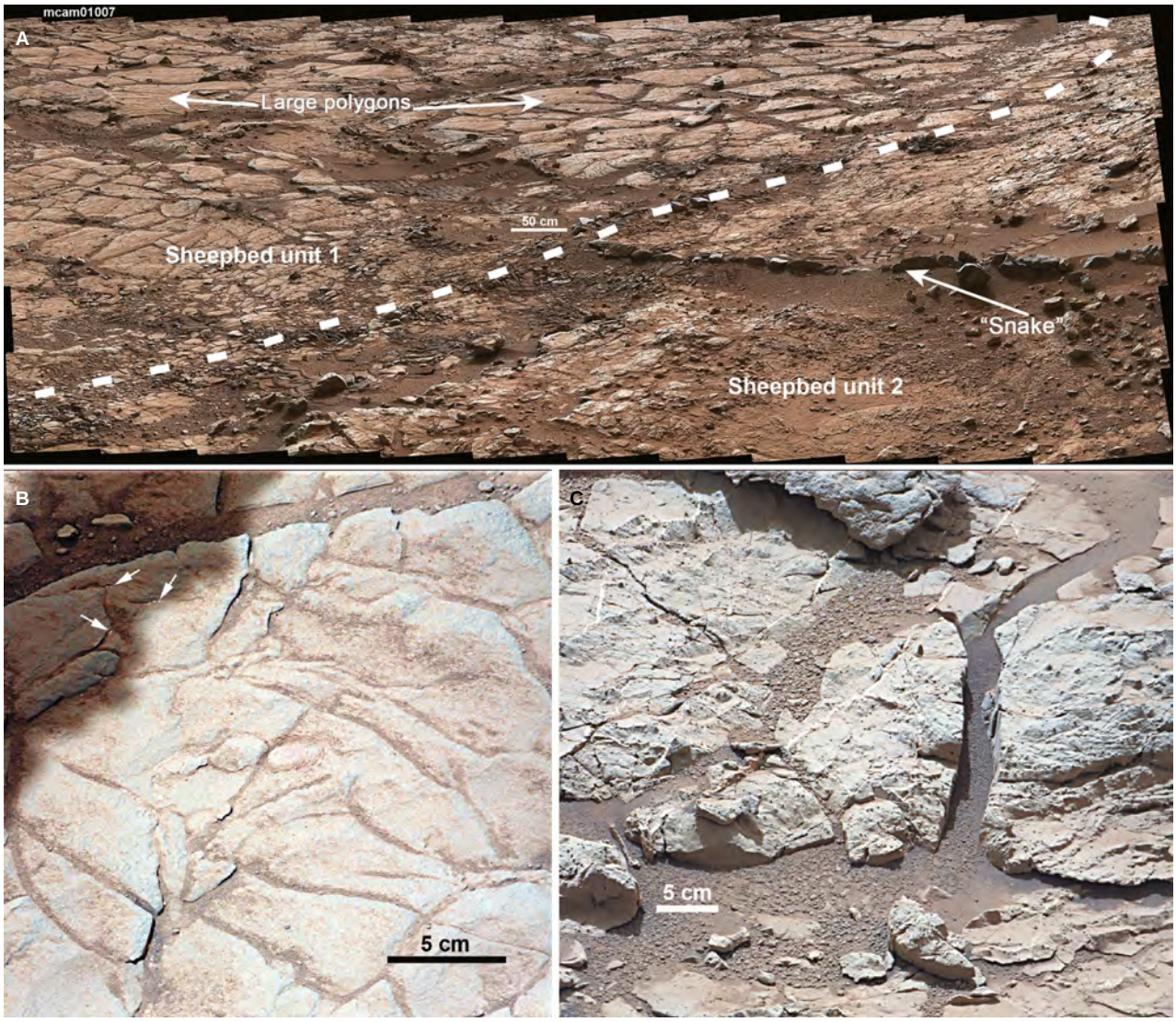

Fig. 4. (A) Dashed line separates Sheepbed unit 1 (on left, large low-amplitude convex smooth polygons) from Sheepbed unit 2 (on right, hackly weathering, smaller fragments). The cross-cutting feature named 'snake' has been interpreted as a clastic dyke of sandstone composition (Grotzinger *et al.*, 2014). Portion of a Mastcam Right mosaic from Sol 198 (mcam01007). (B) Closer view of smoothed polygon surface in Sheepbed unit 1. Debris filled crack near top of image. White arrows point to white crack fills of $CaSO_4$ (anhydrite). Mastcam Right image 0129MR0007940010200824E01. (C) Contrasting appearance of Sheepbed unit 2 with sharp edged crack margins, ragged surfaces and sub-millimetre nodules (Grotzinger *et al.*, 2014). Mastcam Right image 0126MR0007 800000200786E01.

removed. Whether these beds represent physical sedimentation events or are merely an expression of post-depositional cementation will be discussed in detail in the following section on diagenesis. There are also thin resistant layers from a few millimetres to a centimetre thickness that project horizontally out of the outcrop because mudstone above and below has been removed (Fig. 6). The authors do not know the grain size of these particular layers, but presume that they are comparable to similar appearing layers at the John Klein drill site (Fig. 7). At the latter location, due to the gentle slope of the Sheepbed unit 2 outcrop, these highly resistant and probably well-cemented layers can form large bedding plane exposures in the course of aeolian erosion.

The Sheepbed layers in Fig. 7 are more or less horizontal, and in image they have an apparent dip towards the viewer due to the downward tilt of the Mastcam cameras when the images were acquired. The exposure surface 'climbs' through the stratigraphy at a low angle towards the

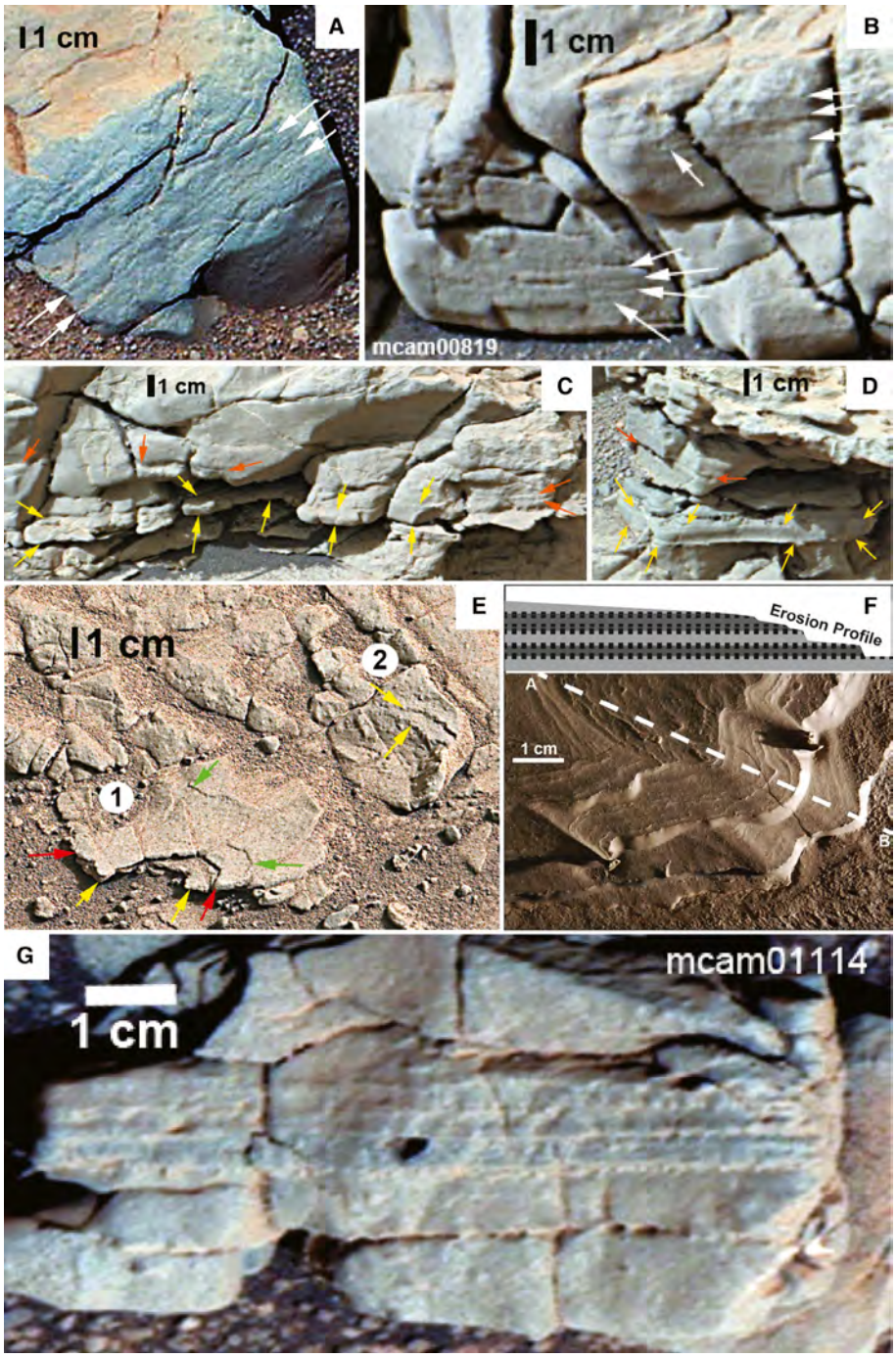

Fig. 5. (A) Side view of a piece of mudstone polygon in Sheepbed unit 1. Arrows point to faintly developed internal parallel layers at the centimetre-scale. Mastcam Right image 0297ML0012420030106392E01. (B), (C) and (D), examples of millimetre to centimetre-scale internal layering in Sheepbed unit 2. White arrows point to largely parallel laminae, red arrows mark laminae that can only be traced for short distances, and yellow arrows mark thin beds. Thin bed in (D) has a more resistant base, might be graded. (B) Mastcam Right image 0138MR0008190650201079E01, (C) Mastcam Right image, 0138MR0008190620201076E01, (D) Mastcam Right image 0138MR0008190610201075E01. (E) A bed surface with traces of resistant laminae (locations 1 and 2, arrows) that look like they might have been 'etched out' by aeolian abrasion. Mastcam Right image 0147MR0008350010201199C00. (F) Lower portion shows terrestrial shale where experimental aeolian abrasion accentuated differences in layer hardness that look very similar to what is seen in (E). Upper portion shows step-wise erosion of shale laminae in cross-section along white dashed line A–B. Dotted black lines mark thin sub-millimetre silt laminae that are better cemented. (G) Millimetre-scale parallel laminae in a piece of Sheepbed float. Mastcam Right image 0234MR0011140180203149E01.

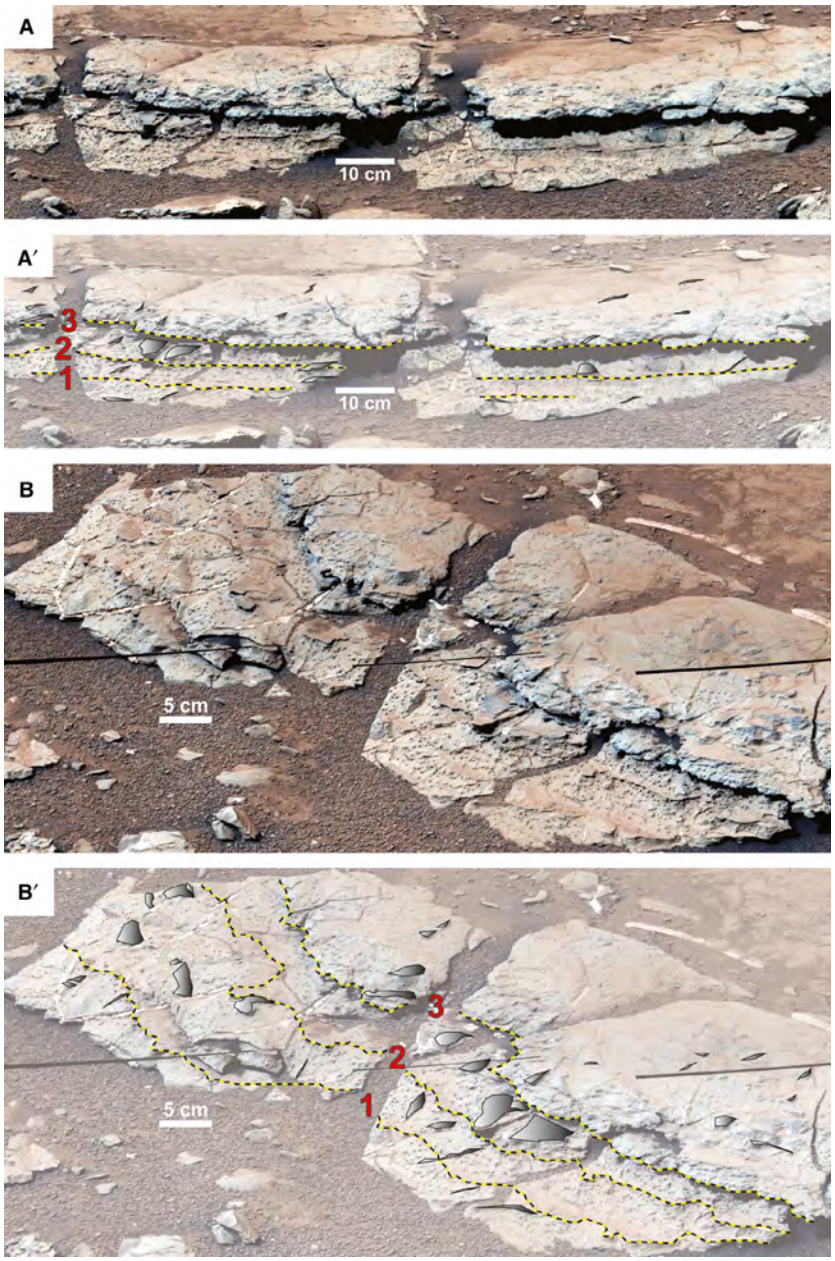

Fig. 6. Prominent layering in the lower portion of Sheepbed unit 2. This interval is more weathering resistant due to diagenetic cements (matrix cement and millimetre-sized nodules) and forms a 'step' as the outcrop slopes gently between Sheepbed unit 1 and the Sheepbed/Gillespie contact (Fig. 2B). In both (A) and (B) three thin resistant layers, a few millimetres in thickness, have been sculpted out by aeolian abrasion. These layers are traced with dashed yellow-black lines in images A′ and B′. This interval also shows multiple 'raised ridges' (marked as polygons with grey scale gradient in A′and B′), interpreted as mineralized synaeresis cracks (Grotzinger *et al.*, 2014; Siebach *et al.*, 2014). In places, 'raised ridges' cut across resistant layers 1, 2 and 3. Note that the upper surface of this more ragged looking interval is comparatively smooth and flat, except where ornamented with 'raised ridges': (A) is a portion of a Mastcam Right mosaic acquired on Sol 297 (mcam01238), images 0297MR0012380120203571E01 and 0297MR0012380170203576E01; (B) is a Mastcam Right mosaic acquired on Sol 298 (mcam01246), images 0298MR0012460000203669E01, 0298MR0012460010203670E01, 0298MR0012460020203671E01, 0298MR0012460030203672E01, 0298MR0012460040203673E01 and 0298MR0012460050203674E01.

Gillespie contact (data not shown). These geometric relations imply that the foreground in Fig. 7A is stratigraphically lower than the background of the image, that there are three layers of rock from bottom to top (Fig. 7A'), and that a thin resistant layer separates the basal two layers (Fig. 7A'). That such a layer exists is illustrated in Fig. 7B where 'raised ridges' cut across a basal flat layer at various angles. Near these 'raised ridges' there can locally be some upward deflection of the basal layer, but overall it gives the appearance that it was a continuous layer prior to fracture formation (Fig. 7B). This basal layer has been exposed because the overlying softer mudstone has largely been removed by aeolian erosion. An edge of the basal layer had been cleaned in one location by the wind and fortuitously captured in a MAHLI close-up, and the image suggests that this basal layer is a fine to very fine sandstone. In the enhanced MAHLI image it is apparent that there are abundant grains in the very fine sand size range (62·5 to 125 μm; Fig. 7C3), and that there is a clear textural difference relative to the grain size observed in the mudstones at the John Klein locality (Fig. 7C1 and C2).

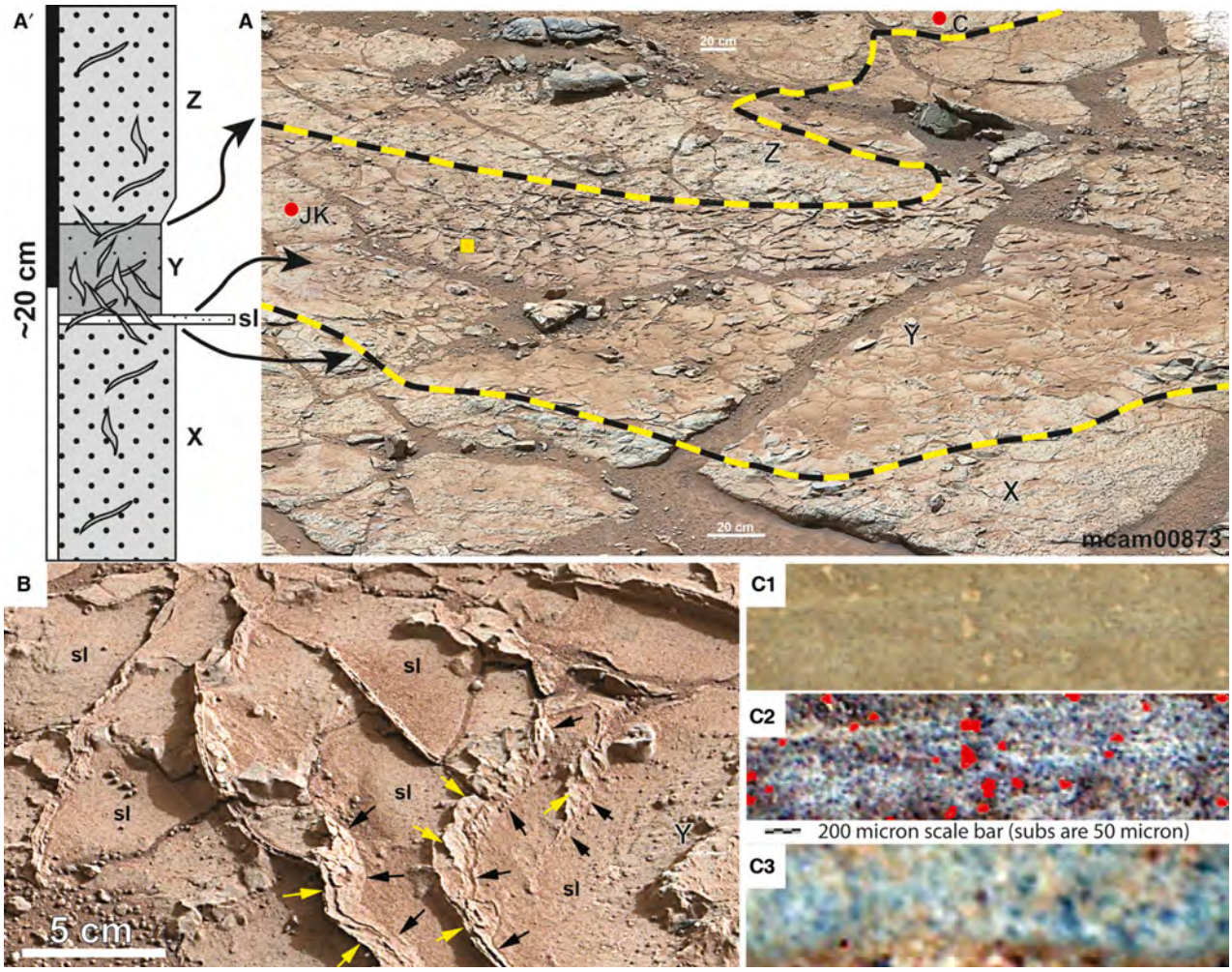

Fig. 7. (A) and (A′) Small-scale stratigraphic relationships at the John Klein locality. The outcrop slope and bed attitude suggest that below the ridge-bearing interval (layer Y), there is a mudstone with millimetre-sized nodules (layer X), and that the ridge-bearing layer is overlain by another mudstone (layer Z) with millimetre-sized nodules. Approximate boundaries are drawn as yellow-black dashed lines. Red circles mark the John Klein and Cumberland drill sites: (A) is a Mastcam Left mosaic acquired on Sol 162 (mcam), images 0298MR0012460000203669E01, 0298MR0012460010203670E01, 0298MR0012460020203671E01, 0298MR0012460030203672E01, 0298MR0012460040203673E01 and 0298MR0012460050203674E01. (B) A closer view of the ridge-bearing surface shows a basal planar layer (sl; presumed sandy) that is cross-cut by 'raised ridges'. Ridges can be either vertical or cut through obliquely (yellow arrows). Black arrows mark the break between the basal sandy layer (sl) and the ridges. Some of the vertical ridges show symmetrical internal layering, probably isopachous cements. At right there is sediment of layer Y that is still being eroded. Elsewhere erosion has 'cleaned off' the softer material, of layer Y, and exposed the surface of the resistant sandy layer. Mastcam Right images 0164MR0008850100201599E01 and 0164MR0008850110201600E01. (C) Comparison of grain size in basal layer (sl) with grain size typical for Sheepbed mudstone. (C1) MAHLI image from Ekwir brush spot (Sol 150, 0150MH0001690010101421C00), brownish-beige spots are surficial sand grains; (C2) enhanced version of C1 (aeolian dust marked in red). (C3) MAHLI close-up of resistant basal layer (sl) that appears definitely coarser and has grains in the very fine to fine sand size range (0165MH0001880010101995C00). MAHLI, Mars Hand Lens Imager.

Interpretation of Sheepbed mudstone stratification

Collectively, the observations presented here suggest that the presumed lake basin received sediment pulses that were associated with localized scouring (Fig. 3A) and also produced beds of considerable lateral continuity and rather uniform thickness (Fig. 3). Some of the beds that presumably resulted from these sedimentation events are clearly visible and traceable over distances of 100 m or more, judging from outcrop and orbital images (Figs 2 and 3), whereas others are less prominent and thinner (marked with red

arrows in Fig. 3A, C and D), perhaps suggesting smaller sediment pulses or a more distal source. The couplet marked '1' in Fig. 3 has a thickness of *ca* 10 cm across the outcrop, and probably is equivalent to the rock interval seen in detail in Fig. 6. Although there are three resistant layers visible in Fig. 6, only two of them are prominent, and the thickness of the layered interval is *ca* 10 cm. Uniform thickness across the extent of the imaged exposure (*ca* 100 m) implies a depositional process that spreads sediment out evenly, a quality more commonly associated with flows that drop sediment from suspension (density currents) than with distribution of sediment by bedload transport (Reineck & Singh, 1980).

Although it was noted in earlier publications that there are centimetre-scale scours at the base of the Gillespie sandstone (Grotzinger *et al.*, 2014), looking at the contact over a larger extent (Figs 2 and 3) shows downcutting of as much as 50 cm and truncation of beds in the Sheepbed member (Fig. 3B), as well as localized scours of decimetre scale (Fig. 3G). As also seen in Fig. 3, in spite of variable thickness of the Gillespie member (Grotzinger *et al.*, 2014) there is no apparent deformation of the underlying Sheepbed member, indicating that the latter was consolidated by the time of Gillespie deposition. In combination with an abrupt change in lithology from mudstone to coarse sandstone and significant intervening erosion, these features strongly suggest that the contact between Sheepbed and Gillespie marks a disconformity rather than simply a shift of sedimentary facies from lacustrine to fluvial.

In the context of what is already known about modern and ancient lake systems on Earth, the Sheepbed member appears to consist of multiple event beds of a thickness of a few centimetres to decimetres, and probably more slowly deposited interlayers (Fig. 5). More sandy channelized portions (Fig. 3A) and finer flanking deposits (Fig. 3B) are consistent, for example, with river-fed hyperpycnal flows as observed in modern lake systems (Houbolt & Jonker, 1968; Sturm & Matter, 1978). In the context of a lake basin located at the terminus of alluvial fans (Grotzinger *et al.*, 2014), episodic sediment gravity flows that deliver coarse sediment into deeper water would be intercalated with basinal muds (Renaut & Gierlowski-Kordesch, 2010) and produce the bedding observed in the Sheepbed member (Fig. 3). In ancient and modern lake beds on Earth, comparable event beds have also been interpreted as distal sheet flood deposits in playa lake settings (Talbot & Allen, 1996), but a lack of features suggestive of wave reworking and desiccation (Hardie *et al.*, 1978) in the Sheepbed member (Grotzinger *et al.*, 2014) does not support such an interpretation. Under the assumption that the lake was comparatively long-lived, alluvial fans feeding sediment into an overfilled lake basin (Bohacs *et al.*, 2000) appears to be a more applicable model.

Apart from the bedding features described above, the Sheepbed mudstone gives the initial impression of a rather featureless and 'massive' mudstone. As Fig. 5 indicates, however, this perception may simply be a matter of insufficient images of bed cross-sections. The millimetre to centimetre-scale layers that can be seen are in keeping with the scale of layering that is encountered in profundal and pelagic deposits of perennial lakes on Earth. There these layers record fine-grained sediment supply from suspension settling as well as bedload transport (Reineck & Singh, 1980; Renaut & Gierlowski-Kordesch, 2010), with sediments derived from detrital input by rivers, littoral erosion and supplemented by aeolian material. Details of composition and sedimentary textures allow differentiation between sources and delivery processes (Reineck & Singh, 1980; Renaut & Gierlowski-Kordesch, 2010), but that level of detail is lacking for the Sheepbed mudstones. Given the general setup with alluvial fans at the lake margins (Grotzinger *et al.*, 2014), the authors surmise that the millimetre to centimetre-scale layering seen in Fig. 5 reflects distal pulses of fluvial sediment input (fine-grained turbidites or muddy hyperpycnites) combined with fall-out from river plumes and possibly some aeolian supply.

POLYGONAL CRACKS AND THEIR SIGNIFICANCE

Although the present authors do not consider the metre to decametre-scale polygonal cracks visible from orbit (Fig. 2) as a feature that relates to the depositional history of the Sheepbed mudstone, this feature has been discussed previously by Hallet *et al.* (2012) and Sletten & Hallet (2014). The latter authors concluded that the polygons reflect contraction of a layer of sediment, and that this contraction was consistent with desiccation of fine-grained clay rich deposits, possibly analogous to formation of large polygonal crack networks in drying terrestrial playa lake deposits (Antrett *et al.*, 2012). Yet, although the geometry of the latter compares

well with what can be seen in Yellowknife Bay (Fig. 2), the fact that the cracks are filled with modern day surface debris (Fig. 4) is more difficult to explain. If these cracks had formed in the context of desiccating lake muds, they should have been filled with sediment (sand and/or mud) that subsequently would have been lithified to the same degree as the host mudstones. However, none of the Mastcam or MAHLI images taken of polygonally fractured mudstone surfaces show any evidence of preserved lithified crack fills. Instead, the cracks are invariably filled with loose surface debris that was transported across the surface by currently active aeolian processes. This observation is consistent with an alternative scenario where contraction occurred when smectite-rich sediment layers were exposed by erosion to the very dry (Harri *et al.*, 2014) modern Martian atmosphere. Expanded smectites (basal layer spacing of ≥15 Å) deposited in an aqueous environment (Grotzinger *et al.*, 2014) should maintain their interlayer water after burial. Once exposed again to the very dry contemporaneous Martian atmosphere, however, these smectites would probably have collapsed due to dehydration (basal spacing *ca* 10 Å), a volume reduction by at least one-third. In one of the XRD samples (John Klein, Vaniman *et al.*, 2014), a 10 Å collapsed smectite constitutes about 20% of the sample, and thus one can estimate that the rock volume would have decreased by *ca* 10%. Thus, metre-scale polygons should be separated by debris filled cracks that are in the 10 to 20 cm width range, and smaller polygons should be separated by crack fills of a few centimetres width. This conclusion agrees well with the crack fills that can be seen, for example, in Fig. 4A (as well as other images of the Sheepbed surface), and suggests that present-day dehydration of exposed smectite-rich strata can explain the polygonal crack patterns in the Sheepbed mudstone. The Sheepbed clay mineral analyses (Vaniman *et al.*, 2014) are from Sheepbed unit 2, an interval characterized by extensive stratiform cementation (see below) that should lessen potential contraction due to smectite dehydration. This prediction is borne out by the observation that the Sheepbed unit 2 forms a fringe around Yellowknife Bay in which polygon development is less prominent (Fig. 2). In that context, the more prominent polygon development in Sheepbed unit 1 (Fig. 2) may actually point to higher clay mineral contents (relative to the John Klein and Cumberland drill sites) in Sheepbed unit 1.

PERSPECTIVES ON THE ORIGIN OF CLAYS

Whether Sheepbed clay minerals are authigenic or detrital has a direct bearing on how best to interpret diagenetic features such as nodules and synaeresis cracks (Grotzinger *et al.*, 2014). To address the origin of the clay minerals, the two XRD analyses reported by Vaniman *et al.* (2014) and Bristow *et al.* (2015) and 18 whole-rock APXS analyses reported by McLennan *et al.* (2014) from the Sheepbed mudstone are considered here. One APXS analysis (target Mavor) was excluded because it is an analysis with a large calcium sulphate vein component (28% SO_3). These data contain critical information on the composition and mineral content of these rocks that illuminate the origin of the clay minerals detected in the Sheepbed mudstone. On Earth, mudstones invariably contain detrital clays because weathering of all but a few rock types produces clay minerals in abundance (Potter *et al.*, 2005), and detrital clay minerals in mudstones are therefore taken for granted. Thus, when abundant clay minerals (*ca* 20%) were detected in the Sheepbed mudstone (Vaniman *et al.*, 2014), the initial assumption was that these clays were mostly detrital, having been carried in by rivers from the highlands surrounding the crater. However, because existing knowledge about Martian surface processes in the distant past is limited, Mars explorers must exercise caution so as not to over-extend conclusions derived from limited data.

Alpha particle X-ray spectrometer (APXS) analyses

Al_2O_3 – CaO+Na_2O – K_2O ternary diagrams are commonly used to illustrate weathering trends (Nesbitt & Young, 1984), and the APXS whole-rock data reported by McLennan *et al.* (2014) cluster tightly (Fig. 8) near the composition of Martian basalts (McSween *et al.*, 2006a,b) and the Martian crustal average (Taylor & McLennan, 2009). Because of this, the conservative assumption was made that the Sheepbed mudstones were derived from unweathered source rocks of average crustal composition (McLennan *et al.*, 2014), and that after deposition these sediments underwent isochemical alteration that produced the observed clay minerals (McLennan *et al.*, 2014; Vaniman *et al.*, 2014). Given that fine-grained sediments with abundant volcanic components (for example, ash

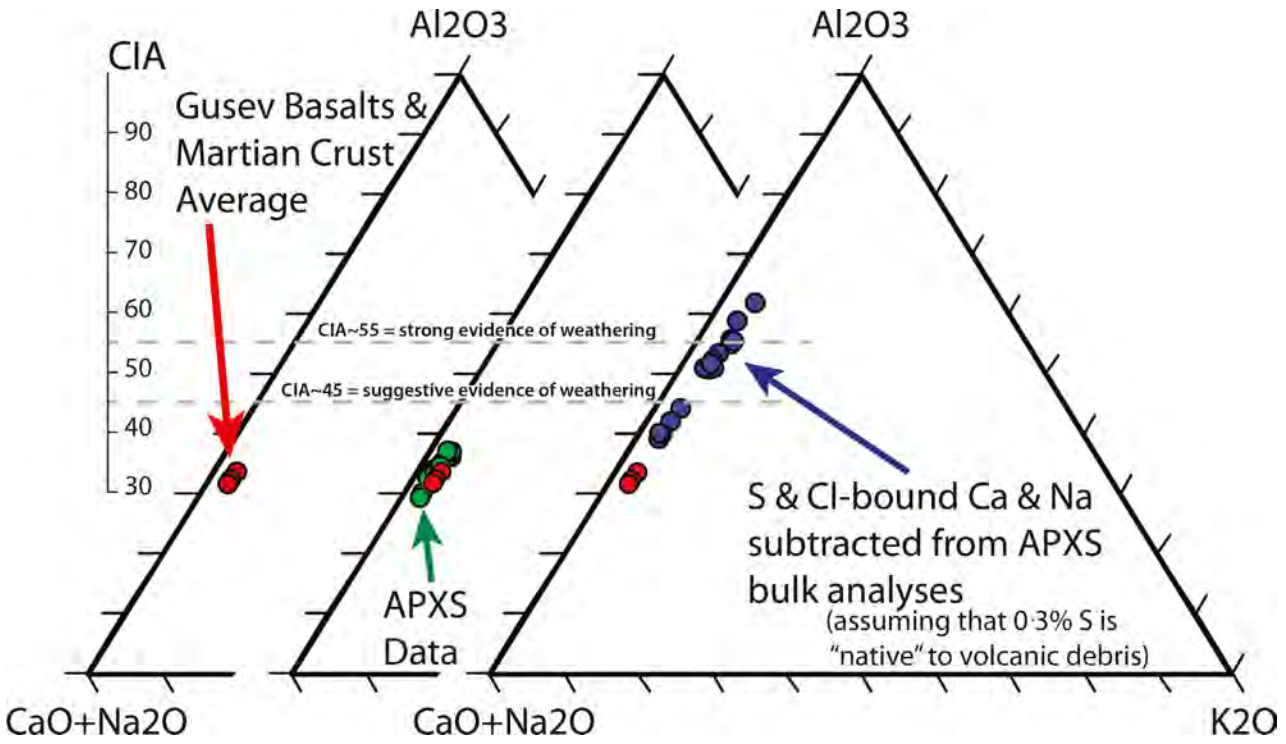

Fig. 8. Plots of potential source rocks and Sheepbed APXS data (from McLennan *et al.*, 2014) with regard to the molar proportions of the elements that constitute the chemical index of alteration (CIA; Nesbitt & Young, 1982). The left plot shows the position of the Martian crustal average (Taylor & McLennan, 2009) and basalts from Gusev crater on Mars (McSween *et al.*, 2006a,b). The middle plot shows in addition the positions of APXS data as reported by McLennan *et al.* (2014), and the tight clustering of these analyses near the crustal and basalt compositions. The right plot shows APXS analyses from the Sheepbed member that have been 'corrected' for that amount of Ca and Na that are probably bound to sulphur and chlorine. The whole-rock APXS analyses plotted here were reported by McLennan *et al.* (2014), and that publication also contains information on methodology and instrumentation as well as further references. APXS, Alpha Particle X-Ray Spectrometer.

beds) on Earth are liable to experience intense alteration and formation of clay minerals (smectites) during diagenesis (e.g., Potter *et al.*, 2005), formation of diagenetic clays might be expected in Martian muds that initially must have contained grains derived from volcanic source rocks (Grotzinger *et al.*, 2014; McLennan *et al.*, 2014).

All APXS whole-rock analyses contain variable amounts of sulphur (up to 9% as SO_3) and up to 2% chlorine (McLennan *et al.*, 2014). Given that Martian basalts do not exceed 0·3% S (McSween *et al.*, 2006a,b), and given that $CaSO_4$ was observed in hair-line fractures within drill holes (Grotzinger *et al.*, 2014) and occurs as anhydrite and lesser bassanite in XRD analyses of these rocks (Vaniman *et al.*, 2014), it is plausible that most of the sulphur in these rocks is in $CaSO_4$ and probably was introduced during diagenesis and burial from external sources (Schieber, 2014). Vaniman *et al.* (2014) also report trace halite, and thus a parallel argument can be made that chlorine is most likely in halite. It should be noted, however, that further analysis here of the XRD data for John Klein and Cumberland do not support the presence of halite above the limit of detection. The Gusev basalts (Fig. 8) were analysed with an APXS instrument of the same design as the one carried by Curiosity and no appreciable amounts of chlorine were reported from them (McSween *et al.*, 2006a,b). These observations imply that the original sediment at Sheepbed (presumed fine-grained basaltic-volcanic debris) is not a likely source of chlorine and instead suggests that chlorine was derived from basin waters or introduced later in diagenesis. With the bulk of the sulphur and all of the chlorine in the Sheepbed APXS analyses most likely not derived from alteration of original detrital grains, the contention here is that the Na and Ca in halite and anhydrite should be removed from the original analyses to determine

the composition of the original sediment. In particular for calculations of the chemical index of alteration (CIA), as defined by Nesbitt & Young (1982), failure to remove non-rock $CaSO_4$ and NaCl yields unrealistically low CIA values. The result of removing $CaSO_4$ and NaCl from the Sheepbed analyses is shown in Fig. 8 (plot on the right). Although the raw data are tightly clustered (Fig. 8, middle plot), the corrected data show a clear shift of all data towards the Al_2O_3 pole of the diagram and they plot on weathering trajectories as described by Nesbitt & Young (1984).

Vaniman *et al.* (2014) report akaganéite, an iron oxide that may contain chlorine, from the Sheepbed XRD samples that probably formed during diagenesis. If akaganéite-bound Cl is used to reduce the Cl correction applied in Fig. 8 to CIA data, the change in CIA numbers is negligible (a fraction of a per cent).

The observation that the salt-corrected APXS compositions all shift to various degrees towards the Al_2O_3 corner of the diagram suggests derivation of the sediments from a source area wherein variably altered rock units were exposed. Even when the data are viewed conservatively and only rocks with a CIA above 45 are considered weathered (McLennan *et al.*, 2014), a dozen of the plotted data points indicate weathering of variable intensity. The lake in which the Sheepbed mudstone was deposited was fed by the Peace Vallis alluvial fan system that received water and sediment from a 730 km^2 catchment that drains the adjacent upland plains (Palucis *et al.*, 2014). Within this catchment a vertical thickness of 2 km of Martian upper crust is exposed (Palucis *et al.*, 2014), which contributed sediment to the fan and the lake at its terminus.

Edgett & Malin (2004) and Malin *et al.* (2010a) describe the Martian upper crust as a layered, cratered and 'valley-ed' volume that consists of filled and buried craters and valley networks at many scales and stratigraphic levels. The layers within this volume are a mixture of volcanic deposits, ejecta blankets and sedimentary deposits, with the latter containing abundant evidence for deposition by flowing water (Malin & Edgett, 2000). Aqueous transport and deposition of sediment implies a moist regolith with the likely formation of clay minerals as a result of soil-forming processes (e.g. Craig & Loughnan, 1964; Singer, 1980). Clay minerals in Martian upper crustal rocks may also have formed from impact-related hydrothermal alteration (Newsom *et al.*, 2004). Given the likely varied source area it is plausible that variably weathered rocks contributed sediment to the lake basin, and that clay minerals were part of that sediment input. The weathering trends shown by APXS analyses (Fig. 8) support such a conclusion.

X-ray diffraction analyses

Further support for the input of detrital clays comes from a re-examination of the XRD data (Vaniman *et al.*, 2014) measured for two Sheepbed mudstone samples, Cumberland and John Klein. These XRD samples were collected in close lateral (<3 m) and stratigraphic (<10 cm) proximity, and although both XRD patterns are quite similar for diffraction angles >12° 2θ, they differ significantly at lower angles (Fig. 9). The John Klein sample shows the presence of a dominant *ca* 10 Å clay mineral, consistent with an iron-rich smectite such as nontronite (Bish & Milliken, 2015) or saponite (Bristow *et al.*, 2015), whereas the Cumberland sample is dominated by a *ca* 14 Å clay mineral that is consistent with a partially chloritized smectite (Bristow *et al.*, 2015). However, there is also clear evidence for a small 10 Å component in the Cumberland sample and a small 14 Å component in John Klein. Some have suggested (Vaniman *et al.*, 2014; Bristow *et al.*, 2015) that the 10 Å clay resulted from dehydration-induced collapse of an expanded smectite of the 14 Å component, but that interpretation is unlikely because the 14 Å clay in the Cumberland sample did not collapse after being stored for several months at the very low relative humidity inside the CheMin instrument and re-analysing (Bristow *et al.*, 2015). Vaniman *et al.* (2014) interpreted the difference in clays as an indication that variable diagenesis had occurred in a mineralogically immature source rock with an abundance of reactive components. However, given that both samples contain the same suite of non-clay minerals (Vaniman *et al.*, 2014) and appear to contain a similar suite of amorphous components (for example, basaltic glass, etc.), the distinct difference with regard to clay minerals is unlikely to be secondary. These differences suggest as an alternative interpretation that at least one of the clay minerals (*ca* 14 Å and *ca* 10 Å) is detrital rather diagenetic in origin. Partial chloritization (*ca* 14 Å phase) of smectite is consistent with formation in: (i) a soil environment (e.g. Rich, 1968); or (ii) a low-

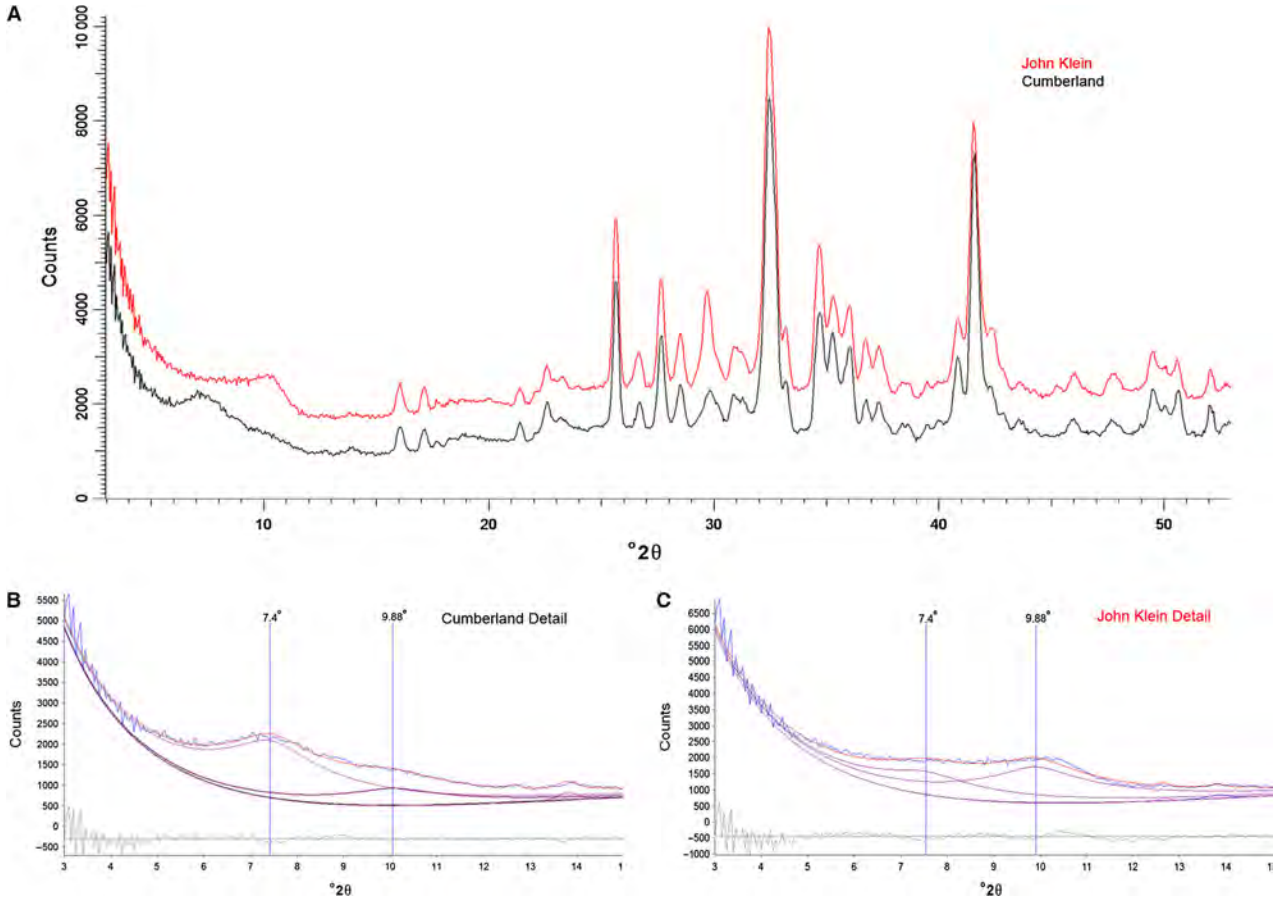

Fig. 9. (A) X-ray diffraction patterns of the two drill samples collected from the Sheepbed mudstone. The complete diffraction patterns illustrate how similar both samples are, with the exception of the clay mineral diffraction features at low angles. (B) and (C) Show the expanded low-angle portion of these patterns and illustrate the distinct difference in clay minerals between the two samples, with a pronounced broad 14 Å feature (with a lesser 10 Å feature) in the Cumberland samples and a pronounced 10 Å feature (with a smaller 14 Å feature) in the John Klein sample. Note scattering at small diffraction angles, a potential indication of a short-range ordered material such as Fe-allophone, a clay mineral precursor phase.

T reaction after burial (e.g. Salem *et al.*, 2000), similar to that evidenced in orbital spectroscopy (Sun & Milliken, 2015). Indeed, option (ii) was suggested for Mars clay minerals by Viviano *et al.* (2013). Given that the Peace Vallis fan system taps into 2 km of upper crustal strata (Palucis *et al.*, 2014) it appears plausible that chloritized smectites related to burial diagenesis or soil formation were part of the sediment load that was transported to the crater basin. The presence of two different clay minerals in both of these samples, in different proportions, suggests that at least one of the two is detrital. Their stratigraphic proximity makes it less likely that two different clay minerals formed in rocks that are otherwise mineralogically and compositionally very similar. Although the amount of pyrrhotite in both samples is close to the detection limits for CheMin, elimination of this phase in Rietveld models results in mismatched intensity in both patterns in the regions of the main pyrrhotite reflections. There is evidence for more pyrrhotite in Cumberland (*ca* 1·2% on an amorphous-free basis) than in John Klein (0·5% on an amorphous-free basis). Adjustment for amorphous components (Vaniman *et al.*, 2014) results in 0·8% and 0·3%, respectively.

Two additional points can be made in support of a detrital clay component for the Sheepbed mudstone. Firstly, in their initial paper on Sheepbed geochemistry, McLennan *et al.* (2014) proposed that detrital olivine reacted to form smectite and magnetite during diagenesis. Although the proposed reaction probably occurred, one should not presume that all of the observed clay minerals were produced

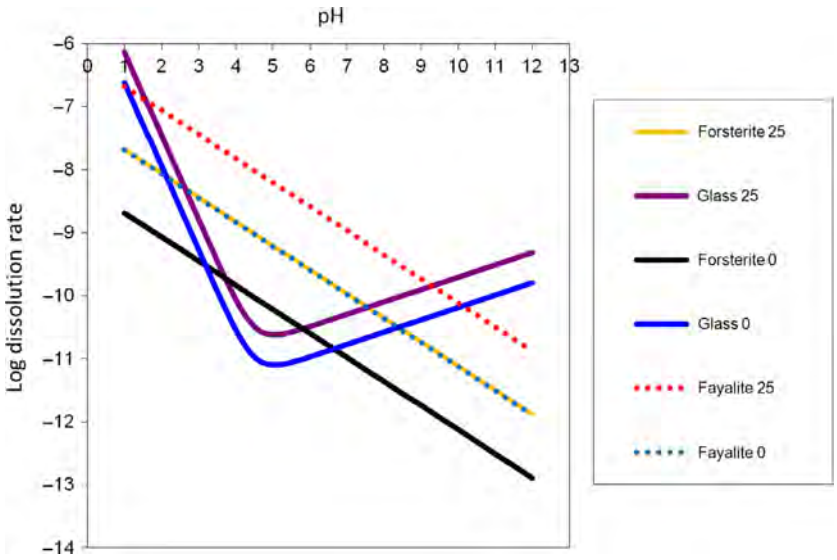

Fig. 10. Dissolution rate laws for fayalite, forsterite and basalt glass at 25°C and 0°C. From Bandstra & Brantley (2008), based on dissolution rates for olivine (Brady & Walther, 1989; Oelkers, 2001a; Pokrovsky & Schott, 2000; Rosso & Rimstidt, 2000; Wogelius & Walther, 1992), basalt (Gislason & Eugster, 1987) and published activation energies for olivine (Van Herk *et al.*, 1989; Wogelius & Walther, 1992; Jonckbloedt, 1998; Rosso & Rimstidt, 2000; Oelkers, 2001a,b) and basaltic glass (Gislason & Eugster, 1987; Gislason & Oelkers, 2003; Wolff-Boenisch *et al.*, 2004). The fayalite rate in Fig. 10 is estimated assuming that fayalite dissolves 10 times faster than forsterite (Bandstra & Brantley, 2008) as documented in the literature at acidic to neutral pH (Wogelius & Walther, 1992). Results indicate similar dissolution rates at near neutral conditions for each mineral, suggesting that extensive loss of basaltic glass would probably accompany extensive loss of olivine. However, Martian glass compositions may vary from basaltic glass composition. Proposed chemical compositions for the Mars amorphous material have much lower silica concentrations than basaltic glass (Dehouck *et al.*, 2014; Vaniman *et al.*, 2014) with enrichments of Ca and Mg, greatly destabilizing the glass, and higher concentrations of Al and Fe somewhat destabilizing the glass (Oelkers, 2001b). Therefore, the amorphous material on Mars would probably have a dissolution rate higher than the basaltic glass indicated here, indicating that even faster dissolution rates are likely.

by this reaction. Supporting evidence for the latter perspective comes from the XRD analysis of other samples in the course of the rover mission since the Sheepbed campaign. For example, our analysis of the XRD data for a mudstone sample from the location Telegraph Peak (Rampe *et al.*, 2016) at the Pahrump outcrop (Grotzinger *et al.*, 2015) contains Fe-forsterite and magnetite (3·6% and 14·2%, respectively, on an amorphous-free basis) but lacks any evidence for smectite, suggesting that the reaction proposed by McLennan *et al.* (2014) did not occur there (or only in a small amount) and that the magnetite may have been detrital rather than diagenetic. The second point relates to the observation that there is a significant and comparable (*ca* 30%; Vaniman *et al.*, 2014) amorphous component in the Rocknest, Cumberland and John Klein samples. The Rocknest sample was collected from a sand shadow and was considered to represent an unaltered mineralogy, with no clay minerals detected (Bish *et al.*, 2013). Although it is difficult to determine the exact nature of the amorphous component(s) in these three samples, they were well modelled by basaltic glass. Laboratory and field data show (Fig. 10) that basaltic glass and Fe-forsterite alter at comparable rates. Thus, it is unlikely that most, but not all, of the Fe-forsterite in each of these samples would have been altered to a clay mineral, leaving behind a significant amorphous component. The authors therefore consider the coexistence of an amorphous component with variable amounts of Fe-forsterite and one or two clay minerals to be inconsistent with an *in situ* alteration scenario.

The XRD data reported by Vaniman *et al.* (2014) show anhydrite and bassanite (Ca-sulphates) in John Klein and Cumberland, which are attributed to hairline fractures filled with $CaSO_4$. However, the possibility of a disseminated $CaSO_4$ component that resides in the mudstone pore spaces cannot be ruled out.

Modelling diagenetic clay formation

Although it is important to understand the potential detrital clay mineral supply to Gale crater, an abundance of thermodynamically unstable grains (for example, olivine and volcanic glass) suggests that low-temperature alteration minerals, such as zeolites and clay minerals may form. Such minerals can be critical gauges of thermochemical conditions for diagenesis, yet their presence alone largely informs about the end point of a much more complex and interesting history. Starting from an initial state where unstable sedimentary particles react with pore waters, geochemical modelling enables an appreciation of the chemical evolution of these waters in the context of dissolution of original minerals and the precipitation of new ones.

To examine the phase relations in the Sheepbed mudstone, the measured composition of the mudstones and an estimated composition for the pore water are used. The Sheepbed lake water must have consisted of runoff from the surrounding terrain that had partially evaporated, thereby accumulating dissolved solids, but apparently not evaporated enough to form distinct evaporite beds. To estimate the concentrations of dissolved solids in the runoff, the first step was to dissolve one mole of the (basaltic) Erte Ale volcanic gas (Oppenheimer *et al.*, 2014), with an added 1% O_2 (Lu *et al.*, 2014) in 1 kg of water, then about 90% of the CO_2 was removed, to bring the partial pressure of CO_2 down to 0·1 MPa from 0·3 MPa. This is equivalent to equilibrating the runoff water with an atmospheric CO_2 partial pressure of 0·1 MPa. Separate calculations equilibrated to 0·05 MPa $P(CO_2)$, but the difference in the water composition is minimal, resulting in little difference in the computed amounts of carbonate minerals. Using program CHIM-XPT (Reed, 1998) with the BRGM Thermoddem data base (Blanc *et al.*, 2012), the liquid is reacted with a Mazatzal basalt (McSween *et al.*, 2006a,b), to obtain a solution with dissolved cations appropriate to weathering of a basaltic terrain, accompanied by smectites and other minerals. The Erte Ale gas is a reasonable example of gas from a basaltic volcano, wherein key features are a large CO_2 fraction and a molar ratio of SO_2 to HCl in the range of 10, which is typical of basaltic gases on Earth (Aiuppa, 2009).

The scheme outlined above provides a basic starting point for understanding waters and diagenesis on Mars in the Hesperian, where the raw ingredients to the hydrosphere had to have been condensed volcanic gases that reacted with basaltic crust. On Earth, it is known that diagenetic waters evolve through progressive partial equilibration of pore fluids with authigenic minerals formed by reaction of fluid with detrital grains (Palandri & Reed, 2001), and that concept was applied to the Sheepbed to examine constraints on its authigenic mineral assemblage. At the low temperatures of the model reactions, 25°C and 50°C, metastable smectites form in place of kinetically retarded stable micas, chlorite and amphiboles, which are suppressed from the calculation, although modest transition of smectite towards chlorite is suggested by some of the XRD data described above. Use of alternate thermochemical data base SOLTHERM-XPT (Reed & Palandri, 2015) and alternate starting waters yield different stable and metastable minerals such as the clinopyroxene acmite (aegirine), which is a recognized authigenic low-temperature mineral, for example, in the Green River Formation (e.g. Milton *et al.*, 1960). The computation of this mineral and others that occur unusually on Earth are a reminder that the choices made about the likely kinetics of authigenic mineral precipitation should be subject to scrutiny and revision as current knowledge of Martian minerals and geochemical processes increases.

The computation of the thermodynamic constraints on a reaction (Fig. 11) of known Martian basalt with a plausible early surface water provides an essential framework for beginning to understand the minerals and bulk composition of the Sheepbed mudstones and their relationship with the atmosphere and hydrosphere. The XRD data show that many primary basaltic minerals are present in the mudstone detrital mix, and that the bulk composition is not too different from basalt, implying that much of the primary reactant rock remains unreacted. Thus, the computed authigenic minerals (Fig. 11) are diluted in the mudstone to an unknown extent and it is not possible to tell from the XRD data whether minor computed authigenic minerals such as the carbonate and pyrite are present. A further complication is that the reaction rates of basaltic glass, olivine and plagioclase are likely to be relatively fast (Fig. 10), but also strongly pH-dependent. A model reaction such as that described here does not provide for differential reaction rates, and thus cannot capture

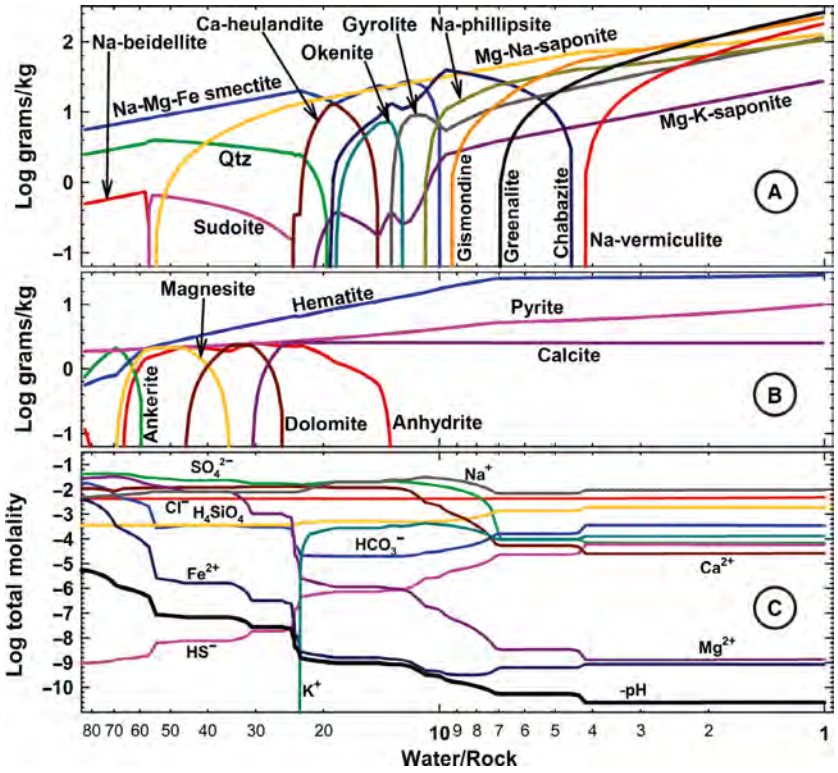

Fig. 11. Computed reaction of Mazatzal basalt with a hypothetical Sheepbed runoff/basin fluid described in the text. (A) and (B) Logarithm of mass of precipitated minerals per kilogram of initial aqueous phase versus water/rock ratio (mass ratio of titrated basalt to original aqueous phase mass). The logarithmic scale makes it difficult to compare masses visually, for example, at w/r 15, calcite mass is 2·5 g, Mg–Na-saponite is 20·6 g and Na–Mg–Fe smectite is 22·1 g. (C) Composition of the aqueous phase in total molality of component species (not individual species). The steps and plateaus in pH and dissolved component concentrations reflect buffering by the various mineral assemblages. At any given w/r, the graphs show the thermodynamically stable mineral assemblage and aqueous composition for the particular bulk composition specified by the w/r. The graph does not portray an amount of as yet unreacted detrital basalt material that is intermingled with the computed authigenic minerals; the unreacted material dilutes the authigenic assemblage to an extent dependent on a sedimentological conception of the reacting environment.

specifically the probable enhanced role of olivine and glass in driving cementation of the mudstone.

A calculation of an early diagenetic reaction at 25°C produces smectites and gypsum. The gypsum recrystallizes to anhydrite when the mixture is heated to 50°C, as shown in Fig. 11B. The reaction at 50°C (Fig. 11) represents diagenesis of a detrital mixture of eroded smectite and particulate Mazatzal basalt wherein the phase relationships can be examined as a basis for understanding the Sheepbed findings. The weathering runoff water described above was not evaporated before reacting it with the mixture of weathering products (gypsum and smectites, including saponite, Fig. 11A) because the water is saturated with gypsum at 25°C (or anhydrite at 50°C), and neither is observed as beds in the sediments. The computed gypsum formed in the mud matrix in early diagenesis could contribute to anhydrite veins upon burial and modest heating, as suggested by the anhydrite shown in Fig. 11B in the water/rock (w/r) range of 60 to 16, and further discussed below in the section on anhydrite veins.

The dominant (*ca* 60 to 30 wt%) diagenetic minerals are smectites (Na–Mg–Fe smectite, Mg–Na-saponite) throughout most of the computed range. Lesser amounts of zeolites and similar minerals (heulandite, okenite, gyrolite, gismondine phillipsite) precipitate at w/r less than *ca* 25, although smectites still dominate. Zeolites have not been identified in the Sheepbed sediments although they are common on Earth in diagenetic settings and hydrothermally altered rocks of similar composition, suggesting

that the relevant w/r reaction ratios for the Sheepbed are larger than 20, or that reaction of the Sheepbed detritus with its pore waters occurred at such a low temperature that slow kinetics of zeolite precipitation precluded their formation. Small amounts of carbonate minerals are also computed (mostly less than 6 wt%) reflecting the significant carbonate amounts in the pore fluid inherited from the atmosphere.

Hematite is a major repository of diagenetic iron in the computed reaction, reflecting the oxidation by sulphate of ferrous iron in the reactant basalt detritus, which contains 16·8% FeO. A fluid such as this one containing enough sulphate (Fig. 11C) to form anhydrite, as observed in the Sheepbed sediments, contains sufficient sulphate to oxidize ferrous iron, reducing sulphate to sulphide, which appears in pyrite (Fig. 11B), and ultimately depletes aqueous sulphate (w/r *ca* 7, Fig. 11C). If the inorganic oxidation kinetics of iron are slow, the ferrous iron may form silicates instead of hematite, such as the greenalite computed here at w/r 7.

The aqueous phase in the diagenetic reaction evolves from somewhat acidic pH to neutral to alkaline in steps controlled by mineral buffers (Fig. 11C). Overall, the diagenetic pore fluid changes from Ca–Mg–Na-sulphate to Na-chloride, but in the actual setting where it is known that substantial basaltic detrital grains remain, the reaction may have been arrested at w/r *ca* 25 – a composition in equilibrium with substantial smectite, minimal zeolites and modest amounts of carbonate and anhydrite.

The finding of smectites (including Mg–Na-saponite) at all w/r ratios is consistent with their occurrence in the Mars Science Laboratory (MSL) XRD patterns (Fig. 9). Their precipitation from a range of water rock interactions is expected because hydrous basalt on Earth generally forms smectites at low temperature.

Kinetics of clay mineral formation

The timing of clay mineral formation after deposition cannot be extracted from this type of calculation, but examination of clay mineral formation during weathering of modern volcanic rocks and volcaniclastic sediments on Earth can provide some guidance as to the amount of time required. For example, allophane and imogolite have been found in the B horizons of soils derived from 5000 to 10 000 year old ashes (Wada, 1989). The allophane apparently subsequently transforms into the clay mineral halloysite. Halloysite formation from volcanic ash occurred after about 10 000 years in Japan (Saigusa *et al.*, 1978), and after 15 000 years (New Zealand; Kirkman, 1975) to >30 000 years in ash beds from central Japan (Nagasawa, 1978). In the Sheepbed mudstone, the potential presence of allophone or Fe-enriched allophane is suggested by small-angle scattering in the XRD patterns (Fig. 9). Because allophane can form as a short-term intermediate before the formation of clays (Wada, 1989), it is plausible that the amorphous component of the Sheepbed mudstone consists of clay precursor phases such as allophane and imogolite, mixed intimately with nanophase iron compounds.

Thus, when examined from multiple perspectives, a plausible concept of clays in the Sheepbed member emerges where detrital clays were supplied to the lake basin from variably weathered upper crustal rocks (volcanic and sedimentary rocks, lithified ejecta blankets). Alteration of unstable grains (Fe-forsterite, glass, etc.) in contact with pore waters of the accumulating muds led to formation of amorphous precursor phases as well as secondary (diagenetic) clay minerals several thousands to tens of thousands of years after deposition. The likelihood that detrital clays were part of the original sediment that now forms the Sheepbed mudstone is essential to an understanding of the early diagenetic history of these rocks because it provides an experimentally understood mechanism to produce synaeresis cracks in muddy sediments (e.g. Burst, 1965).

DIAGENESIS

Various aspects of Sheepbed diagenesis have already been pondered in prior publications, one of them being the presumed diagenetic origin of clay minerals (McLennan *et al.*, 2014), an issue discussed in the preceding section of this paper. Other aspects explored were early diagenetic millimetre-scale nodules and so-called 'raised ridges' (Grotzinger *et al.*, 2014), described in considerable detail by Siebach *et al.* (2014) and Stack *et al.* (2014). A final aspect of Sheepbed diagenetic history is late diagenetic anhydrite-filled fractures that cross-cut nodules and raised ridges and have been attributed to burial-driven expulsion of overpressured fluids that led to hydraulic fracturing (Grotzinger *et al.*, 2014; Schieber, 2014).

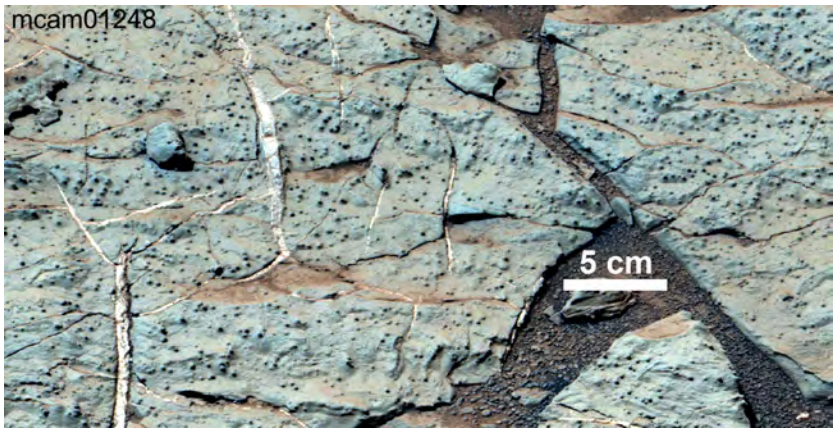

Fig. 12. View of a mudstone bed with abundant small nodules that are sculpted out by aeolian abrasion. The rock is criss-crossed by millimetre to centimetre wide late diagenetic fractures (Grotzinger *et al.*, 2014) that are filled with calcium sulphate (probably anhydrite; Vaniman *et al.*, 2014). Given that the rock surface is more or less flush with the anhydrite vein fills suggests that the mudstone is approximately of the same hardness as anhydrite. Images from a Mastcam Right mosaic acquired on Sol 298 (0298MR0012480180203696E01, 0298MR0012480230203701E0, 0298MR0012480240203702E01 and 0298MR0012480290203707E01).

Fig. 13. 'Raised ridges' in the Sheepbed mudstone at the John Klein locality. The 'ridges' are set in a matrix of soft greyish mudstone with millimetre-size nodules. In the upper left this nodule-bearing mudstone is still present and covers up the ridges, whereas in the centre and lower right of the image the 'ridges' have been exhumed by aeolian abrasion because, by virtue of their cement fill, they are harder than the mudstone matrix and therefore erosion resistant. Residual pockets of this nodule-bearing mudstone matrix can still be seen areas where the ridges form protected overhangs and corners. Images from a Mastcam Right mosaic acquired on Sol 153 (0153MR0008480050201277E01, 0153MR0008480060201278E01, 0153MR0008480150201287E01 and 0153MR0008480160201288E01).

Early diagenesis

The following paragraphs briefly summarize observations relating to early diagenesis and then focus on augmenting and expanding the catalogue of observed diagenetic features and on developing a more comprehensive understanding of the post-depositional history of these rocks.

Nodules and raised ridges

Nodules observed in the Sheepbed mudstone are millimetre-scale spherical and erosion-resistant features that have been categorized as 'solid nodules', 'hollow nodules' and 'filled nodules' (Stack *et al.*, 2014). These are dispersed through a more easily weathered matrix (Fig. 12) and give the rock a pustular appearance. Hollow nodules are systematically larger than solid nodules, and 'filled nodules' containing $CaSO_4$ appear to be related to late diagenetic hairline fractures that intercepted 'hollow nodules' and allowed their infill with $CaSO_4$ (Stack *et al.*, 2014).

The so-called 'raised ridges' are loose networks of spindle-shaped cracks that appear to be clustered in certain stratigraphic horizons

(Fig. 13). These ridges can be seen to cross-cut bedding, do not form polygonal networks and are infilled with multiple layers of isopachous cement that is more erosion resistant than the enclosing mudstone matrix (Siebach *et al.*, 2014). The cement, their discontinuous nature, as well as their generally subvertical orientation suggest that these are subaqueously formed synaeresis cracks, rather than desiccation cracks.

This study concurs with Stack *et al.* (2014) and Siebach *et al.* (2014) that nodules and raised ridges formed very early in diagenetic history in soft and water-rich sediments, although the necessary textural observations to determine the relative timing of features are not available. However, this study differs with regard to the underlying mechanisms and proposes a single basic process that drives the entire spectrum of observed diagenetic features (see discussion of diagenetic processes).

Diagenetic beds

Diagenetic beds are a newly described attribute of the Sheepbed mudstone. Although bedding features examined to this point can all be explained as the outcomes of various physical depositional processes, there are also beds that owe their appearance to vertical variations in erosion resistance, probably reflecting differences in the cementation (and thus erosion resistance) of some horizons. For example, Fig. 2B shows two erosion-resistant levels (yellow arrows) in Sheepbed unit 2 that are characterized by an abundance of small round nodules that are considered a result of early diagenetic cementation (Grotzinger *et al.*, 2014; Stack *et al.*, 2014). Within such horizons there is additional vertical variability of erosion resistance at the centimetre to decimetre-scale (Figs 6 and 7) suggesting that there was not merely cementation at the scale of millimetre-sized nodules and 'raised ridges' (Siebach *et al.*, 2014; Stack *et al.*, 2014), but also laterally pervasive cementation that affected entire horizons and gave rise to 'diagenetic' beds. The prominent layers that are visible in Fig. 3D and 3E are quite possibly lateral equivalents of the resistant interval shown in Fig. 6, and they may mark laterally extensive stratiform cementation. In the John Klein – Cumberland study area, there are multiple Mastcam images that show resistant layers that have been sculpted out by aeolian erosion (Fig. 2B), and there are also visible differences in the style of aeolian erosion between layers (Fig. 7) that probably relate to the level of matrix cementation in these beds.

Evidence for stratiform cementation can be seen at various scales in Mastcam mosaics and MAHLI images that have been collected from the Sheepbed mudstone. There are, for example, thin layers of hard float material that have 'hollow nodules' at the surface (Fig. 14A), but both the nodule rims and the rest of the surface appear to consist of the same material (possibly the same cement). Given that these float pieces are rather thin (probably only a few millimetres, Fig. 14A), they probably represent the thin but very well-cemented horizons of sedimentary rock that were left behind as overlying and underlying material was removed by aeolian abrasion. In addition, hard and presumably cemented surfaces typically show attached objects composed of hard material, such as nodules, and there are remnants of overlying softer material (uncemented or less well cemented) where wind erosion produced wind tails of soft material behind harder obstacles (Fig. 14B and D). The applicability of this interpretation was confirmed by abrasion experiments conducted in the laboratory (Howald & Schieber, 2009; Wilson *et al.*, 2011; Rossman *et al.*, 2012), where sand was moved by strong air currents over samples with layers of differing hardness (construction cement versus gypsum) and resulted in textures as seen in the Sheepbed member (Fig. 14C). Irregular erosion-resistant surfaces (Fig. 14E and F) and irregular features on top of hard (presumably cemented) surfaces may point to mechanical processes that disrupted cementing interfaces and may even have mobilized material from underneath and deposited on top of these cemented interfaces (Fig. 14H).

An example of a cemented bed overlying a softer and more poorly cemented interval is shown in Fig. 15, the location of the Cumberland drill hole. Two of the same layers already examined in Fig. 7 can be seen here, the layer with abundant raised ridges (layer Y) that is overlain by a harder layer with abundant nodules (layer Z). In Fig. 15, the step-up from layer Y to Z, as well as the intervening notch, suggest that layer Y is softer in nature when compared with layer Z. The bumps (nodules) at the surface of layer Z appear to be an integral part of the underlying rock matrix. They are in essence an ornamentation on the surface of a rock layer that has the same degree of erosion resistance as the nodules themselves, suggesting that cementation of nodules and matrix is of comparable

Fig. 14. Examples of stratiform cementation. (A) Fragment of hard layer with hollow nodules (arrows). Layer material and the 'nodules' appear to consist of the same material. MAHLI image 0159MH0000900000101728R00. (B) Area 1 shows hard surface with attached nodules that has been 'cleaned' by aeolian abrasion, and in area 2 there is softer material on this surface that forms wind tails behind nodules (yellow arrows, wind from the right) and also contains holes where nodules were plucked from the surface (black arrows). MAHLI image 0291MH0001970010103292C00. (C) Experimental specimen with gypsum above cement. Gypsum shows wind tails associated with slightly harder portions (same effect when small balls are suspended in gypsum). The underlying cement layer has small surface blemishes, created when the gypsum bed was placed on top, and these have not been modified by aeolian abrasion because of the greater hardness of the cement layer. (D) Another example of a hard surface with attached nodules and surficial ridges that has been 'cleaned off' on the left half of the image, and still is covered with soft material marked by wind tails on the right half of the image. MAHLI image 0171MH0002130010102259C00. (E) An irregular hard surface that has been cleaned off by aeolian erosion. Mastcam Right image 0177MR0009480010201984C00. (F) An experimental analogue to (E). Here, a layer of cement was given a wrinkled-irregular surface and then covered with gypsum. Aeolian abrasion removes the gypsum and leaves behind an irregular hard surface. (G) A hard layer (black arrows) with a bumpy surface texture is overlain by softer material (yellow arrows at base) with nodules. Wind tails behind nodules attest to the softness of the overlying material. MAHLI image 0292MH0002790000103423R00. (H) A hard surface that has been cleaned off by aeolian abrasion and carries on the surface irregular bumps and ridges of erosion-resistant material (also cleaned off). The ridge marked with yellow arrows looks like material might have oozed out of a crack onto the surface and then hardened. MAHLI image 0176MH0001450010102347C00. MAHLI, Mars Hand Lens Imager.

intensity. There is also no obvious difference in colour and texture between nodules and matrix, strongly suggesting that the cementing agent is the same. This inference is supported by ChemCam data, where in spite of numerous measurements no systematic differences between nodules and matrix were observed (McLennan *et al.*, 2014). The absence of wind tails on this surface suggests that any overlying softer materials have already been removed by aeolian abrasion.

Whereas the bumps (nodules) on the surface of Z are rounded (Fig. 15C), those on the surface of Y are elongated, asymmetrical and aligned (Fig. 15D). In close-up, the asymmetry is due to nodules that are 'clean' on one side and have a tapering 'tail' of softer material on the opposite side (Fig. 15E). They have previously been interpreted as wind tails due to aeolian abrasion (e.g. Farley *et al.*, 2014). In places, nodules were plucked out of the matrix during brushing with the dust removal tool (DRT), resulting in circular holes, a feature not observed in layer Z. Collectively these observations suggest that in layer Y, nodules that are probably the same composition as in layer Z, are suspended in a softer non-cemented matrix. This conclusion is re-enforced by close-up imaging from the Cumberland brush spot (DRT) where wind tails and the rock matrix are scratched by the steel bristles of the brush, whereas the nodules resist scratching (Fig. 15E).

Thus, within Sheepbed unit 2, harder and well-cemented layers are interspersed with softer layers that either lack cement or are more poorly cemented. Both harder and softer layers contain previously described diagenetic features, namely nodules (Stack *et al.*, 2014) and raised ridges (Siebach *et al.*, 2014).

Additional observations and thoughts on nodules and raised ridges

As pointed out above, the authors agree that these features are manifestations of early diagenesis as previously proposed by Grotzinger *et al.* (2014), Siebach *et al.* (2014) and Stack *et al.* (2014). However, some of the observations herein bring these features into a broader context of early diagenesis and a different interpretation of the underlying causes is suggested.

One issue in particular is the assumption by Siebach *et al.* (2014) that networks of 'raised ridges' pass laterally into mudstones with high concentrations of nodules. At first, such an assumption seems justified on the basis of Mastcam image mosaics (Siebach *et al.*, 2014; Stack *et al.*, 2014). However, once the existence of diagenetically enhanced layering is considered (Figs 6 and 7) an alternative viewpoint seems viable, where harder and softer (more and less cemented) layers are interspersed and where prominent ridge networks are the result of differential erosion (Fig. 7A). Supporting this assertion is the fact that the ridge-bearing layer (layer Y in Figs 7 and 15) is definitely softer than the overlying layer Z (Figs 7D, 7E, 15A and 15B), and that remnants of eroded layer Y with nodules and wind tails (soft matrix) are visible in various mosaics (Fig. 16). Likewise, the

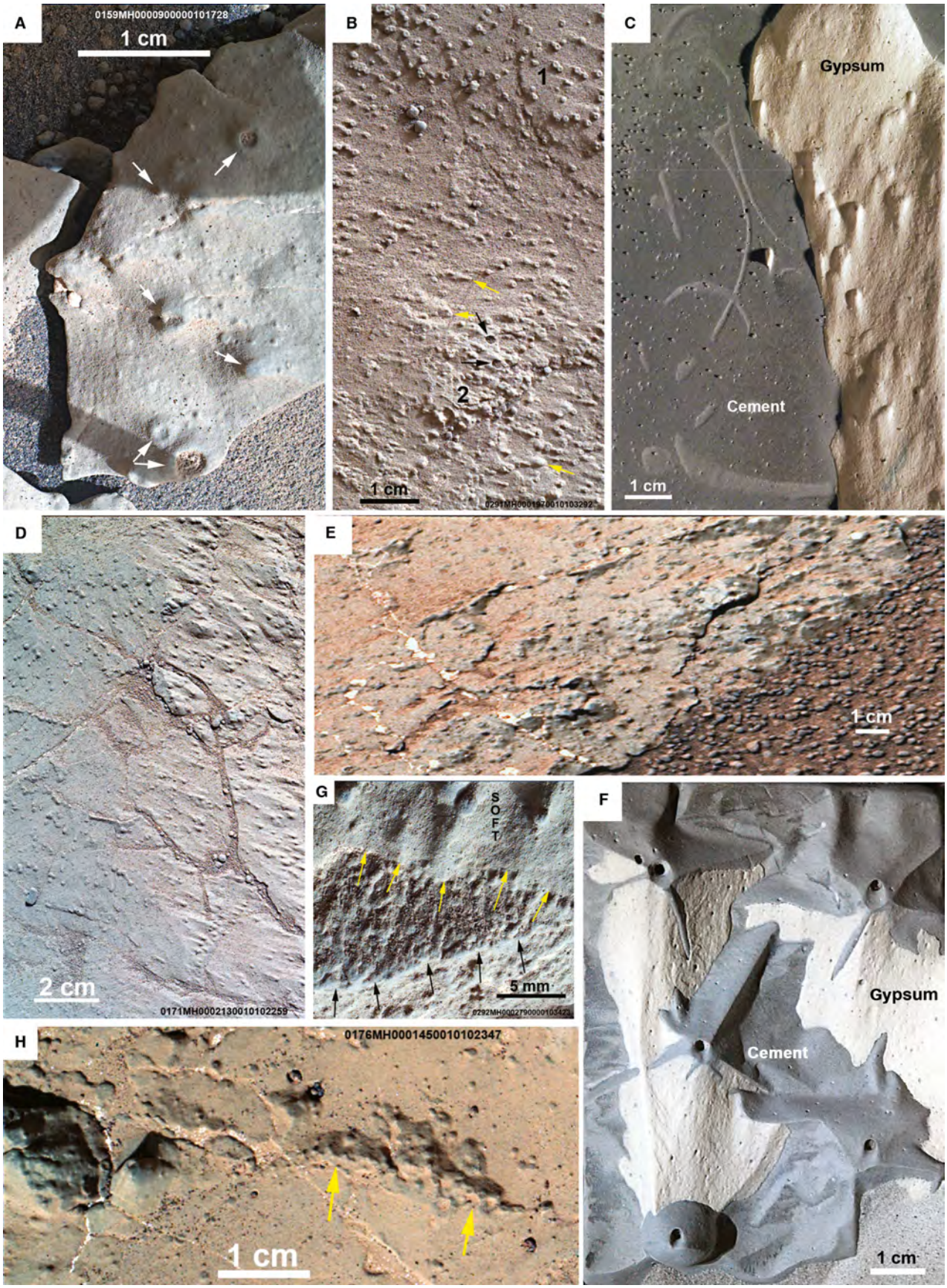

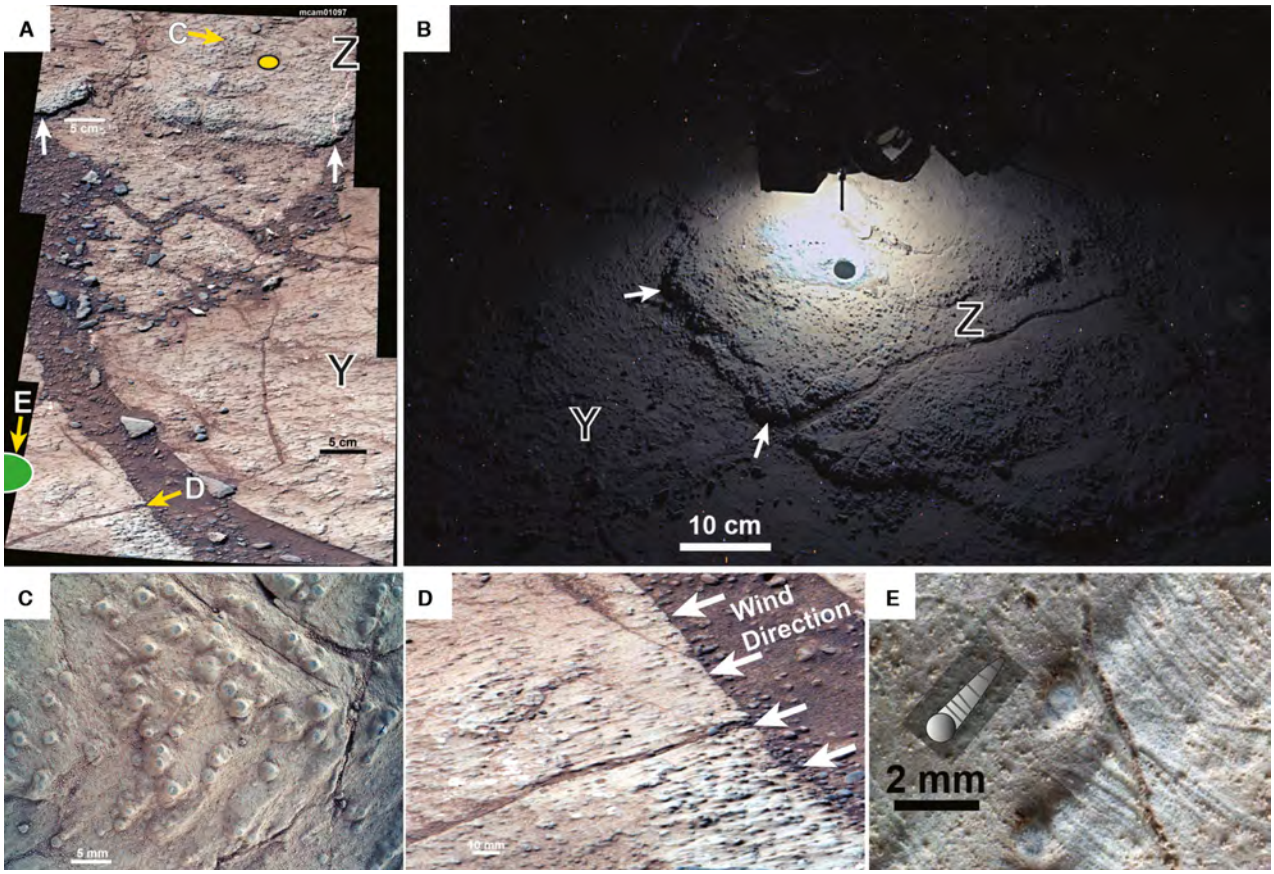

Fig. 15. (A) A Mastcam Right mosaic acquired on Sol 227 (images 0227MR0010970000202900E01, 0227MR0010970030202903E01 and 0227MR0010970060202906E01) that shows a closer view of the Cumberland drill site and its vicinity. White arrows point to a boundary between two layers, presumed to be layers Y and Z as marked in Fig. 7A. Layer Z appears more erosion resistant and differs in surface texture from layer Y. Yellow oval marks Cumberland drill hole, green oval marks Cumberland brush spot (DRT). Yellow arrows and letters 'C', 'D' and 'E' point out detail features below. (B) The rover never sleeps. Night imaging of Cumberland drill hole with MAHLI (using LED illumination), image taken by Mastcam Left (0292ML0012290010106381E01). The image brings out the contrast between layers Y and Z (contact marked by arrows). (C) Closer view of the surface of layer Z. Shows the rounded features that have been described as nodules in prior publications (Grotzinger *et al.*, 2014; Stack *et al.*, 2014). MAHLI image 0276MH0002650000103019R00. (D) Closer view of the surface of layer Y. Round features (presumed to be nodules) consistently have an elongate tail to the left. At the edge of the slab wind erosion has worn down the layer by 10 to 20 mm. Mastcam Right image 0227MR0010970060202906E01. (E) An even closer look at the surface of layer Y at the Cumberland DRT. The round nodules show no damage (scratching) from the DRT, but the wind shadow tails have been scratched by the DRT steel bristles (Fig. 1E). The inset line drawing emphasizes the observed features, scratched wind tail and scratch resistant nodule. MAHLI image 0295MH0002760000103652R00. MAHLI, Mars Hand Lens Imager.

relationship observed in Fig. 13, where nodule-bearing soft mudstone covers the ridges in the upper left and where 'raised ridges' have been exhumed by aeolian abrasion in the lower right and still show residual pockets of nodule-bearing soft mudstone, also suggests that nodule-rich mudstones and ridge-rich areas do not pass laterally into one another (as suggested by Siebach *et al.*, 2014). Instead, the phenomenon of 'clustered' distribution of ridges (Siebach *et al.*, 2014) can be explained as a result of variably deep aeolian erosion into a layer that consists of soft nodule-bearing mudstone with cross-cutting ridges (Fig. 17).

Although the cemented cracks that have been described as 'raised ridges' are prominently associated with soft and easily eroded beds (Figs 13 and 16), they also occur within the ledge-forming beds with enhanced matrix cementation. For example, in Fig. 6 multiple oblique and erosion-resistant features are seen within these harder and nodule-rich beds, and these are most likely

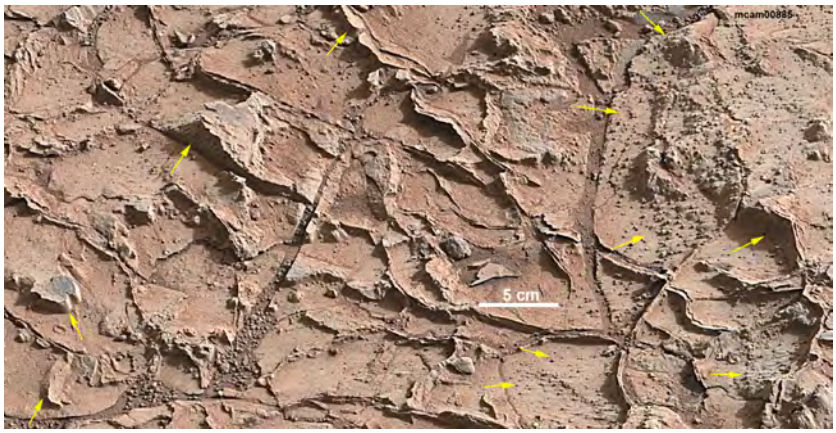

Fig. 16. Close-up of raised ridge horizon (layer Y) at John Klein drill location. Shows that erosion-resistant ridges protected matrix material in various places (arrows) from complete erosion. This matrix contains nodules and there are wind tails associated with nodules, suggesting a softer material, similar to elsewhere in layer Y (for example, Fig. 15D). Towards the upper right corner the ridges appear to get 'buried' under more resistant material with nodules, probably the transition to the overlying layer Z (Figs 13 and 15). Portion of a Mastcam Right mosaic acquired on Sol 164 (images 0164MR0008850020201591E01, 0164MR0008850050201594E01, 0164MR0008850 060201595E01 and 0164MR0008850070201596E01.)

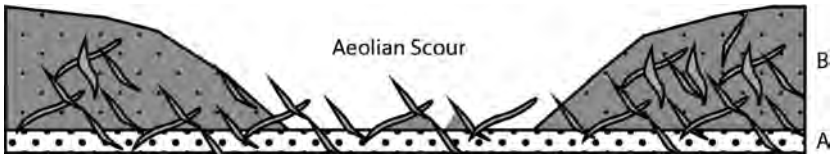

Fig. 17. Model for the formation of clusters of raised ridges: A = basal planar layer as indicated in Fig. 7 (presumed to be sandy and erosion resistant); B = layer of soft mudstone that contains nodules (dots) and cemented synaeresis cracks. As aeolian erosion locally removed the mudstone the ridges rose above the basal resistant layer and formed a cluster of raised ridges with pockets of mudstone still preserved in protected spots. Fig. 13 is representative of the left two-thirds of this diagram.

'raised ridge' equivalents. That this interpretation has merit can be seen in Fig. 18, where blocks of well-cemented layers show how these ridges can become 'hidden' or 'buried' in nodule-rich and more resistant layers. Figure 18, a MAHLI image from Sol 158, confirms that raised ridges as well as nodules are associated with the more resistant (matrix-cemented) ledge-forming layers that are shown for example in Fig. 6. In summary, nodules and ridges are intimately associated in the same mudstone beds, and these beds experienced variable degrees of diffuse diagenetic cementation (matrix cement). If this cementation was intense, resistant beds formed that create ledges in outcrop (Figs 2 and 3) and, if it was weak, recessive beds formed that because of removal of the soft matrix would show exposed raised rides in suitable locations (Figs 7 and 16).

Although millimetre-size diagenetic nodules are common throughout the Sheepbed unit 2 mudstone interval, it is a subcategory of these, the so-called 'hollow' nodules, that has generated a large amount of speculation about their origin (Stack *et al.*, 2014). Hollow nodules are those whose interiors are exposed in the form of a central void that is surrounded by a raised rim, such as seen in Fig. 14A. Competing hypotheses for their origin (Stack *et al.*, 2014) are: (i) that they may represent dissolution of an interior early mineralization phase; or (ii) that they were caused by gas bubbles within the sediment and that nodules then grew around the gas bubbles.

Although no detailed textural data are available to really settle this question one way or the other, there are some observations from gas bubbles in sediments on Earth that may provide some guidance. For example, a survey of the literature on gas bubbles in modern sediments (Förstner *et al.*, 1968; Abegg & Anderson, 1997; Anderson *et al.*, 1998) shows that there is a

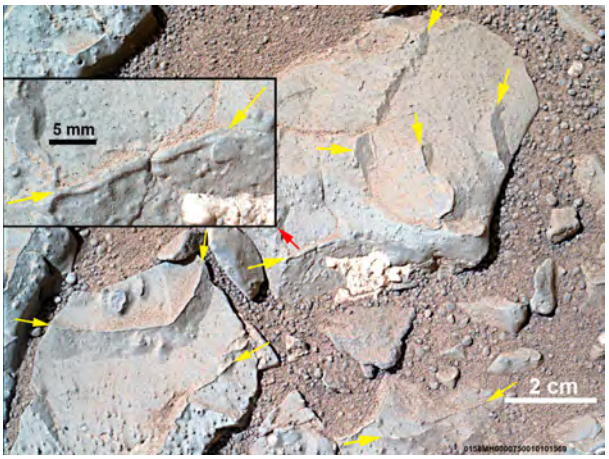

Fig. 18. Blocks of erosion-resistant nodule-bearing mudstone. Linear features marked with yellow arrows are interpreted as 'raised ridges' that are buried in a well-cemented matrix. Inset shows close-up of one of these ridges (red arrow). The ridge appears to have symmetrical cementation with harder margins and a softer interior, just as described from raised ridges in softer strata. The material that fills the 'ridge' does not appear to be significantly different from the surrounding matrix and implies that the cementing agent in the fracture and the surrounding matrix is probably the same. MAHLI image 0158MH0000750010101569C00. MAHLI, Mars Hand Lens Imager.

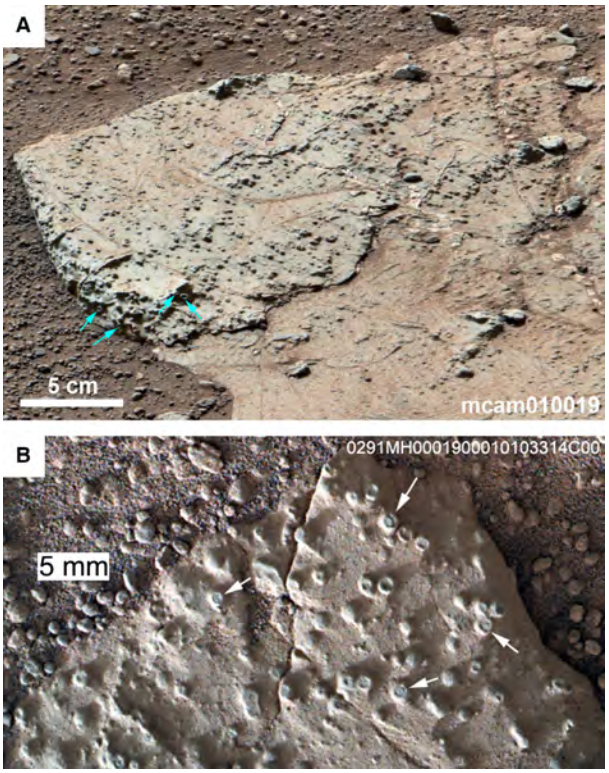

Fig. 19. (A) Weathering resistant bed with abundant solid as well as hollow nodules. Arrows point to hollow nodules whose openings point sideways, possibly nodules that were cored with an earlier and more soluble (or softer) material that was removed by dissolution or abrasion once the protective outer shell of the nodule was breached. Portion of Mastcam Right mosaic acquired on Sol 192 (images 0192MR00 10190170202632E01 and 0192MR0010190180202633 E01). (B) A resistant slab of sediment covered with 'hollow nodules'. Many of these, however, contain a soft greenish fill (arrows) that is at various stages of being removed, probably by aeolian erosion that selectively removes the soft fills. MAHLI image 0291MH0001900010103314C00. MAHLI, Mars Hand Lens Imager.

considerable range in sizes and shapes of bubbles, and that bubbles in quite a few instances are far from spherical (Anderson *et al.*, 1998; Boudreau *et al.*, 2005). In particular, bubbles in sandy (non-cohesive) sediments have a tendency to be rounded, and those in cohesive sediments are more commonly oblate with irregular outlines (Boudreau *et al.*, 2005).

Because the presumed Sheepbed gas bubbles would have formed in a fine-grained sediment that most likely acted cohesively, and given that the hollow nodules are generally rounded and circular in outline (Stack *et al.*, 2014), one wonders whether explaining them as gas bubble phenomena is actually warranted. The spherical nature of solid as well as of hollow nodules suggests that a diffusion-driven reaction, operating in a medium with considerable open pore space (a mud prior to significant compaction), might be a better choice (Coleman & Raiswell, 1993; Sefton-Nash & Catling, 2008; Chan *et al.*, 2012; Yoshida *et al.*, 2015); this is discussed in the following section on diagenetic processes. Because gas bubbles move upward through the sediment and burst once they reach the surface, hollow nodules at the surface of beds, such as in Fig. 14A, do at first seem consistent with a bubble origin. However, a closer examination of the many images also reveals places where hollow nodules occur on surfaces that cut across bedding and have hollow bubbles that point sideways (Fig. 19A). This geometric relationship suggests that either a hollow form was sliced open in that orientation, or that something originally filled the hollow and later was dissolved or removed by aeolian abrasion. As regards the latter possibility, there are in places 'hollow nodules' that actually seem to have a soft interior fill that has not been completely removed by aeolian erosion (Fig. 19B), supporting the

idea that the 'hollow nodules' may not have been initially hollow.

The so-called 'raised ridges' (Fig. 16) have a number of features, such as variable length, random orientation, spindle-shaped terminations and the absence of polygonal networks, that suggest that they may have originated as synaeresis cracks. The latter are sedimentary structures that result from shrinkage of water-rich muds in the absence of desiccation (Pettijohn & Potter, 1964; Plummer & Gostin, 1981). Siebach *et al.* (2014) discuss the various possibilities for synaeresis crack formation, including the possibility that they may be due to fabric collapse in flocculated clays (e.g. Burst, 1965), or because gas development, associated with formation of hollow nodules, led to fracture formation in the water-rich and cohesive sediment. However, whereas crack formation due to clay fabric collapse (induced by salinity change) has been verified by experimental work (Burst, 1965; Plummer & Gostin, 1981), crack formation by gas bubble expansion seems unlikely. The latter mechanism was tested here in laboratory experiments, and whereas the mud did indeed fracture in response to gas injection, the gas immediately escaped upward and led to a collapse of the short-lived fracture. Published experimental work on gas fracturing of muds (Frey *et al.*, 2009) confirms this observation. Because the synaeresis cracks in the Sheepbed mudstone appear to be filled with isopachous cement (Siebach *et al.*, 2014), they must have remained open for an extended time period to allow cementation, a condition not supported by a gas-fracturing mechanism. The analysis here of the nature of the original sediment suggests that there was an initial detrital clay component, and thus a mechanism by which flocculated clays shrink due to salinity-induced fabric collapse (e.g. Burst, 1965) seems considerably more plausible. As will be shown below, progressive chemical interaction between detrital minerals and pore waters may actually have generated the needed shift in salinity. Alternatively, initial clay deposition was probably accompanied by fresh river waters, and post-depositional salinity increase due to evaporation could also have caused formation of synaeresis cracks.

In addition to the role played by salinity, it has been proposed that synaeresis crack formation in some examples of terrestrial mudstones was triggered by earthquakes (Pratt, 1998), and that meteorite impacts might be capable of inducing seismic shocks to the same effect (Simms, 2007). Given the common occurrence of large impact craters, including Gale, during the Noachian time period (e.g. Robbins *et al.*, 2013), impact-induced seismicity may also have played a role in synaeresis crack formation at the time of Sheepbed deposition.

The cement mystery

Freshly deposited muds on Earth typically have porosities in the 70 to 90 volume % range (Schieber, 2011) and, in the case of early diagenetic cementation, much of that space can become partially or entirely filled with cement. It is therefore puzzling that in the Sheepbed mudstone, with ample evidence of early diagenetic cementation, no clear candidate for this cement has appeared in XRD analyses of these rocks (Vaniman *et al.*, 2014). Summing of the most plausible cements from the XRD analyses (hematite, magnetite and akaganéite) at John Klein and Cumberland, yields 5 to 7 weight % of potential cement minerals. This amount of cement is difficult to reconcile with the amount needed to make these rocks as solid as they appear in outcrop. The only other components that are sufficiently abundant by order of magnitude are clay minerals and amorphous components.

A model for early diagenesis

The majority of chemical data with high spatial resolution were acquired with the ChemCam instrument, using laser-induced breakdown spectroscopy (LIBS). ChemCam has very good detection for alkali and alkali earth elements, but is less sensitive for other elements (Wiens & Maurice, 2015). Also, due to the limited number of calibration targets (eight) on the rover and the highly diverse nature of the Gale Crater sedimentary rocks, accuracy is limited. Yet, even with these limitations, the compositional data from LIBS spectra are very instructive with regard to chemical differences (or lack thereof) between diagenetic features in Sheepbed exposures (Nachon *et al.*, 2014; Mangold *et al.*, 2015). As is apparent from the images in this paper, nodules, raised ridges and the matrix surrounding them do not show significant difference in colour and fine scale (sub-millimetre) texture (Figs 14A, 14D, 14H and 18), and within the limits of the rover's analytical capabilities they also do not show much contrast in chemical composition (Grotzinger *et al.*, 2014; McLennan *et al.*, 2014; Siebach *et al.*, 2014; Stack *et al.*, 2014). In combination, these observations permit the assumption that all

of the above-described early diagenetic features have a common cementing agent and that early diagenesis may have been dominated by a single chemical reaction.

Assuming, as discussed above, that the original Sheepbed muds consisted of variably weathered and recycled materials of basaltic provenance, they probably consisted partially of the weathering products of glass, olivine and feldspars, still retaining reactive material. After deposition, weathering (or alteration) continued pervasively *in situ* but with local centres of enhanced activity from differential kinetics, for example, variation in Fa/Fo in olivine. Stack *et al.* (2014) noted that the solid nodules are statistically significantly smaller than are the hollow nodules. The close spatial association and essentially identical appearance (colour, surface texture) of nodules and hollow nodules suggest that they may be the product of a reaction continuum where the same process, with slightly different parameters, can account for both features. All nodule growth requires chemical disequilibrium as the driver (Raiswell & Fisher, 2000), and in the case of the Sheepbed nodules the most plausible reaction might be the alteration of forsterite or basaltic glass. Both of these reactions would be kinetically feasible (Fig. 10), especially at the pH that prevails at the extent of reaction most relevant during sediment burial and diagenesis (Fig. 11). It is important to note that in Fig. 11 the thermodynamic equilibria pertain to the whole-rock composition. There are, however, two qualifying considerations. Firstly, as pointed out above, due to kinetic controls not all components of the reactant rock will be equally susceptible to alteration. Secondly, it is unlikely that the whole rock reacts homogeneously. It is likely that local centres of reaction occur around more reactive grains (for example, already partly reacted during transport or of subtly different composition) where the local control on pH might accelerate the process further. A corollary of this argument is that the amounts of diagenetic minerals shown for the whole-rock reaction (Fig. 11) may be applicable only to a localized environment of enhanced extent of reaction and not necessarily detectable in the bulk compositions measured by Chemin.

Heterogeneous diagenesis is the mechanism for the formation of nodules and concretions. Below is one example of a simplistic but plausible set of reactions of the kinetically favoured breakdown of olivine. A similar but more complex equivalent scheme could be written for the reaction of basaltic glass. Separating alteration of fayalite and forsterite (Schulte *et al.*, 2006) gives, for example, the following set of equations:

$$Fe_2SiO_4 + 5Mg_2SiO_4 + 9H_2O \rightarrow 3Mg_3Si_2O_5(OH)_4 + Mg(OH)_2 + 2Fe(OH)_2 \quad \text{(Eq. 1)}$$

$$Mg(OH)_2 \rightarrow Mg^{2+} + 2OH^- \quad \text{(Eq. 2)}$$

$$3Fe(OH)_2 \rightarrow Fe_3O_4 + 2H_2O + H_2 \quad \text{(Eq. 3)}$$

A reaction of this type was also considered by McLennan *et al.* (2014) to be a possible driver for clay formation during Sheepbed diagenesis, although chemical modelling suggests that multiple reactions may have contributed to diagenetic clay formation (Fig. 11), and that the bulk of diagenetic clays probably were generated thousands of years after deposition of a given bed. How deep might these sediments have been buried before the onset of diagenetic clay mineral formation? Although there are no data on Martian sedimentation rates, and given that comparisons with Earth analogues are tenuous because Martian gravity is 0·375 that of Earth, sedimentation rates from Earth examples are still instructive with regard to the likely magnitude of burial. On Earth, net sedimentation rates in alluvial fan – lacustrine settings can be around 1 m per 1000 years or more (Einsele, 2000; Smith *et al.*, 2010), and it is therefore plausible to assume that the bulk of the diagenetic clays in the Sheepbed mudstone formed after the sediments had already been buried by several metres.

The degree to which the above reactions might have contributed to diagenetic smectite formation in the presence of Al from dissolving volcanic glass (McLennan *et al.*, 2014) remains uncertain (Fig. 11), but they do produce the hydroxyl ions that could drive the modelled reactions in Fig. 20. Figure 20 takes its cues from a model developed by Coleman & Raiswell (1995) and Coleman (1993) to explain hollow terrestrial concretions by centrifugal (not centripetal) diffusion. Stack *et al.* (2014) stated that APXS analyses showed that nodule-rich areas correlate with the presence of iron, implying that solid and hollow nodules may contain a higher concentration of an iron-bearing mineral than the host mudstone. It seems plausible therefore that centrifugal diffusion of hydroxyl ions (reaction 2) was the most likely driver. What actual reactions were involved in the

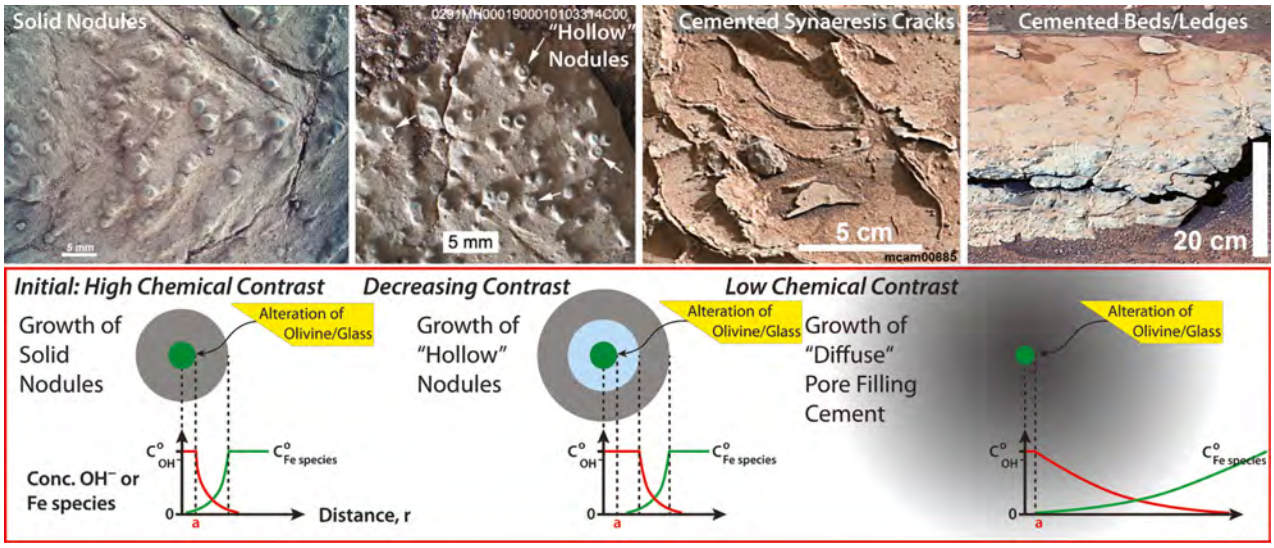

Fig. 20. Envisioned progression (from left to right) of early diagenetic features as olivine/glass alteration reaction dissipates through the pore space. The top row shows representative images of the various diagenetic features that form as a consequence of this process. The bottom row shows a model of centrifugal and counter diffusion of two reactive species at various levels of chemical contrast with the surrounding pore waters, how the saturation index may be exceeded at the centre (solid nodules) or at some distance (hollow nodule, cement shell) from the reacting grain, and how at lowest contrast cementation of synaeresis cracks (raised ridges) and the matrix (cemented ledges) occurs. Based on a two-dimensional model developed by Helfferich & Katchalsky (1970) which was developed into a 3D model by Raiswell *et al.* (1993). Images from left to right: MAHLI image 0276MH0002650000103019R00; MAHLI image 0291MH0001900010103314C00; Mastcam Right image 0164MR0008850060201595E01; Mastcam Left image 0298ML0012440030106396E01. MAHLI, Mars Hand Lens Imager.

diagenetic transformations of the Sheepbed muds remains unknown in the absence of insight from optical and electron-beam petrography, but the above outlined mechanism is chemically plausible and provides a rationale to understand a wide range of features within a coherent conceptual framework (Fig. 20).

The inherent mechanics of centrifugal diffusion, as illustrated in Fig. 20, can explain both the solid and hollow concretions as well as their sizes. In centrifugal diffusion, the size of a concretion is controlled both by the rate of reaction at the centre of the forming nodule and by the concentration of the species with which it is reacting in the surrounding pore water. If the external reactant concentration is lower, then the centrifugal diffusing front must travel further before it will exceed the solubility constant of the precipitate. Qualitatively, nodules growing in a more concentrated pore water reactant environment will grow to completion and are solid. In a less concentrated reactant environment, however, the reaction products diffuse further away before they precipitate, forming a cemented shell with an uncemented interior. At the time of formation the interior is likely to be filled with water and uncompacted sediment, and one could argue that with billions of years available for further diffusion, the interior may modestly solidify over time. The soft fills seen in Fig. 19B may represent this stage. A possible Earth analogue, hollow spheres of magnetite, has been reported from crater-lake (maar) deposits in Africa (Cornen *et al.*, 1992).

Extending the same model further (Fig. 20), following the period of relatively rapid alteration of detrital olivine/glass, the process continues but with insufficient chemical contrast to produce spheroidal nodules. Instead, this is when the matrix cement is precipitated variably throughout the system and is also available to fill available cavities, such as synaeresis cracks and pore spaces.

As indicated above, synaeresis cracks can be generated in experiments where flocculated clays are subjected to a change in salinity (e.g. Burst, 1965; Plummer & Gostin, 1981). In the Sheepbed mudstone, relatively small amounts of chemical sedimentation (McLennan *et al.*, 2014) and the absence of evidence that lake waters were at times supersaturated with evaporite minerals were taken as an indication that deposition occurred in

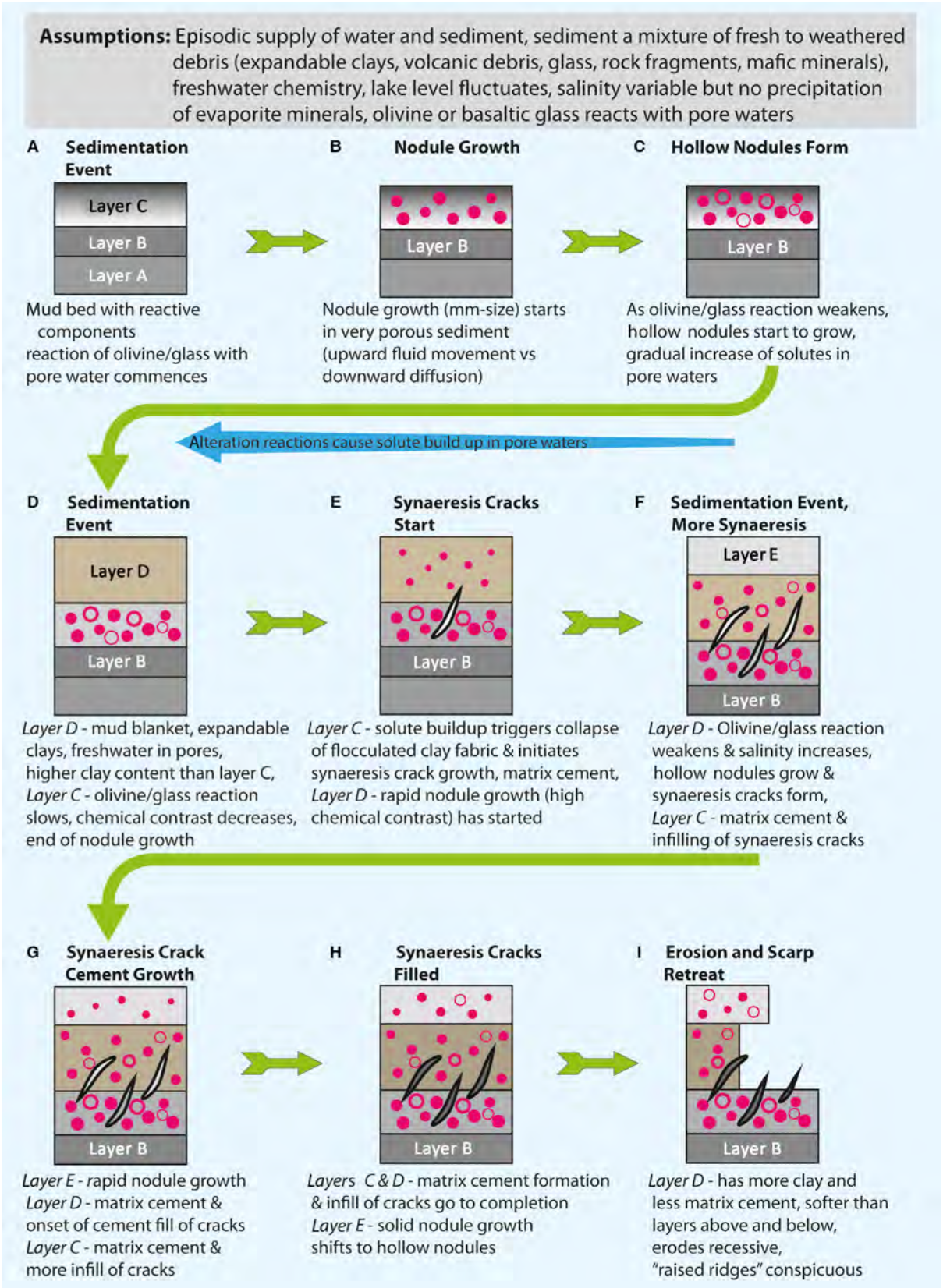

Fig. 21. A summary of how the interplay of sedimentation pulses, diagenetic processes and subsequent erosion produced the features observed in outcrop at Yellowknife Bay.

waters of low salinity (Grotzinger *et al.*, 2014). It is worth noting at this juncture that seawater, for example, is definitely saline, yet undersaturated with evaporite minerals, and thus it is plausible that the lake waters were intermittently somewhat saline as well and may have caused fabric collapse and synaeresis in the freshly deposited mud. The reaction graph in Fig. 11C suggests comparatively small initial build-up of dissolved species owing to diagenetic reactions, and makes a salinity increase in the lake waters a more likely driver for synaeresis.

This model (Fig. 20) implies that infilling of synaeresis cracks overlaps in time with matrix cementation, and it may explain a puzzling feature of the Sheepbed raised ridges – their apparent lack of compactional deformation. Cracks formed in water-rich sediments on Earth frequently show substantial deformation by means of ptygmatic folding (Ulmer-Scholle *et al.*, 2015) or telescoping if cemented (Pratt, 1998), yet the presumed synaeresis cracks of the Sheepbed mudstone show comparatively smooth curvature when exposed by aeolian erosion (Figs 13 and 16). One can speculate that early cementation stabilized the sediment sufficiently to minimize the distorting effects of compaction.

The evident vertical variability of cementation in Sheepbed unit 2 strata (Fig. 6) implies (from an Earth perspective) that sedimentation rates varied and that there were prolonged pauses in sedimentation (e.g. Lazar *et al.*, 2015). Cements occupied a larger portion of the available pore space at times of slow sedimentation, and as sedimentation rates increased the cement fraction of the sediment decreased (Taylor & Macquaker, 2000). The observation of lower clay contents at Cumberland (Vaniman *et al.*, 2014) could be a manifestation of 'cement dilution' in that location. Figure 21 summarizes in an idealized way what sequence of events and processes could have produced the features observed in outcrop at Yellowknife Bay.

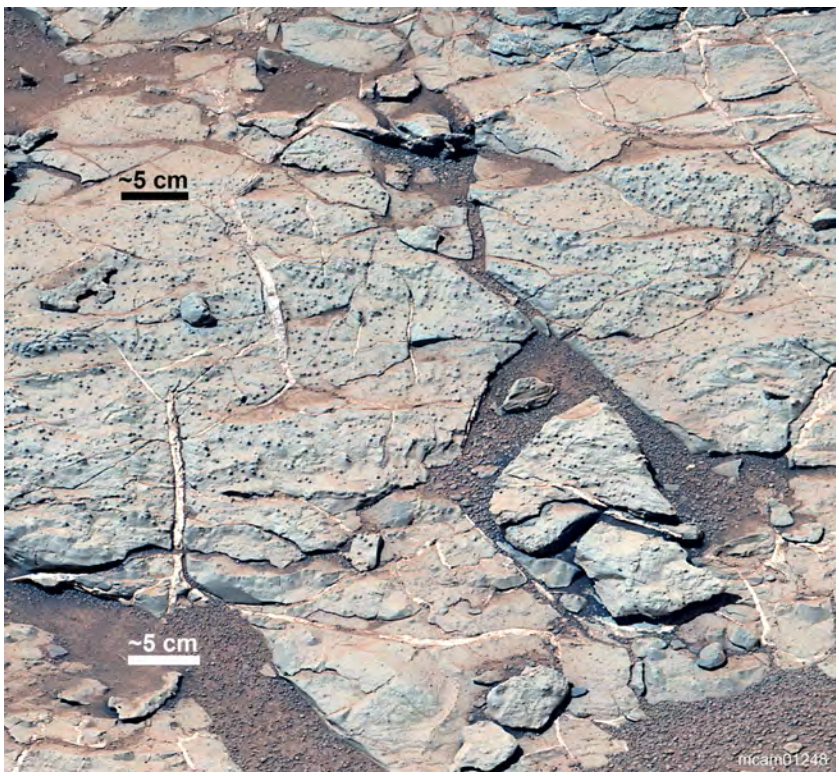

Fig. 22. Oblique view of the Sheepbed outcrop with a nodule-rich bed in the middle-ground. Parallel-sided anhydrite-filled subvertical fractures (up to 1 cm wide) are prominent. These 'straight veins' represent one of the common styles of vein formation in the Yellowknife Bay area (Fig. 2). Strike of veins appears to be random, consistent with a hydrostatic state of stress in the plane of bedding during their formation. The veins weather level with their mudstone host indicating that the two have approximately the same resistance to aeolian abrasion. Portion of a Mastcam Right image from Sol 298 (images 0298MR0012480180203696E01, 0298MR0012480230203701E01, 0298MR00124802402 03702E01 and 0298MR0012480290203707E01).

Late diagenesis

In addition to the diagenetic features discussed above, the sediments of Yellowknife Bay contain pervasive networks of calcium sulphate (most likely to be anhydrite) filled fractures that formed later in diagenesis and cut across nodules, raised ridges and cemented beds (Grotzinger *et al.*, 2014; Siebach *et al.*, 2014; Stack *et al.*, 2014). These features are described and discussed below.

Straight veins

The strata exposed in Yellowknife Bay (Fig. 2) contain prominent fractures with a white infill that most likely consists of anhydrite (Grotzinger *et al.*, 2014; Nachon *et al.*, 2014). Fractures with this type of infill are not only observed in Yellowknife Bay but continue upsection through Gale Crater strata explored so far (e.g. Kronyak *et al.*, 2015a; Newsom *et al.*, 2016). A good example of these fracture fills (designated here as 'straight veins') is shown in Fig. 22.

Hairline fractures with white infill have been intercepted by the rover drill (Fig. 23B) and the XRD analysis of the corresponding host rock reveals 2·6% anhydrite (Vaniman *et al.*, 2014). Judging from Mastcam mosaics, these fractures show a wide range of orientations, and they range in width from less than a millimetre (hairline fracture, Fig. 23A) to more than a centimetre (e.g. Kronyak *et al.*, 2015b). These fractures show an overall subvertical orientation in outcrop, and their strikes when viewed on bedding, appear random.

X-ray diffraction analyses of the bulk rock show the presence of anhydrite, without evidence for gypsum (Vaniman *et al.*, 2014). The atmosphere of Mars is cold and contains very little water vapour. Although the relative humidity can approach 100% at night, the relative humidity during most of the Martian day is very low (<1%), and re-hydration of anhydrite is unlikely in that setting (Robertson & Bish, 2013). Another argument against pre-existing gypsum (and subsequent transformation to anhydrite) is that the conversion of anhydrite ($CaSO_4$) to gypsum ($CaSO_4{\cdot}2H_2O$) involves a 62% volume increase. The associated swelling causes spallation textures that are quite evident on Earth, but similar features have not been observed in any outcrops with exposed $CaSO_4$-filled veins at Yellowknife Bay. A small bassanite ($CaSO_4{\cdot}0.5H_2O$) component may occur with anhydrite (Vaniman *et al.*, 2014) and is plausibly explained by partial hydration of anhydrite

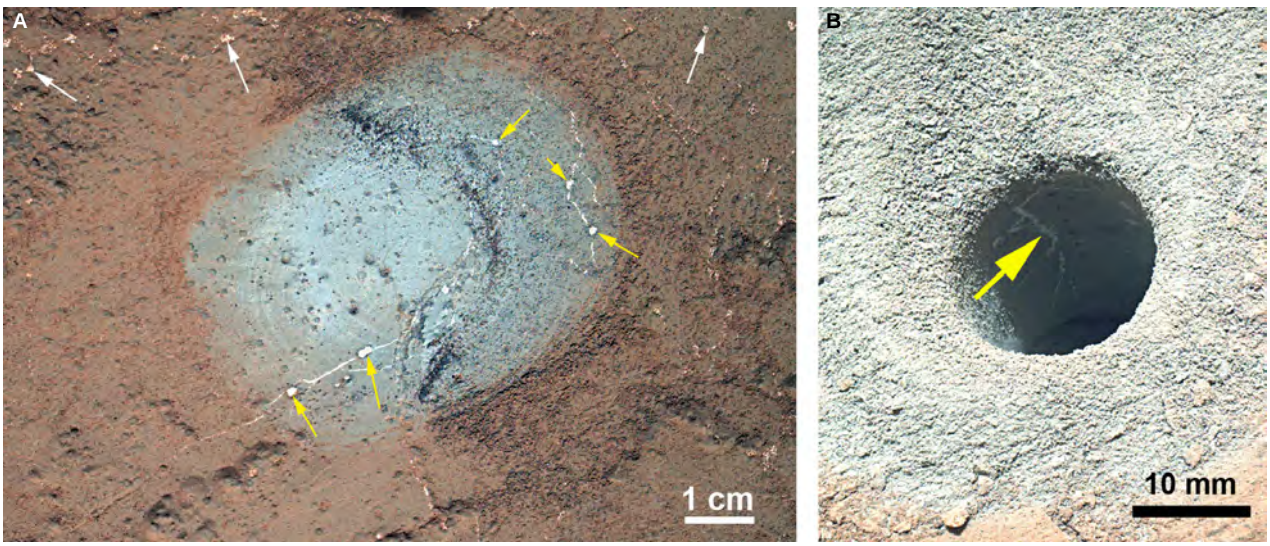

Fig. 23. (A) An area brushed with the DRT (Fig. 1) at the end of the rover arm. Note the colour difference between brushed and un-brushed surface. Rounded bodies of likely anhydrite occur across the surface and are comparatively easy to see (white arrows). The dust obscures the fact that these are connected to anhydrite-filled fractures, but that relationship is readily observed in brushed areas (yellow arrows). The anhydrite lumps are irregular in shape and size. MAHLI image 0173MH0001900010102313C00. (B) MAHLI image of the interior of the John Klein drill hole, showing the contrast between the unoxidized rock on the interior and the brownish oxidized coating at the surface. The yellow arrow points to an anhydrite vein that is oriented subvertical and has subhorizontal offshoots. MAHLI image 0270MH0002520000102916R00. MAHLI, Mars Hand Lens Imager.

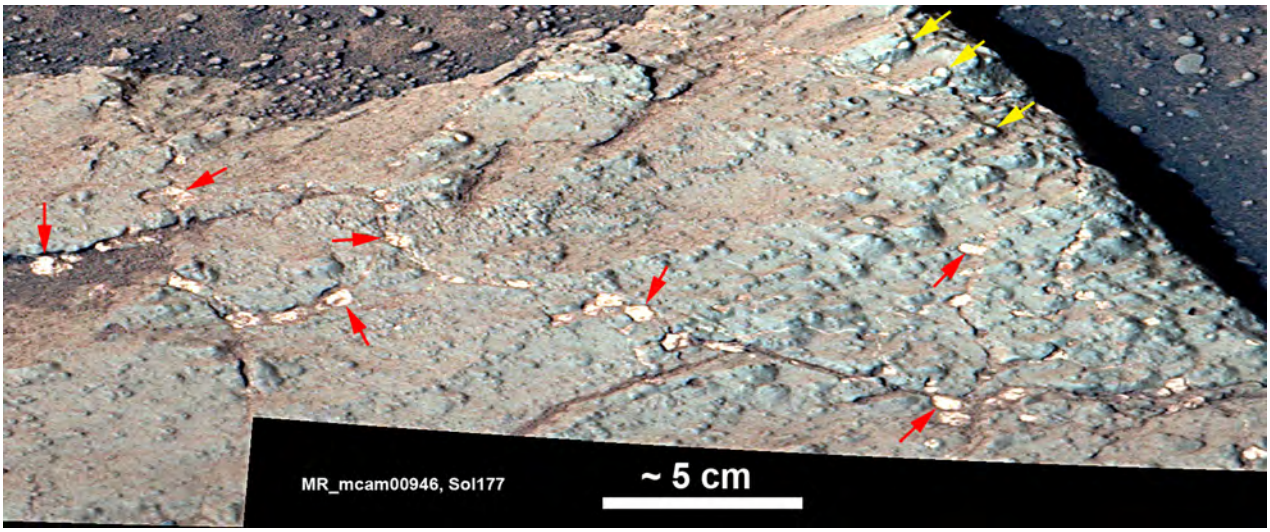

Fig. 24. Bedding plane with anhydrite veins that show larger irregular-rounded anhydrite masses (red arrows) that form within or alongside veins. This type of vein formation, described as 'knobbly veins', appears distinct from the 'straight veins' shown in Fig. 22. Yellow arrows point to filled cement shells for size comparison. Mastcam Right image 0177MR0094600102019 80C00.

where exposed to the present-day Martian atmosphere. Although 'hydration' has been reported from these materials using remote methods (for example, Mastcam multispectral imaging, ChemCam; Vaniman *et al.*, 2014; Rice *et al.*, 2013; Nachon *et al.*, 2014), the presence of gypsum is unlikely. For the remote methods, the discrimination of gypsum from bassanite (both hydrated) is complicated by matrix effects (Rice *et al.*, 2013; Nachon *et al.*, 2014), whereas the most intense diffraction peak from gypsum is in a region of the XRD pattern that is clear of overlap with other diffraction peaks. Detection limits for gypsum with the CheMin instrument are likely to be <0·5%, based on the analyses here of XRD data for John Klein and Cumberland, and to date gypsum has not been detected with CheMin on Mars. For the remainder of this discussion, all white-filled veins in the Sheepbed mudstone are referred to as anhydrite veins, acknowledging

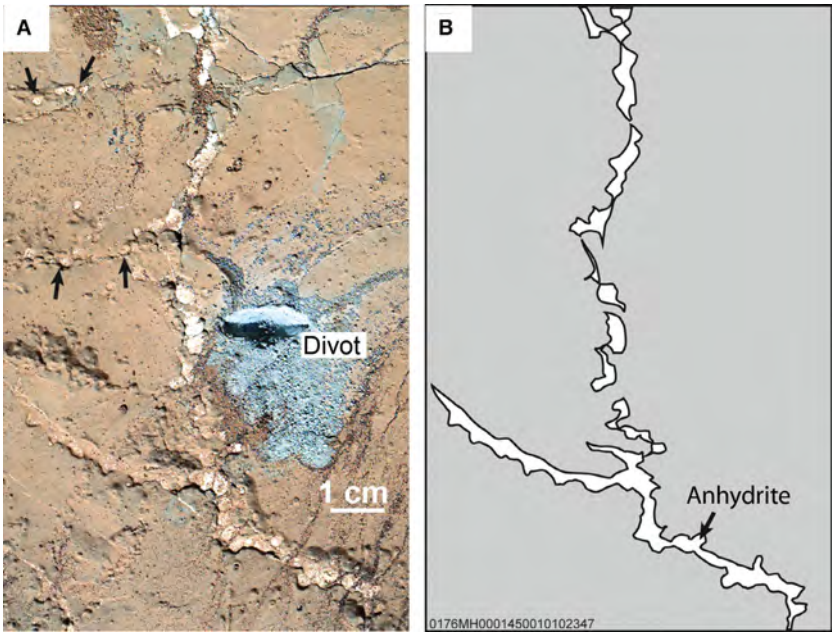

Fig. 25. (A) Image of bedding plane with drill divot scar. Bedding plane is cut by subvertical anhydrite veins. MAHLI image 0176MH0001450010102347C00. (B) Shows a sketch of the anhydrite fill. Instead of being simple filled fractures, these veins have a more complex knobbly morphology. If the anhydrite were removed, the vein walls would not fit back together. MAHLI, Mars Hand Lens Imager.

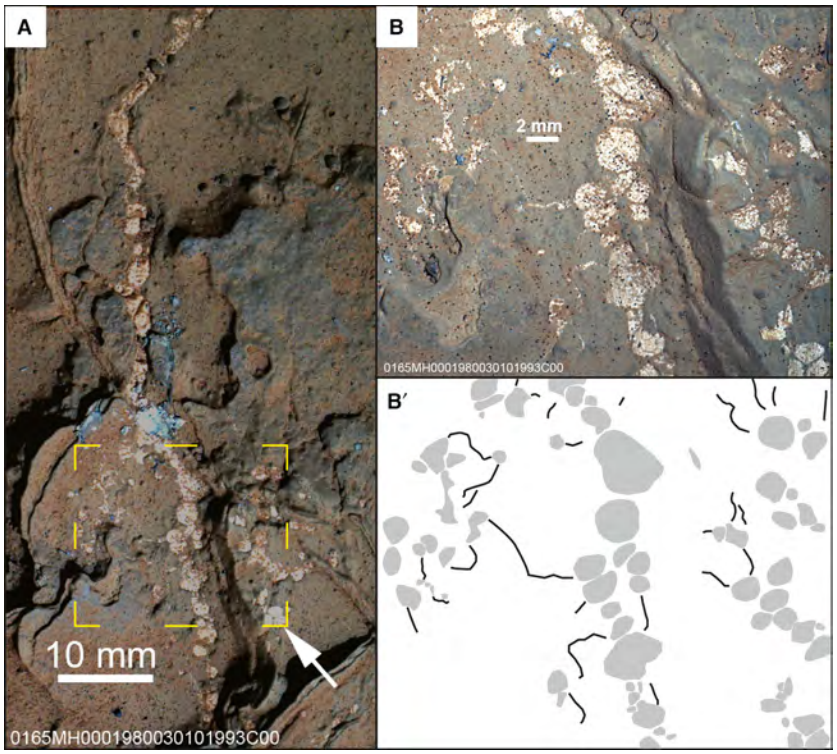

Fig. 26. (A) A knobbly vein extends through the length of a sub-frame of MAHLI image 0166MH0002030030102060C00. The region in the yellow dashed rectangle is enlarged in (B), where the 'string of pearls' character is readily apparent. MAHLI image 0165MH0001980030101993C00. In (B′), the anhydrite spherules are outlined in grey, and connecting hairline fractures are shown as black lines (tracing was made difficult by dust). MAHLI, Mars Hand Lens Imager.

that hydrated forms of $CaSO_4$ (i.e. bassanite) may be present as well.

Knobbly veins

Rounded anhydrite bodies of 1 to 2 mm diameter (Fig. 23) have been attributed to infilling of presumably empty 'hollow nodules' where hairline fractures opened these for mineralizing fluids (Grotzinger *et al.*, 2014; Stack *et al.*, 2014), an explanation that also applies to the cement shells from the model shown in Fig. 20. In the latter (Fig. 20), the centres of cement shells are filled with mostly pore fluids and some sediment and they are easily filled with anhydrite where access becomes possible. There are, however, larger (1 to 15 mm) irregular-rounded anhydrite bodies that occur along veins in Sheepbed strata, and these are not likely to be related to cement shells (Fig. 24). The majority of these veins (described as 'knobbly') appear subvertical in orientation, and the strikes of their intercepts with bedding planes appear random overall.

In plan view (Fig. 25), the rounded bodies have a bulbous-complex, knobbly form and, if the anhydrite were to be removed, the walls of the veins would not fit back together (Fig. 25). The mismatch between adjacent pieces of wall rock that is apparent in Fig. 25 suggests that

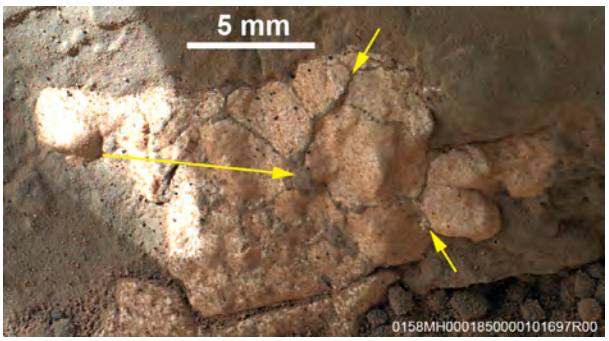

Fig. 27. A look at a fracture surface with anhydrite stuck to the wall. The anhydrite consists of impinging–coalescing spherules that have thin films (short arrows) and pockets (long arrow) of grey matrix material between them. From MAHLI image 0158MH0001850000101697R00. MAHLI, Mars Hand Lens Imager.

these knobbly vein fills reflect a different history than simple fracturing of lithified sediment and then filling the crack with anhydrite as in 'straight veins' (Fig. 22). A closer look at this type of vein suggests a possible explanation.

Although the bedding plane imaged in Fig. 25 is slightly coated by dust and sand, the knobbly anhydrite fillings appear to consist of adjacent and abutting rounded spherules. A close look at

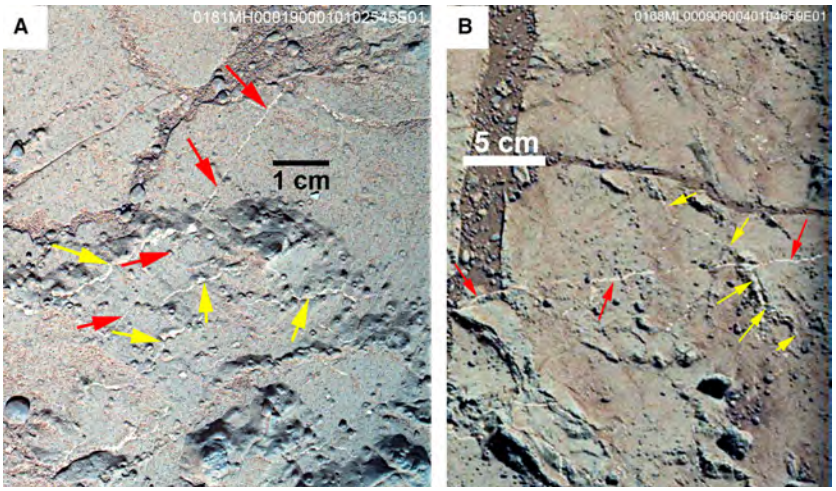

Fig. 28. (A) MAHLI view of a bedding plane with veins (MAHLI image 0181MH00019000101025 4E01). Small knobbly veins are marked with yellow arrows, straight vein is marked with red arrows and cuts across a knobbly vein. (B) Bedding plane view (Mastcam Left image 0168ML00090600401046 59E01) with knobbly vein (yellow arrows) cut by straight vein (red arrows). MAHLI, Mars Hand Lens Imager.

another knobbly vein (Fig. 26), where the aligned anhydrite spherules give the whole a 'string of pearls' appearance, shows this relationship more clearly. Several of the adjacent spherical to ovoid anhydrite grains in Fig. 26 are separated by thin films and pockets of grey matrix. A trio of adjacent spherules indicated by an arrow in Fig. 26A and in the lower right corner of Fig. 26B, illustrates this relationship nicely. In one image (Fig. 27), where anhydrite was imaged on a fracture-parallel surface, multiple growing spherules seem to have coalesced, leaving thin seams and pockets of grey matrix between them.

As pointed out in the *Introduction*, there are no second chances in rover geology. Because imaging the John Klein and Cumberland drill sites (Fig. 2) was focused on characterizing the drill sites and adjacent areas, one could say in hindsight that more images should have been taken to better characterize the sulphate veins. There are, however, a number of 'accidental' views of vein networks that show their spatial

Fig. 29. At the top is a view of a bedding plane with cross-cutting anhydrite veins (portion of a Mastcam Right mosaic (mcam00186) acquired on Sol 270). At the bottom is an attempt to categorize veins. Wide grey lines mark veins with 'complex' or knobbly morphology, like those shown in Fig. 24. Narrow black lines mark narrow, parallel-walled and comparatively straight veins. The tracing of the two vein styles suggests that 'complex' knobbly veins are oriented roughly SE–NW, whereas straight-narrow veins are oriented approximately E–W. Mastcam Right images 0270MR0011860180203241E01, 0270MR0011860210203244E01, 0270MR0011860240203247E01, 0270MR0011860270203250E01, 0270MR0011860480203271E01, 0270MR0011860510203274E01, 0270MR0011860540203277E01 and 0270MR0011860570203280E01.

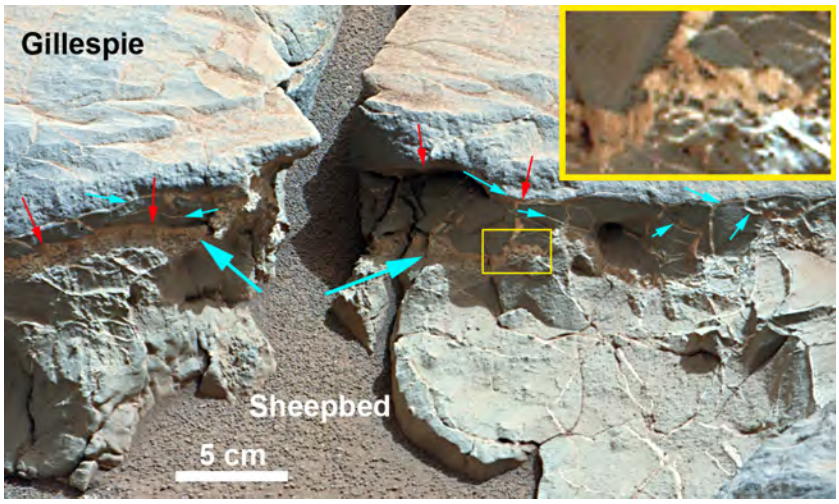

Fig. 30. Image of the contact (marked with red arrows) between the Sheepbed mudstone and the Gillespie Lake sandstone. Illuminated by sunlight from the right, this is a portion of Mastcam Right image 0153MR0008490000201265C00, acquired on Sol 153. Note that the mudstone below the contact shows abundant opening-mode veins with white fill, and that there are abundant subhorizontal veins (turquoise arrows) as well. In a 2 to 3 cm thick horizontal zone beneath the contact (large turquoise arrows), the white fill dominates and contains angular fragments of mudstone (see inset in upper right, enlarged 4×).

relationships in spite of the dust that obscures their subtle details (Fig. 28). Figure 28 shows a MAHLI image where small knobbly veins are cut by a straight vein (Fig. 28A) and a Mastcam image where the same type of cross-cutting relationship is documented (Fig. 28B), indicating that the straight veins formed later in burial history than the knobbly veins. The Mastcam image mosaics at hand show vistas where these two styles of vein development (straight versus knobbly) can be seen dominating (Fig. 22 and Fig. 24, respectively) or intermingled (Fig. 29). The latter figure also shows, although less clearly, that the knobbly veins are cut by straight veins (Fig. 29) and therefore preceded them in burial history.

Horizontal veins at lithological boundaries

Although throughout the Sheepbed interval and elsewhere in the explored succession, anhydrite-filled veins show a dominant subvertical orientation, subhorizontal orientations are observed at fracture offsets and at stratigraphic contacts where rocks of contrasting strength are juxtaposed. The lowermost observed contact of this type is the Sheepbed/Gillespie contact in Yellowknife Bay (Grotzinger *et al.*, 2014; Schieber, 2014), illustrated in Fig. 2B.

The escarpment made by the Gillespie Lake sandstone (Fig. 2) formed because the Gillespie

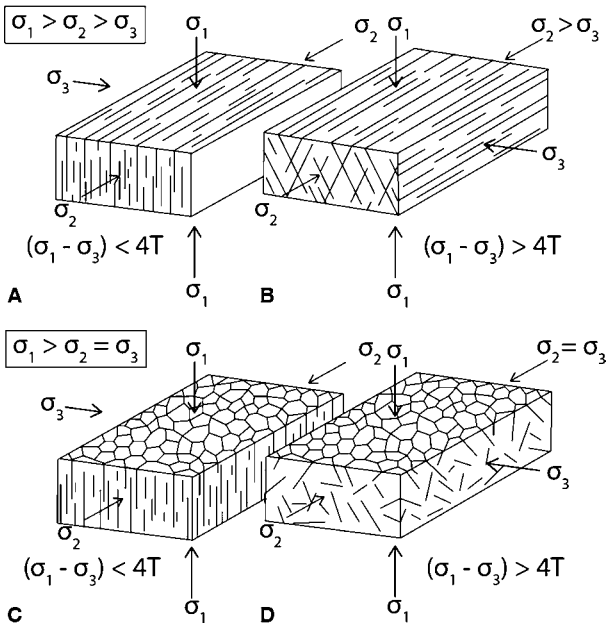

Fig. 31. The impact of the intermediate principal stress (σ_2) on the strike direction of extensional and shear fractures. Extensional fractures form when the differential stress ($\sigma_1 - \sigma_3$) < four times the tensile strength (T) and shear fractures when it is > 4T. In (A) and (B), $\sigma_2 > \sigma_3$ and the strike orientations of the resulting fractures are consistent and regular. In (C) and (D), $\sigma_2 = \sigma_3$ and the fracture strike directions are random, resulting in polygonal arrays. Note that Fig. 31C is the stress regime proposed for the Sheepbed mudstone during the evolution of the vein system it contains. From Cosgrove & Hudson (2016).

is more resistant to present-day aeolian erosion than the underlying Sheepbed mudstone. The Sheepbed is riddled with fractures (Fig. 30), and the fracture density in the overlying Gillespie is significantly lower. Also, below the contact there is a few centimetres thick layer of anhydrite that contains angular clasts of Sheepbed mudstone and anhydrite-filled fractures with horizontal branches are associated with this layer (Fig. 30).

Interpretation of anhydrite veins

The above-described anhydrite-rich zone at the Sheepbed/Gillespie contact has alternatively been interpreted as a result of natural hydraulic fracturing, induced by overpressured fluids that rose from strata beneath the Sheepbed mudstone (Grotzinger *et al.*, 2014; Schieber, 2014), or as an example of displacive gypsum growth (chicken-wire texture) early in depositional history (Nachon *et al.*, 2014). However, the presence of angular fragments of mudstone and the continuation of anhydrite into overlying fractures suggests that the former interpretation (hydraulic fracturing) most likely applies. Displacive gypsum growth can also be excluded based on the volumetric arguments discussed above.

The associated vein types (straight and knobbly) both show spatial organization of fractures that reveals the stress regime under which they formed. The majority of fractures are vertical, appear extensional, and show random strike on bed surfaces. Fractures of this type form at right angles to the least principal compressive stress, σ_3, and contain the maximum and intermediate principal stresses σ_1 and σ_2. Because there is no consistent strike to the veins it follows that the state of stress in the horizontal plane was hydrostatic, i.e. that $\sigma_2 = \sigma_3$, and that the maximum principal stress was vertical. The observed polygonal array of vertical fractures would on Earth be typical of a stress regime associated with a simple overburden load that was unaffected by tectonic stresses (Fig. 31C).

The knobbly veins have qualities that suggest displacive growth of anhydrite in a still-soft matrix. This view is supported by the rounded to coalescing growth textures seen in Figs 26 and 27, and in particular by the thin films and pockets of mudstone matrix between coalesced anhydrite clumps. These same textures are observed in ancient and modern sediments where anhydrite clusters grow and coalesce in semi-consolidated muds (e.g. Lucia, 2007; Kendall, 2010). In typical evaporites, however, displacive anhydrite grows as layers (e.g. Kendall, 2010), not following fractures that cut across bedding.

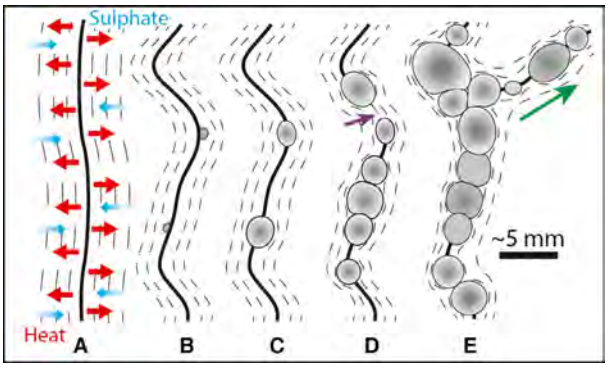

Fig. 32. Evolution of knobbly veins. (A) Overpressuring due to compaction causes fractures in the consolidating mud. Warm fluids rise from depth into colder sediments with dissolved calcium sulphate and gypsum (as suggested by XRD data, and predicted by the calculation in Fig. 11) in the mud matrix. The temperature of the wall zones of fractures increases, anhydrite precipitates, and more $CaSO_4$ diffuses in. (B) First clusters of anhydrite begin to sprout and push into surrounding sediment. Veins may become deformed. (C) As the process continues, anhydrite clusters expand. (D) More and more anhydrite clusters form, but in some parts of the vein no anhydrite precipitates. These portions will pinch shut (purple arrow) once fluid pressure declines (see, for example, Fig. 23). (E) Initial vein may clog with anhydrite and alternative fluid routes develop (green arrow).

Geochemically, anhydrite forms by evaporation, by ice freeze-out, by replacement of Ca minerals (for example, plagioclase) or Ca-bearing glass where sulphate-rich waters permeate, by mixing of Ca^{2+} rich waters with sulphate-rich waters, and by heating of $CaSO_4$ waters, such as seawater where it enters a sea floor hydrothermal system or where it mixes with hot spring waters at a vent. Anhydrite may also form where gypsum recrystallizes to anhydrite upon heating the gypsum, as occurred in the model above (Fig. 11) when the system was heated from 25°C to 50°C. Anhydrite dissolves upon dilution, cooling and chemical reduction (Fig. 11), so these processes are not reasonable components of a precipitation mechanism. In a mud that is not fully consolidated and thus has appreciable porosity, the anhydrite could grow as clusters or rosettes and displace the surrounding sediment (Fig. 32). Additional drivers could be dissolution of early diagenetic gypsum in the mud matrix upon burial and heating along vein

envelopes, coupled with Ostwald Ripening and pressure solution of $CaSO_4$ in the matrix mud, driving movement of aqueous $CaSO_4$ from matrix to fractures where larger crystals form. A possible scheme for knobbly vein formation in this fashion is shown in Fig. 32. Because, as outlined above, bringing dissolved $CaSO_4$ from depth via hot formation waters does not seem feasible, a 'local' source of $CaSO_4$ is indicated. A simple calculation of maximum dissolved anhydrite in pore waters indicates that if pore waters were the only source of $CaSO_4$, the vein spacing would have to be on the order of several metres instead of decimetres, and this suggests that additional $CaSO_4$ may have been contributed via dissolution of dispersed $CaSO_4$ in the mud matrix. The likely presence of $CaSO_4$ in the mud matrix is consistent with XRD data (Vaniman *et al.*, 2014) as well as with the prediction of diagenetic matrix $CaSO_4$ in our calculations of potential diagenetic pathways (Fig. 11).

The observed anhydrite textures, common where anhydrite grows in unconsolidated sediments, imply that the knobbly veins developed in sediment that was still soft enough to be pushed aside by growing crystal clusters and that remaining porosity allowed diffusion of dissolved $CaSO_4$ to the veins. Given that the original sediment was a mud with high water content, it needed to consolidate partially before being able to fracture and respond in a ductile manner to the growing crystal clusters. On Earth, buried muds still retain porosities in the 20 to 30% range at burial depths of as much as 1·7 km (Rieke & Chilingarian, 1974; Kominz *et al.*, 2011). Taking into account the smaller acceleration due to gravity on Mars (*ca* 3·75 m/sec^2), the Sheepbed muds could have retained enough ductility for knobbly vein formation to a burial depth of several kilometres.

The straight veins, on the other hand imply that a significant amount of lithification of the mudstone had taken place prior to the formation of the hydraulic fractures. As noted above, these straight veins occur both normal to and parallel to the bedding, i.e. in a vertical or horizontal orientation. A prominent zone of bedding-parallel veins, together with a horizontal band of anhydrite with angular mudstone fragments occurs just below the Sheepbed – Gillespie contact (Fig. 30). Such horizontal fracturing is compatible with the stress regime proposed for these rocks, i.e. one dominated by an overburden load, provided that the rocks possess a planar anisotropy such as bedding. Such rocks have a lower tensile strength across the bedding (T_n) than parallel to it (T_p) and, as outlined below (Fig. 33), this can result in the formation of horizontal fractures although the maximum principal compression is vertical.

As shown in Fig. 33, the condition for the formation of hydraulic fractures is that the fluid pressure in the rock must exceed the tensile strength of the rock (T) plus the normal stress acting across the potential fracture (Fig. 33A). In a rock with a uniform tensile strength in all directions, this condition is first met along planes normal to the least principal stress, σ_3. As discussed above, the random strike of the vertical (bedding-normal) anhydrite veins indicates that they were formed under a stress regime in which the maximum principal stress (σ_1) was vertical and the intermediate and minimum principal stresses (σ_2 and σ_3) were equal and horizontal (Figs 31C and 33B). The existence of a bedding plane fabric, however, makes the rock mechanically anisotropic with a relatively low tensile strength normal to the bedding (T_n) compared to the higher tensile strength parallel to the bedding (T_p) (Fig. 33C). Thus, in an overburden stress regime with σ_1 vertical and σ_3 horizontal the condition for the formation of *vertical fractures* (veins) is that:

$$P_{fluid} > (\sigma_3 + T_p) \quad (1)$$

and for *horizontal fractures*:

$$P_{fluid} > (\sigma_1 + T_n) \quad (2)$$

Thus, for horizontal fractures to form, condition (2) must be satisfied before condition (1), i.e.:

$$(\sigma_1 + T_n) < (\sigma_3 + T_p) \quad (3)$$

$$\text{i.e. } (\sigma_1 - \sigma_3) < (T_p - T_n) \quad (4)$$

It follows that the formation of horizontal veins within the Sheepbed mudstone and at the Sheepbed–Gillespie contact is compatible with an overburden stress regime and indicates that there was low cohesion across the bedding in the mudstone and at the contact with the overlying Gillespie sandstone at the time of vein formation.

The high density of veins and the horizontal anhydrite-rich zone with angular mudstone fragments below that contact (Fig. 30), suggests that rising fluids may have been impounded at a flow barrier. The Gillespie has considerable

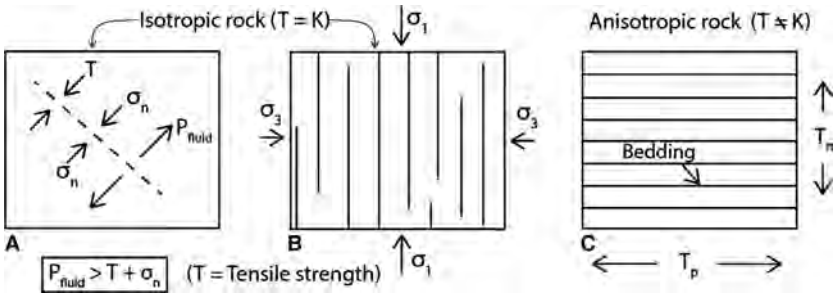

Fig. 33. (A) A block of isotropic rock and the conditions necessary to induce a hydraulic fracture parallel to the dashed line. (B) The block in (A) subjected to an overburden load (σ_1) and an induced horizontal stress (σ_3). Conditions for hydraulic fracturing are first met along the vertical planes normal to σ_3. (C) An anisotropic (bedded) rock subjected to the same stress field as the rock in (B): Tp is the tensile strength parallel to bedding and Tn is the tensile strength normal to bedding.

strength as evident from its erosion resistance in outcrop and little obvious porosity in close-up images. As a sandstone with abundant unstable volcanic components, it is liable to have experienced abundant pore-filling clay generation early in diagenesis and should therefore have low permeability (Pittman, 1979; Surdam & Boles, 1979; Remy, 1994). Thus, as rising fluids hydraulically fractured the Sheepbed mudstone and reached the Sheepbed–Gillespie contact, they spread laterally, caused brecciation, and deposited anhydrite along the contact. Because those fluids could not have removed much $CaSO_4$ from the remaining porosity, the $CaSO_4$ may have been derived from buried evaporites lower in the section.

Although cross-cutting relationships show that the $CaSO_4$ veins post-date the early diagenetic features like nodules, raised ridges and matrix cement, it is difficult to further constrain the time of formation of the veins. The stress configuration appropriate for their formation (Fig. 31C), i.e. that of an overburden load, has been operating on these rocks at all times from the onset of burial and diagenesis to the time of their maximum burial and indeed during their subsequent exhumation. Work by Murray (1964) suggests that the stable form of calcium sulphate in the Earth's crust at depths less than 600 m at a temperature less than 42°C is gypsum. At depths greater than this anhydrite is the stable form. Because this conversion (gypsum to anhydrite) involves a 40% volume loss, voids form that collapse due to overburden pressure and cause fracturing and brecciation of the surrounding sediment (Lucia, 2007). Had the Martian $CaSO_4$ veins been gypsum originally, one should therefore expect to see textural evidence of such volume loss, in particular in association with the geometrically more complex knobbly veins. The complete absence of such features suggests that anhydrite was the primary $CaSO_4$. Following the argument made by Murray (1964), and given that on Mars the acceleration due to gravity is *ca* 3·75 m/sec^2, the anhydrite should therefore have formed at a burial depth of approximately 1·6 km or deeper.

The veined Sheepbed mudstone is currently *ca* 1 km below the major unconformity that separates the water lain sediments of the crater from the >3 km thickness of aeolian sandstones that overlie them (see fig. 8 in Grotzinger *et al.*, 2015). The thickness of the overburden of water lain sediments was clearly ≥1 km before erosion reduced it and could well have exceeded the 1·6 km thought to represent the depth of the gypsum–anhydrite transition noted above. It therefore seems likely that if the veins did form late in burial history, the form of calcium sulphate that would have been deposited in them could well have been anhydrite. This argument can apply to both the somewhat earlier knobbly veins, because it is plausible that sediments stayed partially ductile over several kilometres of burial (see discussion above), as well as to the somewhat later straight veins (Fig. 28). Given that the latter do not show significant deformation due to compaction may imply that they formed close in time to the period of maximum burial. Under the assumption that anhydrite is present in these veins because it formed below the gypsum-anhydrite transition (1.6 km minimum depth), it is interesting to speculate whether gypsum will be found in layers and as vein fills as the rover ascends to higher stratigraphic levels.

Calcium sulphate veins have been observed consistently since leaving Yellowknife Bay as the

rover traversed another 100 m of stratigraphic section, and well-developed sulphate bearing vein networks with an evident multi-stage history have been encountered higher in the stratigraphic section at a location called 'Garden City' (Kronyak *et al.*, 2015a). These observations suggest an extensive and interconnected fracture network that allowed upward fluid migration through a considerable thickness of sedimentary rocks. Evidence for multiple episodes of fluid flow at 'Garden City' provides support for the notion that more than one pulse of late diagenetic fluids also traversed the Sheepbed mudstone.

On Earth, smectites convert to other clay minerals in the course of burial and are not stable over extended time periods above *ca* 70°C (Boles & Franks, 1979), and comparable considerations can be applied to the clay minerals observed by Curiosity (Vaniman *et al.*, 2014; Bish & Milliken, 2015; Bristow *et al.*, 2015). If one considers that these rocks were buried to at least 1·6 km (see above), and possibly to even 4·5 km or more, there are interesting implications with regard to the Martian geothermal gradient. From a clay mineralogy perspective, both clays do not appear to have experienced temperatures much above 50 to 70°C (e.g. Boles & Franks, 1979; Hower & Altaner, 1983; Horton, 1985), although the literature on the details in this low-temperature regime is sparse. At a minimum depth of 1·6 km (to ensure anhydrite stability), 50°C would compute to an Earth-like 31 degrees per kilometre, and for 50°C at a depth of 4·5 km the result would be 11 degrees per kilometre. The latter would be well in keeping with the common assumption that the Martian geothermal gradient is about one-third that of Earth (e.g. Hoffman, 2001; Kargel, 2004). The observation that smectites have persisted in the Sheepbed mudstone for approximately 3·8 billion years (Grotzinger *et al.*, 2014; Bish & Milliken, 2015) and have been buried to a depth of probably several kilometres suggests that the low estimate of the geothermal gradient is probably the more realistic one. This observation may also provide a partial explanation for the persistence of amorphous phases (Vaniman *et al.*, 2014) in these rocks. Amorphous phases in sediments on Earth are altered into diagenetic minerals over the course of millions or tens of millions of years of burial, an effect that has been examined in some detail in research on the diagenetic 'ageing' of red bed successions (Walker, 1967; Van Houten, 1973). A smaller degree of heating of buried Martian sediments is likely to retard this process, although it seems implausible that it would delay it by billions of years. Another factor in the persistence of amorphous material might be a lack of liquid water during diagenesis. Diffusion in the absence of water (thin films between particles) is extremely slow, which could have retarded chemical and mineral transformations (recrystallization) to this day, particularly because most of the reactions occurring during diagenesis involve dissolution and precipitation.

CONCLUSIONS

The present authors are in agreement with prior investigations as to the lacustrine depositional setting of the Sheepbed mudstone (Grotzinger *et al.*, 2014). Yet, although the fine-grained nature of the deposits is consistent with sediment settling from suspension through the water column, it is proposed here that fine-grained hyperpycnal flows were a likely additional agent of sediment transport into the lake basin.

Metre-scale and decametre-scale polygonal cracks in the Sheepbed mudstone are best explained with dehydration of buried smectite bearing rocks upon exposure to the present-day dry Martian atmosphere, rather than being interpreted as desiccation cracks that formed upon the subaerial exposure of water-rich lake sediments. Re-examination of the chemical and mineralogical data suggests that the Sheepbed sediments were derived from eroding Martian upper crust that consisted of a mixture of rock types that had already been weathered to various degrees. At least a portion of the clay minerals observed are likely to be of detrital origin. Modelling the alteration of basaltic starting materials with lake waters shows an abundance of clay minerals as alteration products, and points to the likelihood that the bulk of *in situ* generated clay minerals formed thousands to tens of thousands of years after deposition. Therefore, most of the early diagenetic features, such as nodules, synaeresis crack fills (raised ridges) and matrix cements, formed prior to the bulk of the diagenetic clays.

Early diagenesis in the Sheepbed mudstone can be explained by a single process, the alteration of olivine and/or glass that leads via centrifugal diffusion to the observed features: sequential formation of nodules, cement shells (hollow nodules), filled synaeresis cracks (raised ridges) and matrix cement (resistant ledges). These features were generated as the chemical

contrast between reactive sites (olivine and/or glass alteration) and surrounding pore waters gradually dissipated.

Late diagenesis of the Sheepbed mudstone was dominated by the formation of two styles of anhydrite-filled veins. 'Knobbly' veins formed when the strata may already have been buried by more than a kilometre but still had substantial porosity and ductility, and 'straight' veins formed at even greater burial depth when the mudstone was fully lithified and behaved brittly. Both styles of veins reflect a stress regime associated with simple overburden load, unaffected by tectonic stresses, and are the result of hydraulic fracturing by overpressured fluids. Hydraulic fracturing appears most intense just below the Sheepbed–Gillespie contact, probably because the mechanically stronger and well-cemented Gillespie sandstone acted as a flow barrier for upward migrating fluids. Our interpretation of the origin of anhydrite veins also predicts that gypsum-filled veins may occur at higher elevations on Mt. Sharp.

Combining stability constraints for anhydrite with those for the clay minerals in the Sheepbed mudstone allows estimates of geothermal gradients ranging from 11 to 32 degrees per kilometre, with the former number in agreement with other estimates of the Martian geothermal gradient. Given that unstable clay minerals like smectite were buried several kilometres and did not convert to higher temperature forms of phyllosilicates suggests that the low estimate of the geothermal gradient is more realistic. The long-term (in excess of 3 billion years) persistence of abundant amorphous material in these rocks probably results from a combination of a low level of geothermal gradient, a lack of interstitial water at late stages of burial, and the absence of liquid water throughout most of the subsequent history of these rocks.

EPILOGUE

The tools available to examine sediments on Mars are different in scope and ease of operation from those on Earth: a small number of XRD patterns and whole-rock analyses and a collection of images that are largely at a resolution of multiple sand grains. Thus, it is surprising how far we have been able to extend outwards from those beginnings. On Earth, having that level of data from a mudstone would just be the first step in starting a more serious investigation, involving petrography by optical microscope, and SEM and TEM as well as other more sophisticated analysis, data that would allow substantial constraints for advanced interpretations. On Mars, the current data are all we will ever have in our lifetimes, and thus the only option for optimal use of the data is to rely on in-depth data analysis and the fact that the laws of physics and chemistry apply equally on Mars and Earth. Bringing together a team of highly knowledgeable geologists with expertise ranging from mudstone sedimentology through geochemical and diagenetic modelling to rock mechanics was the key to achieving the sophistication of interpretation that we finally were amazed (and we say so humbly) to arrive at. Even when investigations of mudstones on Earth are considered it is exceedingly rare to have this level of integration. Our joining of forces for this project accomplished everything we set out to do; and it did so because it was a true collaboration, not an assembly of '(L)ego' blocks. Everybody was brought to the project at the height of their experience, but nevertheless learnt from the others, and all that was needed was to capture these inputs and present them in a unified language. We did it on Mars. Could we and others do it again on Earth?

ACKNOWLEDGEMENTS

This work results from MSL science activities performed at the Jet Propulsion Laboratory, California Institute of Technology, under contract with the National Aeronautics and Space Administration. The authors thank the entire MSL Science team for generating an abundance of observations and data in support of science activities. We also thank the MSL engineering and operations teams, who got us to Mars and continue to make the exploration of Gale Crater possible. A special thanks goes to the members of the Malin Space Sciences operations team for their unflagging efforts to provide the high quality images which form the basis of this project. We also thank the Sedimentology editors for agreeing to publish a manuscript of this length, because that allowed us to keep all the strands of reasoning in one coherent piece, rather than spreading them over multiple publications. And, finally, although this manuscript was 'in the works' for about nine months, it still had the inevitable small inconsistencies and errors in it that are par for the course in multi-authored works. Our sincere thanks, therefore, go to reviewers Chris Paola and Kevin Bohacs who helped us to fix these as

well as clarify some muddled prose, and gave the paper its final polish.

REFERENCES

Abegg, F. and **Anderson, A.L.** (1997) The acoustic turbid layer in muddy sediments of Eckernfoerde Bay, Western Baltic: methane concentration, saturation and bubble characteristics. *Mar. Geol.*, **137**, 137–147.

Aiuppa, A. (2009) Degassing of halogens from basaltic volcanism: insights from volcanic gas observations. *Chem. Geol.*, **263**, 99–109. doi:10.1016/j.chemgeo.2008.08.022.

Anderson, A.L., **Abegg, F.**, **Hawkins, J.A.**, **Duncan, M.E.** and **Lyons, A.P.S.** (1998) Bubble populations and acoustic interaction with the gassy floor of Eckernförde Bay. *Cont. Shelf Res.*, **18**, 1807–1838.

Anderson, R., **Bridges, J.C.**, **Williams, A.**, **Edgar, L.**, **Ollila, A.**, **Williams, J.**, **Nachon, M.**, **Mangold, N.**, **Fisk, M.**, **Schieber, J.** and **Gupta, S.** (2015) ChemCam results from the Shaler outcrop in Gale crater, Mars. *Icarus*, **249**, 2–21.

Antrett, P., **Vackiner, A.A.**, **Kukla, P.**, **Klitzsch, N.** and **Stollhofen, H.** (2012) Impact of arid surface megacracks on hydrocarbon reservoir properties. *AAPG Bull.*, **96**, 1279–1299.

Bandstra, J.Z. and **Brantley, S.L.** (2008) Data Fitting Techniques with Applications to mineral dissolution kinetics. In: *Kinetics of Water-Rock Interaction* (Eds S.L. Brantley, J.D. Kubicki and A.F. White), pp. 211–257. Springer, New York.

Bell, J.F., **Malin, M.C.**, **Caplinger, M.A.**, **Ravine, A.S.**, **Godber, M.C.**, **Jungers, M.S.**, **Rice, M.** and **Anderson, R.B.** (2012) Mastcam multispectral imaging on the Mars Science Laboratory rover: Wavelength coverage and imaging strategies at the Gale Crater field site. 43rd Lunar Planet. Sci. Conf., abstract 2541.

Bibring, J.P., **Langevin, Y.**, **Mustard, J.F.**, **Poulet, F.**, **Arvidson, R.**, **Gendrin, A.**, **Gondet, B.**, **Mangold, N.**, **Pinet, P.**, **Forget, F.** and **Berthé, M.** (2006) Global mineralogical and aqueous Mars history derived from OMEGA/Mars Express data. *Science*, **312**, 400–404.

Bish, D.L. and **Milliken, R.E.** (2015) Clay minerals on Mars and Earth: insights into long-term clay mineral stability? *Geol. Soc. Am. Abst. Programs*, **47**, 267.

Bish, D.L. and **Post, J.E.** (1993) Quantitative mineralogical analysis using the Rietveld full-pattern fitting method. *Am. Mineral.*, **78**, 932–940.

Bish, D.L., **Blake, D.F.**, **Vaniman, D.T.**, **Chipera, S.J.**, **Morris, R.V.**, **Ming, D.W.**, **Treiman, A.H.**, **Sarrazin, P.**, **Morrison, S.M.**, **Downs, R.T.**, **Achilles, C.N.**, **Yen, A.S.**, **Bristow, T.F.**, **Crisp, J.A.**, **Morookian, J.M.**, **Farmer, J.D.**, **Rampe, E.B.E.**, **Stolper, E.M.**, **Spanovich, N.** and **Science Team, M.S.L.** (2013) X-ray diffraction results from Mars Science Laboratory: mineralogy of Rocknest at Gale Crater. *Science*, **341**, 1238932.

Bish, D., **Blake, D.**, **Vaniman, D.**, **Sarrazin, P.**, **Bristow, T.**, **Achilles, C.**, **Dera, P.**, **Chipera, S.**, **Crisp, J.**, **Downs, R.T.**, **Farmer, J.**, **Gailhanou, M.**, **Ming, D.**, **Morookian, J.M.**, **Morris, R.**, **Morrison, S.**, **Rampe, E.**, **Treiman, A.** and **Yen, A.** (2014) The first X-ray diffraction measurements on Mars. *Int. Union Crystallogr. J.*, **1**, 514–522.

Blanc, P., **Lassin, A.**, **Piantone, P.**, **Azaroual, M.**, **Jacquemet, N.**, **Fabbri, A.** and **Gaucher, E.C.** (2012) Thermoddem: a geochemical database focused on low temperature water/rock interactions and waste materials. *Appl. Geochem.*, **27**, 2107–2116.

Bohacs, K.M., **Carroll, A.R.**, **Neal, J.E.** and **Mankiewicz, P.J.** (2000) Lake-basin type, source potential, and hydrocarbon character: an integrated-sequence-stratigraphic–geoche mical framework. In: *Lake Basins Through Space and Time* (Eds E.H. Gierlowski-Kordesch and K.R. Kelts), *AAPG Stud. Geol.*, **46**, 3–34.

Boles, J.R. and **Franks, S.G.** (1979) Clay diagenesis in Wilcox sandstones of southwest Texas: implications of smectite diagenesis on sandstone cementation. *J. Sed. Petrol.*, **49**, 55–70.

Boudreau, B.P., **Algar, C.**, **Johnson, B.D.**, **Croudace, I.**, **Reed, A.**, **Furukawa, Y.**, **Dorgan, K.M.**, **Jumars, P.A.**, **Grader, A.S.** and **Gardiner, B.S.** (2005) Bubble growth and rise in soft sediments. *Geology*, **33**, 517–520.

Brady, P.V. and **Walther, J.V.** (1989) Controls on silicate dissolution rates in neutral and basic pH solutions at 25°C. *Geochim. Cosmochim. Acta*, **53**, 2823–2830.

Bristow, T.F., **Bish, D.L.**, **Vaniman, D.T.**, **Morris, R.V.**, **Blake, D.F.**, **Grotzinger, J.P.**, **Rampe, E.B.**, **Crisp, J.A.**, **Achilles, C.N.**, **Ming, D.W.** and **Ehlmann, B.L.** (2015) The origin and implications of clay minerals from Yellowknife Bay, Gale crater, Mars. *Am. Mineral.*, **100**, 824–836.

Burst, J.F. (1965) Subaqueously formed shrinkage cracks in clay. *J. Sed. Petrol.*, **35**, 348–353.

Carr, M.H. and **Head, J.W.** (2010) Geologic history of Mars. *Earth Planet. Sci. Lett.*, **294**, 185–203.

Chan, M.A., **Potter, S.L.**, **Bowen, B.B.**, **Petersen, E.U.**, **Parry, W.T.**, **Bowman, J.R.**, **Barge, L.** and **Seiler, W.** (2012) Characteristics of terrestrial ferric oxide concretions & implications for Mars. In: *Sedimentary Geology of Mars* (Eds J. Grotzinger and R. Milliken), *SEPM Spec. Publ.*, **102**, 253–270.

Chipera, S.J. and **Bish, D.L.** (2002) FULLPAT: a full-pattern quantitative analysis program for X-ray powder diffraction using measured and calculated patterns. *J. Appl. Crystallogr.*, **35**, 744–749.

Coleman, M.L. (1993) Microbial processes: controls on the shape and composition of carbonate concretions. *Mar. Geol.*, **113**, 127–140.

Coleman, M.L. and **Raiswell, R.** (1993) Microbial mineralization of organic matter: mechanisms of self-organisation and inferred rates of precipitation of diagenetic minerals. *Phil. Trans. Roy. Soc. London A*, **344**, 69–87.

Coleman, M.L. and **Raiswell, R.** (1995) Source of carbonate and origin of zonation: pyritiferous carbonate concretions. *Am. J. Sci.*, **295**, 282–308.

Cornen, G., **Bandet, Y.**, **Giresse, P.** and **Maley, J.** (1992) The nature and chronostratigraphy of Quaternary pyroclastic accumulations from Lake Barombi Mbo (West-Cameroon). *J. Volcanol. Geoth. Res.*, **51**, 357–374.

Cosgrove, J.W. and **Hudson, J.A.** (2016) *Structural Geology & Rock Engineering*. Imperial College Press, London UK.

Craig, D.C. and **Loughnan, F.C.** (1964) Chemical and mineralogical transformations accompanying the weathering of basic volcanic rocks from New South Wales. *Soil Res.*, **2**, 218–234.

Dehouck, E., **McLennan, S.M.**, **Meslin, P.Y.** and **Cousin, A.** (2014) Constraints on abundance, composition, and nature of X-ray amorphous components of soils and rocks at Gale crater, Mars. *J. Geophys. Res. Planets*, **119**, 2640–2657.

Edgett, K.S. and **Malin, M.C.** (2004) *The Geologic Record of Early Mars: A Layered, Cratered, and "Valley-ed" Volume.*

35th Lunar and Planetary Science Conference, Abstract # 1188.

Edgett, K.S., **Yingst, R.A.**, **Ravine, M.A.**, **Caplinger, M.A.**, **Maki, J.N.**, **Ghaemi, F.T.**, **Schaffner, J.A.**, **Bell, J.F., III**, **Edwards, L.J.**, **Herkenhoff, K.E.** and **Heydari, E.** (2012) Curiosity's Mars Hand Lens Imager (MAHLI) Investigation. *Space Sci. Rev.*, **170**, 259–317.

Einsele, G. (2000) *Sedimentary Basins: Evolution, Facies, and Sediment Budget*. Press, Springer Verlag, Berlin, 792 pp.

Farley, K.A., **Malespin, C.**, **Mahaffy, P.**, **Grotzinger, J.P.**, **Vasconcelos, P.**, **Milliken, R.E.**, **Malin, M.**, **Edgett, K.S.**, **Pavlov, A.A.**, **Hurowitz, J.A.**, **Grant, J.A.**, **Miller, H.B.**, **Arvidson, R.**, **Beegle, L.**, **Calef, F.**, **Conrad, P.G.**, **Dietrich, W.E.**, **Eigenbrode, J.**, **Gellert, R.**, **Gupta, S.**, **Hamilton, V.**, **Hassler, D.M.**, **Lewis, K.W.**, **McLennan, S.M.**, **Ming, D.**, **Navarro-González, R.**, **Schwenzer, S.P.**, **Steele, A.**, **Stolper, E.M.**, **Sumner, D.Y.**, **Vaniman, D.**, **Vasavada, A.**, **Williford, K.**, **Wimmer-Schweingruber, R.F.** and **the MSL Science Team** (2014) In situ radiometric and exposure age dating of the Martian surface. *Science*, **343**, 1247166.

Förstner, U., **Müller, G.** and **Reineck, H.E.** (1968) Sedimente und Sedimentgefüge des Rheindeltas im Bodensee. *Neues. Jahrb. Miner. Abh.*, **109**, 33–62.

Frey, S.E., **Gingras, M.K.** and **Dashtgard, S.E.** (2009) Experimental studies of gas-escape and water-escape structures, mechanisms and morphologies. *J. Sed. Res.*, **79**, 808–816.

Gislason, S.R. and **Eugster, H.P.** (1987) Meteoric water-basalt interactions. I: a laboratory study. *Geochim. Cosmochim. Acta*, **51**, 2827–2840.

Gislason, S.R. and **Oelkers, E.H.** (2003) Mechanism, rates and consequences of basaltic glass dissolution: II An experimental study of the dissolution rates of basaltic glass as a function of pH and temperature. *Geochim. Cosmochim. Acta*, **67**, 3817–3832.

Grant, J.A., **Wilson, S.A.**, **Mangold, N.**, **Clalef, F.** and **Grotzinger, J.P.** (2014) The timing of alluvial activity in Gale crater. *Mars. Geophys. Res. Lett.*, **41**, 1142–1149.

Grotzinger, J.P., **Sumner, D.Y.**, **Kah, L.C.**, **Stack, K.**, **Gupta, S.**, **Edgar, L.**, **Rubin, D.**, **Lewis, K.**, **Schieber, J.**, **Mangold, N.**, **Milliken, R.**, **Conrad, P.G.**, **DesMarais, D.**, **Farmer, J.**, **Siebach, K.**, **Calef, F.**, **Hurowitz, J.**, **McLennan, S.M.**, **Ming, D.**, **Vaniman, D.**, **Crisp, J.**, **Vasavada, A.**, **Edgett, K.S.**, **Malin, M.**, **Blake, D.**, **Gellert, R.**, **Mahaffy, P.**, **Wiens, R.C.**, **Maurice, S.**, **Grant, J.A.**, **Wilson, S.**, **Anderson, R.C.**, **Beegle, L.**, **Arvidson, R.**, **Hallet, B.**, **Sletten, R.S.**, **Rice, M.**, **Bell, J., III**, **Griffes, J.**, **Ehlmann, B.**, **Anderson, R.B.**, **Bristow, T.F.**, **Dietrich, W.E.**, **Dromart, G.**, **Eigenbrode, J.**, **Fraeman, A.**, **Hardgrove, C.**, **Herkenhoff, K.**, **Jandura, L.**, **Kocurek, G.**, **Lee, S.**, **Leshin, L.A.**, **Leveille, R.**, **Limonadi, D.**, **Maki, J.**, **McCloskey, S.**, **Meyer, M.**, **Minitti, M.**, **Newsom, H.**, **Oehler, D.**, **Okon, A.**, **Palucis, M.**, **Parker, T.**, **Rowland, S.**, **Schmidt, M.**, **Squyres, S.**, **Steele, A.**, **Stolper, E.**, **Summons, R.**, **Treiman, A.**, **Williams, R.**, **Yingst, A.** and **MSL Science Team** (2014) A habitable fluvio-lacustrine environment at Yellowknife Bay, Gale Crater, Mars. *Science*, **343**, 1242777.

Grotzinger, J.P., **Gupta, S.**, **Malin, M.C.**, **Rubin, D.M.**, **Schieber, J.**, **Siebach, K.**, **Sumner, D.Y.**, **Stack, K.M.**, **Vasavada, A.R.**, **Arvidson, R.E.**, **Calef, F., III**, **Edgar, L.**, **Fischer, W.F.**, **Grant, J.A.**, **Griffes, J.**, **Kah, L.C.**, **Lamb, M.P.**, **Lewis, K.W.**, **Mangold, N.**, **Minitti, M.E.**, **Palucis, M.**, **Rice, M.**, **Williams, R.M.E.**, **Yingst, R.A.**, **Blake, D.**, **Blaney, D.**, **Conrad, P.**, **Crisp, J.**, **Dietrich, W.E.**, **Dromart, G.**, **Edgett, K.S.**, **Ewing, R.C.**, **Gellert, R.**, **Hurowitz, J.A.**, **Kocurek, G.**, **Mahaffy, P.**, **McBride, M.J.**, **McLennan, S.M.**, **Mischna, M.**, **Ming, D.**, **Milliken, R.**, **Newsom, H.**, **Oehler, D.**, **Parker, T.J.**, **Vaniman, D.**, **Wiens, R.C.** and **Wilson, S.A.** (2015) Deposition, exhumation, and paleoclimate of an ancient lake deposit, Gale crater, Mars. *Science*, **350**, aac7575-1–12.

Hallet, B., **Sletten, R.S.**, **Stewart, W.**, **Williams, R.**, **Mangold, N.**, **Schieber, J.**, **Sumner, D.** and **Kocurek, G.** and **MSL Science Team** (2012) *Fracture Networks at Gale Crater, Mars*. 43rd Lunar and Planetary Sciences Conference, Houston, TX, March 19–23, 2012, Abstract No. 3108.

Hardie, L.A., **Smoot, J.P.** and **Eugster, H.P.** (1978) Saline lakes and their deposits: a sedimentological approach. In: *Modern and Ancient Lake Sediments* (Eds A. Matter and M.E. Tucker), *Spec. Publ. Int. Ass. Sediment.*, **2**, 7–41.

Harri, A.M., **Genzer, M.**, **Kemppinen, O.**, **Gomez-Elvira, J.**, **Haberle, R.**, **Polkko, J.**, **Savijärvi, H.**, **Rennó, N.**, **Rodriguez-Manfredi, J.A.**, **Schmidt, W.** and **Richardson, M.** (2014) Mars Science Laboratory relative humidity observations, initial results. *J. Geophys. Res. Planets*, **119**, 2132–2147.

Helfferich, F. and **Katchalsky, A.** (1970) A simple model of diffusion with precipitation. *J. Phys. Chem.*, **74**, 306–314.

Hoffman, N. (2001) *Modern Geothermal Gradients on Mars and Implications for Subsurface Liquids*. Conference on the Geophysical Detection of Subsurface Water on Mars, August 6–10, 2001, Lunar and Planetary Institute, Houston, TX, Abstract volume, 49 pp.

Horton, D.G. (1985) Mixed-layer illite/smectite as a paleotemperature indicator in the Amethyst vein system, Creede district, Colorado, USA. *Cont. Mineral. Pet.*, **91**, 171–179.

Houbolt, J.J.H.C. and **Jonker, J.B.M.** (1968) Recent sediments in the eastern part of the Lake of Geneva (Lac Leman). *Geol. Mijnbouw*, **47**, 131–148.

Howald, T. and **Schieber, J.** (2009) *Textural Features Produced by Aeolian Erosion of Mudstones*. 39th Lunar and Planetary Sciences Conference, Houston, TX, March 10–14, 2008, Abstract No. 2052.

Hower, J. and **Altaner, S.P.** (1983) *The Petrologic Significance of Illite/Smectite*. Proceedings of the 20th Annual Clay Minerals Society Meeting, Buffalo, NY, 40 pp.

Jonckbloedt, R.C.L. (1998) Olivine dissolution in sulphuric acid at elevated temperatures: implications for the olivine process, an alternative waste acid neutralizing process. *J. Geochem. Explor.*, **62**, 337–346.

Kargel, J.S. (2004) *Mars-A Warmer, Wetter Planet*. Springer Verlag, London, 558 pp.

Kendall, A.C. (2010) Marine Evaporites. In: *Facies Models 4* (Eds N.P. James and R.W. Dalrymple), *Geol. Assoc. Canada*, 505–539.

Kirkman, J.H. (1975) Clay mineralogy of some tephra beds of Rotorua area, North Island, New Zealand. *Clay Miner.*, **10**, 437–449.

Kominz, M.A., **Patterson, K.** and **Odette, D.** (2011) Lithology dependence of porosity in slope and deep marine sediments. *J. Sed. Res.*, **81**, 730–742.

Kronyak, R.E., **Kah, L.C.**, **Grotzinger, J.P.**, **Fisk, M.R.**, **Sumner, D.Y.**, **Nachon, M.**, **Mangold, N.**, **Blaney, D.L.**, **Rapin, W.** and **Wiens, R.C.** (2015a) Garden city: a complex vein system observed by the Curiosity Rover at Pahrump Hills, Gale Crater, Mars. *Geol. Soc. Am. Abst. Programs*, **47**, 217.

Kronyak, R.E., **Kah, L.C.**, **Nachon, M.**, **Mangold, N.**, **Wiens, R.C.**, **Williams, R.**, **Schieber, J.** and **Grotzinger, J.P.** (2015b) *Distribution of Mineralized Veins from Yellowknife Bay to Mt. Sharp, Gale Crater, Mars: Insight from Textural and Compositional Variation*. 46th Lunar

and Planetary Sciences Conference, Houston, TX, March 16–20, 2015, Abstract No. 1903

Lazar, O.R., **Bohacs, K.M.**, **Macquaker, J.H.**, **Schieber, J.** and **Demko, T.M.** (2015) Capturing key attributes of fine-grained sedimentary rocks in outcrops, cores, and thin sections: nomenclature and description guidelines. *J. Sed. Res.*, **85**, 230–246.

Lu, Z., **Chang, Y.**, **Yin, Q.**, **Ng, C.** and **Jackson, W.** (2014) Evidence for direct molecular oxygen production in CO_2 photodissociation. *Science*, **346**, 61–64.

Lucia, F.J. (2007) *Carbonate Reservoir Characterization – An Integrated Approach*. Springer Verlag, New York, 336 pp.

Malin, M.C. and **Edgett, K.S.** (2000) Sedimentary rocks of early Mars. *Science*, **290**, 1927–1937.

Malin, M.C. and **Edgett, K.S.** (2001) *Rock Stratigraphy in Gale crater, Mars*. 32nd Lunar and Planetary Science Conference, Abstract # 1005.

Malin, M.C., **Edgett, K.S.**, **Cantor, B.A.**, **Caplinger, M.A.**, **Danielson, G.E.**, **Jensen, E.H.**, **Ravine, M.A.**, **Sandoval, J.L.** and **Supulver, K.D.** (2010a) An overview of the 1985–2006 Mars Orbiter Camera science investigation. *Mars*, **5**, 1–60.

Malin, M.C., **Caplinger, M.A.**, **Edgett, K.S.**, **Ghaemi, F.T.**, **Ravine, M.A.**, **Schaffner, J.A.**, **Baker, J.M.**, **Bardis, J.D.**, **DiBiase, D.R.**, **Maki, J.N.** and **Willson, R.G.** (2010b) *The Mars Science Laboratory (MSL) Mast-Mounted Cameras (Mastcams) Flight Instruments*. 41st Lunar and Planetary Science Conference, Abstract # 1123.

Mangold, N., **Forni, O.**, **Dromart, G.**, **Stack, K.**, **Wiens, R.C.**, **Gasnault, O.**, **Sumner, D.Y.**, **Nachon, M.**, **Meslin, P.Y.**, **Anderson, R.B.** and **Barraclough, B.** (2015) Chemical variations in Yellowknife Bay formation sedimentary rocks analyzed by ChemCam on board the Curiosity rover on Mars. *J. Geophys. Res. Planets*, **120**, 452–482.

Marty, N.C.M., **Claret, F.**, **Lassin, A.**, **Tremosa, J.**, **Blanc, P.**, **Madé, B.**, **Giffaut, E.**, **Cochepin, B.** and **Tournassat, C.** (2015) A database of dissolution and precipitation rates for clay-rocks minerals. *Appl. Geochem.*, **55**, 108–118.

McLennan, S.M., **Anderson, R.B.**, **Bell, J.F., III**, **Bridges, J.C.**, **Calef, F., III**, **Campbell, J.L.**, **Clark, B.C.**, **Clegg, S.**, **Conrad, P.**, **Cousin, A.**, **Des Marais, D.J.**, **Dromart, G.**, **Dyar, M.D.**, **Edgar, L.A.**, **Ehlmann, B.L.**, **Fabre, C.**, **Forni, O.**, **Gasnault, O.**, **Gellert, R.**, **Gordon, A.**, **Grant, J.A.**, **Grotzinger, J.P.**, **Gupta, S.**, **Herkenhoff, K.E.**, **Hurowitz, J.A.**, **King, P.L.**, **Le Mouélic, S.**, **Leshin, L.A.**, **Léveillé, R.**, **Lewis, K.W.**, **Mangold, N.**, **Maurice, S.**, **Ming, D.W.**, **Morris, R.V.**, **Nachon, M.**, **Newsom, H.E.**, **Ollila, A.M.**, **Perrett, G.M.**, **Rice, M.S.**, **Schmidt, M.E.**, **Schwenzer, S.P.**, **Stack, K.**, **Stolper, E.M.**, **Sumner, D.Y.**, **Treiman, A.H.**, **VanBommel, S.**, **Vaniman, D.T.**, **Vasavada, A.**, **Wiens, R.C.**, **Yingst, R.A.** and **MSL Science Team** (2014) Elemental geochemistry of sedimentary rocks at Yellowknife Bay, Gale Crater, Mars. *Science*, **343**, 1244734.

McSween, H.Y., **Ruff, S.W.**, **Morris, R.V.**, **Bell, J.F.**, **Herkenhoff, K.**, **Gellert, R.**, **Stockstill, K.R.**, **Tornabene, L.L.**, **Squyres, S.W.**, **Crisp, J.A.** and **Christensen, P.R.** (2006a) Alkaline volcanic rocks from the Columbia Hills, Gusev crater, Mars. *J. Geophys. Res. Planets*, **111**, E9.

McSween, H.Y., **Wyatt, M.B.**, **Gellert, R.**, **Bell, J.F.**, **Morris, R.V.**, **Herkenhoff, K.E.**, **Crumpler, L.S.**, **Milam, K.A.**, **Stockstill, K.R.**, **Tornabene, L.L.** and **Arvidson, R.E.** (2006b) Characterization and petrologic interpretation of olivine-rich basalts at Gusev Crater, Mars. *J. Geophys. Res. Planets*, **111**, E02S10.

Milton, C., **Chao, E.C.T.**, **Axelrod, J.M.** and **Grimaldi, F.S.** (1960) Reedmergnerite, NaBSi3O8, the boron analogue of albite, from the Green River Formation, Utah. *Am. Mineral.*, **45**, 188–199.

Murray, R.C. (1964) Origin and diagenesis of gypsum and anhydrite. *J. Sed. Res.*, **34**, 512–523.

Nachon, M., **Clegg, S.M.**, **Mangold, N.**, **Schröder, S.**, **Kah, L.C.**, **Dromart, G.**, **Ollila, A.**, **Johnson, J.R.**, **Oehler, D.Z.**, **Bridges, J.C.** and **Le Mouélic, S.** (2014) Calcium sulphate veins characterized by ChemCam/Curiosity at Gale crater, Mars. *J. Geophys. Res. Planets*, **119**, 1991–2016.

Nagasawa, K. (1978) Weathering of volcanic ash and other pyroclastic materials. In: *Clay and Clay Minerals of Japan* (Eds T. Sudo and S. Shimoda), pp. 105–125. Elsevier Scientific Publications Co., Amsterdam.

Nesbitt, H.W. and **Young, G.M.** (1982) Early Proterozoic climates and plate motions inferred from major element chemistry of lutites. *Nature*, **299**, 715–717.

Nesbitt, H.W. and **Young, G.M.** (1984) Prediction of some weathering trends of plutonic and volcanic rocks based on thermodynamic and kinetic considerations. *Geochim. Cosmochim. Acta*, **48**, 1523–1534.

Newsom, H.E., **Nelson, M.J.**, **Shearer, C.K.** and **Misra, S.** (2004) *Hydrothermal Processes in Impact Craters on Mars: Implications from Lonar Crater, India, and Other Craters*. AGU 2004 Fall Meeting Abstracts, Vol. 1, 6 pp.

Newsom, H.E., **Belgacem, I.**, **Jackson, R.**, **Ha, B.**, **Vaci, Z.**, **Wiens, R.C.**, **Frydenvang, J.**, **Gasda, P.**, **Lanza, N.**, **Clegg, S.**, **Gasnault, O.**, **Maurice, S.**, **Cousin, A.**, **Rapin, W.**, **Forni, O.**, **Banham, S.**, **Gupta, S.**, **Williams, A.**, **Grotzinger, J.**, **Blaney, D.**, **Schroeder, J.**, **Calef, F.**, **Francis, R.**, **Ehlmann, B.**, **Yen, A.**, **Stein, N.**, **Rubin, D.**, **Bridges, N.**, **Johnson, J.**, **Lewis, K.**, **Payré, V.**, **Mangold, N.**, **Edgett, K.**, **Fey, D.**, **Fisk, M.**, **Gellert, R.**, **Thompson, L.**, **Schmidt, M.**, **Perrett, G.**, **Kah, L.**, **Kronyak, R.**, **Anderson, R.**, **Herkenhoff, K.**, **Bridges, J.**, **Hurowitz, J.**, **Schieber, J.**, **Heydari, E.** and **Watkins, J.** (2016) *The Materials at an Unconformity between the Murray and Stimson Formations at Marias Pass, Gale Crater, Mars*. 47th Lunar and Planetary Sciences Conference, Houston, TX, March 21–25, 2016, Abstract No. 2397.

Nimmo, F. and **Tanaka, K.** (2005) Early crustal evolution of Mars 1. *Annu. Rev. Earth Planet. Sci.*, **33**, 133–161.

Oelkers, E.H. (2001a) An experimental study of forsterite dissolution rates as a function of temperature and aqueous Mg and Si concentrations. *Chem. Geol.*, **175**, 485–494.

Oelkers, E.H. (2001b) General kinetic description of multioxide silicate mineral and glass dissolution. *Geochim. Cosmochim. Acta*, **65**, 3703–3719.

Oppenheimer, C., **Fischer, T.** and **Scaillet, B.** (2014) Volcanic degassing: process and impact, chapter 4.4. In: *Treatise on Geochemistry*, 2nd Edition (Ed. R.L. Rudnick), pp. 111–179. Elsevier, Amsterdam.

Palandri, J. and **Reed, M.H.** (2001) Reconstruction of in situ composition of sedimentary formation waters. *Geochim. Cosmochim. Acta*, **65**, 1741–1767.

Palucis, M.C., **Dietrich, W.E.**, **Hayes, A.G.**, **Williams, R.M.**, **Gupta, S.**, **Mangold, N.**, **Newsom, H.**, **Hardgrove, C.**, **Calef, F.** and **Sumner, D.Y.** (2014) The origin and evolution of the Peace Vallis fan system that drains to the Curiosity landing area, Gale Crater, Mars. *J. Geophys. Res. Planets*, **119**, 705–728.

Parsons, A.J. and **Abrahams, A.D.** (2009) *Geomorphology of Desert Environments*. Springer, New York, 852 pp.

Pettijohn, F.J. and **Potter, P.E.** (1964) *Atlas and Glossary of Primary Sedimentary Structures*. Springer-Verlag, New York, 370 pp.

Pittman, E.D. (1979) Recent advances in sandstone diagenesis. *Annu. Rev. Earth Planet. Sci.*, **7**, 39–62.

Plummer, P.S. and **Gostin, V.A.** (1981) Shrinkage cracks: desiccation or synaeresis? *J. Sed. Res.*, **51**, 1147–1156.

Pokrovsky, O.S. and **Schott, J.** (2000) Kinetics and mechanism of forsterite dissolution at 25°C and pH from 1 to 12. *Geochim. Cosmochim. Acta*, **64**, 3313–3325.

Potter, P.E., **Maynard, J.B.** and **Depetris, P.J.** (2005) *Mud and Mudstones: Introduction and Overview*. Springer Verlag, Berlin, 298 pp.

Pratt, B.R. (1998) Syneresis cracks: subaqueous shrinkage in argillaceous sediments caused by earthquake-induced dewatering. *Sed. Geol.*, **117**, 1–10.

Raiswell, R. and **Fisher, Q.J.** (2000) Mudrock-hosted carbonate concretions: a review of growth mechanisms and their influence on chemical and isotopic composition. *J. Geol. Soc.*, **157**, 239–251.

Raiswell, R., **Whaler, K.**, **Dean, S.**, **Coleman, M.L.** and **Briggs, D.E.G.** (1993) A simple three dimensional model of diffusion plus precipitation applied to localised pyrite formation in framboids, fossils and detrital iron minerals. *Mar. Geol.*, **113**, 89–100.

Rampe, E.B., **Ming, D.W.**, **Morris, R.V.**, **Blake, D.F.**, **Bristow, T.F.**, **Chipera, S.J.**, **Vaniman, D.T.**, **Yen, A.S.**, **Grotzinger, J.P.**, **Downs, R.T.**, **Morrison, S.M.**, **Peretyazhko, T.**, **Achilles, C.N.**, **Bish, D.L.**, **Cavanagh, P.D.**, **Craig, P.I.**, **Crisp, J.A.**, **Fairén, A.G.**, **Des Marais, D.J.**, **Farmer, J.D.**, **Fendrich, K.V.**, **Morookian, J.M.** and **Treiman, A.H.** (2016) *Diagenesis in the Murray Formation, Gale Crater, Mars*. 47th Lunar and Planetary Sciences Conference, Houston, TX, March 21–25, 2016, Abstract No. 2543.

Reed, M.H. (1998) Calculation of Simultaneous Chemical Equilibria in Aqueous-Mineral-Gas Systems and its Applications to Modeling Hydrothermal Processes. *Rev. Econ. Geol.*, **10**, 109–124.

Reed, M. and **Palandri, J.** (2015) *SOLTHERM.XPT, A Database of Equilibrium Constants for Minerals and Aqueous Species*. University of Oregon, Eugene, Oregon. Available at: http://pages.uoregon.edu/palandri/.

Reineck, H.E. and **Singh, I.B.** (1980) *Depositional Sedimentary Environments*. Springer, Berlin, 549 pp.

Remy, R.R. (1994) Porosity reduction and major controls on diagenesis of Cretaceous-Paleocene volcaniclastic and arkosic sandstone, Middle Park Basin, Colorado. *J. Sed. Res.*, **64**, 797–806.

Renaut, R.W. and **Gierlowski-Kordesch, E.H.** (2010) Lakes. In: *Facies Models 4* (Eds N.P. James and R.W. Dalrymple), *Geol. Assoc. Canada*, 541–575.

Rice, M.S., **BellIII, J.F.**, **Godber, A.**, **Wellington, D.**, **Fraeman, A.A.**, **Johnson, J.R.**, **Kinch, K.M.**, **Malin, M.C.** and **Grotzinger, J.P.** (2013) Mastcam multispectral imaging results from the Mars Science Laboratory investigation in Yellowknife Bay. In: *European Planetary Science Congress 2013*, Vol. 8. London, UK, 762 pp. Available at: http://meetings.copernicus.org/epsc2013id.EPSC2013-762.

Rich, C.I. (1968) Hydroxy interlayers in expansible layer silicates. *Clays Clay Miner.*, **16**, 15–30.

Rieke, H.H. and **Chilingarian, G.V.** (1974) *Compaction of Argillaceous Sediments, Developments in Sedimentology*, Vol. 16. Elsevier, Amsterdam, 423 pp.

Robbins, S.J., **Hynek, B.M.**, **Lillis, R.J.** and **Bottke, W.F.** (2013) Large impact crater histories of Mars: the effect of different model crater age techniques. *Icarus*, **225**, 173–184.

Robertson, K. and **Bish, D.** (2013) Constraints on the distribution of $CaSO_4{\cdot}nH_2O$ phases on Mars and implications for their contribution to the hydrological cycle. *Icarus*, **223**, 407–417.

Rossman, B., **Wilson, R.** and **Schieber, J.** (2012) *Eolian Erosion Experiments on Soft Sedimentary Rocks – Measurement of Erosion Rates, Textural Observations, and Implications for Mars Rover Geology*. 43rd Lunar and Planetary Sciences Conference, Houston, TX, March 19–23, 2012, Abstract No. 2837.

Rosso, J.J. and **Rimstidt, J.D.** (2000) A high resolution study of forsterite dissolution rates. *Geochim. Cosmochim. Acta*, **64**, 797–811.

Saigusa, M., **Shoji, S.** and **Kato, T.** (1978) Origin and nature of halloysite in Ando soils from Towada tephra, Japan. *Geoderma*, **20**, 115–129.

Salem, A.M., **Morad, S.**, **Mato, L.F.** and **Al-Aasm, I.S.** (2000) Diagenesis and reservoir-quality evolution of fluvial sandstones during progressive burial and uplift: evidence from the Upper Jurassic Boipeba Member, Reconcavo Basin, Northeastern Brazil. *AAPG Bull.*, **84**, 1015–1040.

Schieber, J. (2011) Reverse engineering mother nature – shale sedimentology from an experimental perspective. *Sed. Geol.*, **238**, 1–22.

Schieber, J. (2014) *A Seal Breach on Mars – How We Closed in on a Mudstone and Teased Information from Images and Comparison with Experimental and Earth Analogs*. AAPG Annual Convention and Exhibition, Houston, Texas, USA, April 6–9, 2014. AAPG Datapages/Search and Discovery Article #90189.

Schmidt, K.-H. (1989) The significance of scarp retreat for cenozoic landform evolution on the Colorado Plateau, U.S.A. *Earth Surface Processes Landforms*, **14**, 93–105.

Schulte, M., **Blake, D.**, **Hoehler, T.** and **McCollom, T.** (2006) Serpentinization and its implications for life on the early earth and Mars. *Astrobiology*, **6**, 364–376.

Sefton-Nash, E. and **Catling, D.C.** (2008) Hematitic concretions at Meridiani Planum, Mars: their growth timescale and possible relationship with iron sulphates. *Earth Planet. Sci. Lett.*, **269**, 365–375.

Siebach, K.L., **Grotzinger, J.P.**, **Kah, L.C.**, **Stack, K.M.**, **Malin, M.**, **Léveillé, R.** and **Sumner, D.Y.** (2014) Subaqueous shrinkage cracks in the sheepbed mudstone: implications for early fluid diagenesis, Gale Crater, Mars. *J. Geophy. Res. Planets*, **119**, 1597–1613.

Simms, M.J. (2007) Uniquely extensive soft-sediment deformation in the Rhaetian of the UK: evidence for earthquake or impact?. *Palaeogeogr. Palaeoclimatol. Palaeoecol.*, **244**, 407–423.

Singer, A. (1980) The paleoclimatic interpretation of clay minerals in soils and weathering profiles. *Earth Sci. Rev.*, **15**, 303–326.

Sletten, R.S. and **Hallet, B.** (2014) *On 10 to 30 m-Scale Fracture Networks in Gale Crater: Contraction of Fine-Grained Sediments Due to Drying or of Frozen Sediments Due to Cooling?* EGU General Assembly Meeting, Vienna, Austria, April 27-May 02, 2014, abstract volume.

Smith, M.E., **Chamberlain, K.R.**, **Singer, B.S.** and **Carroll, A.R.** (2010) Eocene clocks agree: coeval 40Ar/39Ar, U-Pb, and astronomical ages from the Green River Formation. *Geology*, **38**, 527–530.

Stack, K.M., **Grotzinger, J.P.**, **Kah, L.C.**, **Schmidt, M.E.**, **Mangold, N.**, **Edgett, K.S.**, **Sumner, D.Y.**, **Siebach, K.L.**, **Nachon, M.**, **Lee, R.** and **Blaney, D.L.** (2014) Diagenetic origin of nodules in the Sheepbed member, Yellowknife Bay formation, Gale crater, Mars. *J. Geophy. Res. Planets*, **119**, 1637–1664.

Sturm, M. and **Matter, A.** (1978) Turbidites and varves in Lake Brienz (Switzerland): deposition of clastic detritus by density currents. In: *Modern and Ancient Lake Sediments* (Eds A. Matter and M.E. Tucker), *Spec. Publ. Int. Ass. Sediment.*, **2**, 147–168.

Sun, V.Z. and **Milliken, R.E.** (2015) Ancient and recent clay formation on Mars as revealed from a global survey of hydrous minerals in crater central peaks. *J. Geophy. Res. Planets*, **120**, 2293–2332.

Surdam, R.C. and **Boles, J.R.** (1979) Diagenesis of volcanogenic sandstones. In: *Aspects of Diagenesis* (Eds P.A. Scholle and P.R. Schlager), *Soc. Econ. Paleontol. Mineral. Spec. Publ.*, **26**, 227–242.

Talbot, M.R. and **Allen, P.A.** (1996) Lakes. In: *Sedimentary Environments: Processes, Facies and Stratigraphy* (Ed. H.G. Reading), pp. 83–124. Blackwell Science, Oxford, UK.

Tanaka, K.L. (1986) The stratigraphy of Mars. J. Geophys. Res.- Solid. *Earth*, **91**, E139–E158.

Taylor, K.G. and **Macquaker, J.H.S.** (2000) Spatial and temporal distribution of authigenic minerals in continental shelf sediments: implications for sequence stratigraphic analysis. In: *Marine Authigenesis: From Global to Microbial* (Eds C.R. Glenn, L. Prévôt and J. Lucas), *SEPM Spec. Publ.*, **66**, 309–323.

Taylor, S.R. and **McLennan, S.** (2009) *Planetary Crusts: Their Composition, Origin and Evolution*. Cambridge University Press, Cambridge, 404 pp.

Ulmer-Scholle, D.S., **Scholle, P.A.**, **Schieber, J.** and **Raine, R.J.** (2015) A Color Guide to the Petrography of Sandstones, Siltstones, Shales and Associated Rocks. *AAPG Mem.*, **109**, 505.

Van Herk, J., **Pietersen, H.S.** and **Schuiling, R.D.** (1989) Neutralization of industrial waste acids with olivine - The dissolution of forsteritic olivine at 40–70 º C. *Chem. Geol.*, **76**, 341–352.

Van Houten, F.B. (1973) Origin of red beds: a review-1961-1972. *Annu. Rev. Earth Planet. Sci.*, **1**, 39–61.

Vaniman, D.T., **Bish, D.L.**, **Ming, D.W.**, **Bristow, T.F.**, **Morris, R.V.**, **Blake, D.F.**, **Chipera, S.J.**, **Morrison, S.M.**, **Treiman, A.H.**, **Rampe, E.B.**, **Rice, M.**, **Achilles, C.N.**, **Grotzinger, J.P.**, **McLennan, S.M.**, **Williams, J.**, **Bell, J.F., III**, **Newsom, H.E.**, **Downs, R.T.**, **Maurice, S.**, **Sarrazin, P.**, **Yen, A.S.**, **Morookian, J.M.**, **Farmer, J.D.**, **Stack, K.**, **Milliken, R.E.**, **Ehlmann, B.L.**, **Sumner, D.Y.**, **Berger, G.**, **Crisp, J.A.**, **Hurowitz, J.A.**, **Anderson, R.**, **Des Marais, D.J.**, **Stolper, E.M.**, **Edgett, K.S.**, **Gupta, S.**, **Spanovich, N.** and **MSL Science Team** (2014) Mineralogy of a mudstone at Yellowknife Bay, Gale Crater, Mars. *Science*, **343**, 1243480.

Viviano, C.E., **Moersch, J.E.** and **McSween, H.Y.** (2013) Implications for early hydrothermal environments on Mars through the spectral evidence for carbonation and chloritization reactions in the Nili Fossae region. *J. Geophy. Res. Planets*, **118**, 1858–1872.

Wada, S. (1989) Allophane and Imogolite. In: *Minerals in Soil Environments* (Eds J.B. Dixon and S.B. Weed), pp. 1051–1087. Soil Science Society of America Book Series, Soil Science Society of America, Madison, WI.

Walker, T.R. (1967) Color of recent sediments in tropical Mexico: a contribution to the origin of red beds. *Geol. Soc. Am. Bull.*, **78**, 917–920.

Wiens, R.C. and **Maurice, S.** (2015) ChemCam: chemostratigraphy by the First Mars Microprobe. *Elements*, **11**, 33–38.

Williams, R.M.E., **Grotzinger, J.P.**, **Dietrich, W.E.**, **Gupta, S.**, **Sumner, D.Y.**, **Wiens, R.C.**, **Mangold, N.**, **Malin, M.C.**, **Edgett, K.S.**, **Maurice, S.**, **Forni, O.**, **Gasnault, O.**, **Ollila, A.**, **Newsom, H.E.**, **Dromart, G.**, **Palucis, M.C.**, **Yingst, R.A.**, **Anderson, R.B.**, **Herkenhoff, K.E.**, **Le Mouélic, S.**, **Goetz, W.**, **Madsen, M.B.**, **Koefoed, A.**, **Jensen, J.K.**, **Bridges, J.C.**, **Schwenzer, S.P.**, **Lewis, K.W.**, **Stack, K.M.**, **Rubin, D.**, **Kah, L.C.**, **Bell, J.F., III**, **Farmer, J.D.**, **Sullivan, R.**, **Van Beek, T.**, **Blaney, D.L.**, **Pariser, O.**, **Deen, R.G.** and **MSL Science Team** (2013) Martian fluvial conglomerates at Gale Crater. *Science*, **340**, 1068–1072.

Wilson, R., **Schieber, J.** and **Howald, T.V.** (2011) *Experimental Eolian Erosion of Soft Sedimentary Rocks with a Variety of Abrasives – Observed Features and Potential Applications for Mars Rover Geology*. 42nd Lunar and Planetary Sciences Conference, Houston, TX, March 19-23 2012, Abstract No. 2837.

Wogelius, R.A. and **Walther, J.V.** (1992) Olivine dissolution kinetics at near-surface conditions. *Chem. Geol.*, **97**, 101–112.

Wolff-Boenisch, D., **Gislason, S.R.**, **Oelkers, E.H.** and **Putnis, C.V.** (2004) The dissolution rates of natural glasses as a function of their composition at pH 4 and 10.6, and temperatures from 25 to 74°C. *Geochim. Cosmochim. Acta*, **68**, 4843–4858.

Yoshida, H., **Ujihara, A.**, **Minami, M.**, **Asahara, Y.**, **Katsuta, N.**, **Yamamoto, K.**, **Sirono, S.I.**, **Maruyama, I.**, **Nishimoto, S.** and **Metcalfe, R.** (2015) Early post-mortem formation of carbonate concretions around tusk-shells over week-month timescales. *Sci. Rep.*, **5**, 14123.

Manuscript received 30 March 2016; revision accepted 5 August 2016